Sensor and Simulation Notes
Note 409
August 11, 1997

# The P×M Antenna and Applications to Radiated Field Testing of Electrical Systems

## Part-2 - Experimental Considerations



F.M. Tesche
EMC Consultant
Dallas, TX
Tesche@ont.com

Torbjörn Karlsson
Sven Garmland
EMICON
Linkoping, SWEDEN
Torbjorn@Emicon.se

## Abstract

*This report continues with a study of the EM behavior of the p×m antenna which consists of orthogonal electric and magnetic dipole elements operating together. At low frequencies, this antenna produces near fields in a particular direction that have the same impedance as a plane wave in free space. Four different types of antenna structures are analyzed in this report, and design curves for the proper resistance loading are given for each. One specific structure — the inverted V antenna — is chosen for use in an experimental program, and the measured results are described. Detailed calculations for this antenna also have been performed, and comparisons with the measurements are made.*

## Acknowledgment

This note extends some of the early work of Dr. C. E. Baum in low frequency radiators for the near-field illumination of electrical systems. Thanks are due to Dr. Baum, not only for his support of this effort, but also for his many interesting ideas and discussions on this subject. In addition, thanks are due to Dr. Armin Kälin of the Swiss NEMP Laboratory for his earlier support of this study. This work was partially supported by the Phillips Laboratory of the US Air Force, Kirtland AFB, NM.

# Contents

# Contents (con't.)

# Figures

# Figures (con't)

# Figures (con't)

# Figures (con't)

# Figures (con't)

# Figures (con't)

# The P×M Antenna and Applications to Radiated EM Field Testing

## Part-2 - Experimental Considerations

### 1. Introduction

An earlier note [1] has laid the foundation for understanding the electromagnetic behavior of the p×m antenna. This antenna is a specially designed radiator which possesses both an electric and magnetic dipole moment in the proper ratio so that the EM fields produced by the antenna have an E/H ratio of 377 Ω in the near field.

Understanding how this antenna works is relatively straightforward. By using point dipole moment models, a simple representation for the low frequency behavior of the antenna is possible, and this leads to analytic expressions for the fields produced at an arbitrary observation point. This understanding of the p×m principles, however, does not immediately lead one to a design of a specific antenna having the desired radiating characteristics. Real antennas are finite in extent, and as a consequence, their low frequency behavior cannot be modeled by simple point dipole moments if the observer is too close to the antenna. Furthermore, at higher frequencies, the presence of higher-order multipole moments make the problem much more complex.

Moreover, practical antennas are usually fed by a single voltage source and this produces both the electric and magnetic dipole moment. To adjust these moments to the proper ratio requires changing either the antenna geometry, the source position, the resistive loading on the antenna, or a combination of these elements. None of these issues is explained by the simple point dipole moment model.

In addition, physical antennas must operate in real-world environments, including an imperfectly conducting ground plane. In such a situation, it is not at all clear how applicable the ideal point dipole moment representation of the antenna will fare in providing approximations to the EM fields.

To understand these practical aspects of the p×m antenna, a combined theoretical and experimental program was conducted, and this report documents the results. The first part of this report deals with various pre-test analysis issues. Of key interest is how to determine the proper impedance loading on the antenna to maintain the desired p×m operating characteristics. Various techniques for doing this are suggested in Section 2. Many different shapes of antennas are possible for the p×m structure. In Section 3, the transmission line (Beverage) antenna, the triangular antenna, the inverted V antenna and the half-toroidal antenna are examined, and the results of a parametric study are presented to allow the determination of the proper load resistance for a wide variety of antenna dimensions. The inverted V antenna is identified as the candidate for field testing and for

this specific shape of antenna, studies of how the fields vary with changes in the aspect ratio of this antenna are conducted in Section 4.

The effect and influence of the lossy ground on the antenna operation is addressed theoretically in Section 5 for the special case of the inverted V antenna. There, it is found that the lossy ground has an important influence on both the fields and the wave impedance. A clear problem in this case is that the electrical parameters of the earth are seldom known accurately, and this can lead to large discrepancies between the theoretical predications and measured results.

The second part of this report, which begins with Section 6, documents the experimental portion of the effort. Measurements were made by Emicon in Sweden during the month of May, 1997, and involved testing a full-scale inverted V antenna over a real earth, and a 1:10 scale model antenna with a highly conducting ground plane. Special emphasis is placed on understanding how to determine the proper antenna loading, on mapping the E and H near fields, and in examining the E/H ratio of the primary field components in the near field. In this section, each measured data record is compared with a computed response, thereby offering an estimate of the degree of agreement (or disagreement in some cases) between theory and experiment. As might be expected, the experiments with the scale model antenna over the highly conducting earth offer better agreement with the calculations than do those for the antenna over the lossy earth.

It should be noted in passing that this is not the first time that attempts at using the p×m antenna in an EM measurement program have been made. In 1990, Emtech (now Emicon) in Sweden was preparing for an EMP test of the 155 m high Kaknäs radio tower in Stockholm, as was reported in an NEM paper [2]. In this test, field strengths produced by scale models of possible p×m antennas were measured. The antennas were placed on a grass field with unknown impedance properties. The shapes of the measured antennas were dictated by the restricted possibilities to erect an antenna that was large enough to create a detectable response inside the tower.

The results of the measurements on the scale model were not reported, but were used for the construction of a 60 m high p×m antenna that provided the field illumination of the tower in the frequency range below 1 MHz. The antenna base length was 100 m, and the distance to the tower from the closest point of the antenna was about 100 m. It was concluded in this test, which occurred in February-March 1991, that the p×m antenna construction gave an illumination that was a much better approximation to the real far field conditions than what was possible to achieve by simple dipoles, like a rod antenna or a loop antenna.

## 2. Determination of the P×M Radiating Condition

As discussed in ref. [1], when a p×m antenna is configured to provide quasistatic electric and magnetic dipole moments that are both orthogonal to each other and related by the expression

$$cp_z = -m_y, \tag{1}$$

the electromagnetic fields produced by the antenna propagate primarily in the $+x$ direction, with an *E/H* ratio of 377 Ω, *even in the near field.* This property makes the p×m antenna particularly useful for illuminating test objects with EM fields appearing locally like a plane wave.

For practical use of the p×m antenna concept, it is important to design the antenna such that the proper *cp/m* ratio of Eq.(1) is maintained. This can be done in several different ways:

- by calculating the electric and magnetic dipole moments, and adjusting their strengths to provide the proper the ratio
- by examining the near-zone E and H fields in the forward direction of the antenna, and adjusting the antenna parameters so that the E/H ratio is 377 Ω, or
- by examining the primary component of the E-field in the backward direction and adjusting the antenna parameters so that the field is minimized.

Each of these possibilities is discussed in this section

### *2.1 Calculation of the Dipole Moments of the Antenna*

As the magnetic and electric dipole moments of the antenna are defined in terms of the static current and charge distributions on the conductors, it is possible to consider two simple static problems to evaluate the dipole moments. Once these are known, their ratio can be adjusted by either changing the antenna configuration or by adding resistive loading on the antenna.

To illustrate this procedure, consider the case of an arbitrary loop antenna located over a perfectly conducting ground plane, as shown in Figure 1. Assuming that the only resistance in the antenna is the load $R_L$, the voltage generator $V_o$ produces a current $I = V_o/R_L$. Because this is assumed to be a static problem, the current is not a function of position $\zeta$ along the wire. From the expressions provided in ref. [3], the magnetic dipole moment for this loop antenna can be written as

$$\vec{m} = \frac{1}{2}\int_{wire}\left(\vec{r}' \times \hat{\zeta}\right) I(\zeta)d\zeta + \frac{1}{2}\int_{image\ wire}\left(\vec{r}'^{*} \times \hat{\zeta}^{*}\right) I(\zeta)d\zeta\,, \tag{2}$$

where the first term corresponds to the physical current flowing in the antenna and the second term takes into account the ground plane effects through image theory. In this expression $\hat{\zeta}$ denotes the unit vector in the direction of the current flow in the physical wire and $\hat{\zeta}^{*}$ is the corresponding unit vector on the image conductor.

Using the fact that the integral terms in Eq.(2) are proportional to the areas of the loop and the image loop respectively [4], the net magnetic dipole moment for this structure can be written as

$$\begin{aligned} m_y &= -2A_L I \\ &= -2A_L \frac{V_o}{R_L}. \end{aligned} \tag{3}$$

In this expression, the term $A_L$ denotes the area of the loop antenna (not including the image of the loop.)

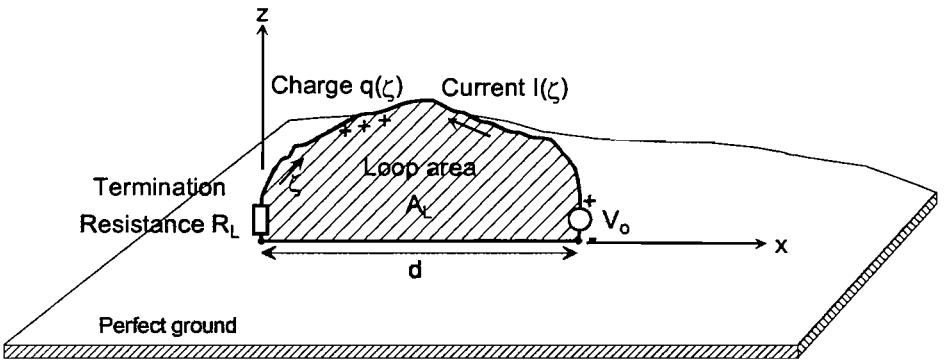


**Figure 1. Geometry of an arbitrary loop over a perfect ground plane.**

The evaluation of the static electric dipole moment is given by the expression [1]

$$\vec{p} = \int_{wire}\vec{r}'\rho(\zeta)d\zeta + \int_{image\ wire}\vec{r}'^{*}\rho^{*}(\zeta)d\zeta \tag{4}$$

where $\rho(\zeta)$ is the per-unit-length charge density on the wire and $\rho^{*}(\zeta) = -\rho(\zeta)$ is the charge density on the image of the conductor. The evaluation of this expression is more difficult than for the magnetic term, since the charge distribution $\rho$ depends on position along the conductor. Unfortunately, simple estimates for the charge on such an arbitrary conductor are not possible, and one must resort to numerical methods to evaluate the distribution.

As discussed in ref. [5], the charge density on the wire can be obtained through the solution of a static integral equation. The electric potential at any observation point $\vec{r}$ may be obtained by integrating over the charge on the wire and its image as

$$\Phi(\vec{r}) = \frac{1}{4\pi\varepsilon_o}\left[\int_{wire}\frac{\rho(\zeta)d\zeta}{|\vec{r}-\vec{r}'|} + \int_{image\ wire}\frac{\rho^*(\zeta)d\zeta}{|\vec{r}-\vec{r}'^*|}\right]. \qquad (5)$$

By letting $\vec{r}$ approach the wire conductor and imposing the potential condition that $\Phi(\vec{r}) = V_o$ everywhere on the conductor[1], an integral equation for the charge results. This integral equation can be solved numerically by the moment method [6], and involves representing the charge densities by $n$ basis (or expansion) functions on the wire and then matching Eq. (5) at $n$ locations on each of the wires. This yields a non-singular ($n\times n$) matrix equation that may be inverted numerically to determine the charge distribution along the wire.

In filling the matrix for the evaluation of the charge, various integrals over the 1/r term in Eq.(5) must be carried out. While these integrations pose no problems as long as the source and observation points are well separated, there is a singularity in the integrand when the source and observation points are coincident. As discussed in ref. [7], such a singularity is integrable, and this leads to rather simple forms for the matrix elements.

Once the charge distribution on the wire is determined, the electric dipole moment follows directly from Eq.(4). Given the fact that the loop is assumed to be contained in the x-z plane, the only non-vanishing component of $\vec{p}$ is $p_z$. By requiring that Eq.(1) be satisfied, we can use Eq.(3) together with the computed value of $p_z$ to evaluate the required load resistance for the loop:

$$R_L = \frac{2A_L V_o}{cp_z} \qquad (6)$$

### *2.2 Use of the Near-Fields to Adjust the E/H Ratio*

Although computing and adjusting the electric and magnetic dipole moments to have the proper ratio is a direct way of obtaining p×m operation of the antenna, it can be difficult to do if the antenna structure is overly complex or if the ground plane is not perfectly conducting. In this latter case it becomes difficult to compute the dipole moments and an alternate method for designing the antenna is needed.

---

[1] Actually, this condition on the potential is correct only for the load resistance and source positions as shown in Figure 4. More generally, the potential of the wire segment between the source and load positions should be set to $V_o$ and zero elsewhere. If the line is loaded with a distributed resistance, then the potential on the line must change continuously, in accordance with the resistive taper, from $V_o$ at the source to zero at the end of the resistance load.

One possible approach is to examine the behavior of the near fields in the primary direction of the p×m radiation, and then adjust the antenna resistance load so that this impedance is approximately equal to the free space impedance of 377 Ω. Figure 6 in ref. [1] has plotted the wave impedance of the primary field quantities (the vertical E-field/horizontal H-field) for a point electric dipole, a point magnetic dipole, and for the point p×m source – all for various values of normalized distance *kr*. The constant impedance level for the p×m source is clearly evident in this figure. Figure 2 illustrates the impedance magnitude for the infinitesimal p×m source plotted as a contour plot for the case of $kr = 0.5$. The location of the main beam of the antenna, where the impedance magnitude is 377 Ω, is noted on the figure.

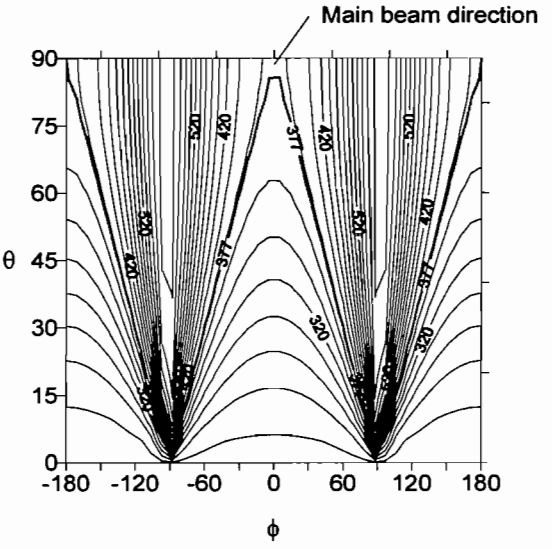


**Figure 2. Plot of the near field wave impedance magnitude for a point p×m source, as a function of the angles $\theta$ and $\phi$ ($kr = 0.5$).**

For a realistic antenna which is not exactly a point source, the near-zone impedance varies with position, as shown in Figure 31 of ref. [1]. Moreover, this impedance will also vary with frequency. A rough rule of thumb is to select a field observation point at a distance of about 2 to 3 times the antenna linear dimension to perform this E/H adjustment.

Another possibility for adjusting the p/m ratio of the antenna is to examine the phase of the wave impedance. As can be noted from Eq.(41a) of [1], in the main beam where $\theta = 90°$ and $\phi = 0°$, the phase of the wave impedance for the point p×m source is exactly zero, regardless of the distance away from the source. Figure 3 plots the contours of phase of the near field wave impedance for a point p×m source as a function of the angles $\theta$ and $\phi$ for the particular special case of $kr = 0.5$. This plot illustrates that in the main beam direction, the phase is indeed zero and slowly decreases as the observation point moves off or the principal field axis.

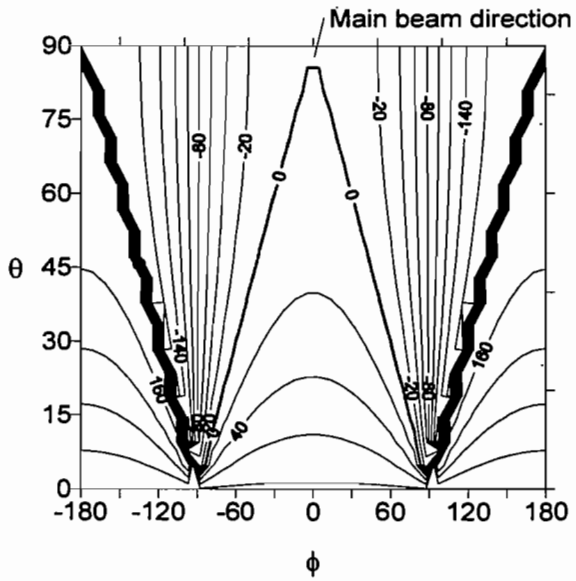


**Figure 3. Plot of the phase of the near field wave impedance for a point p×m source, as a function of the angles $\theta$ and $\phi$ ($kr = 0.5$).**

### *2.3 Detection of the E-field Null in the Backward Direction*

An alternate method for adjusting the antenna load for proper p×m operation is to examine the far-field radiation pattern in the backward (or null) direction. As shown in Figure 28 of ref. [1], a properly tuned p×m transmission line antenna has a null in the primary $E_\theta$ field component in the backward direction. By calculating or measuring this component of the field, the load resistance can be adjusted to minimize this component of the field.

A justification for this approach is found by examining Eq.(36) of [1], which presents an expression for the vector components of the E-field produced by an ideal (infinitesimal) p×m antenna having an electric dipole moment $p_z$ and a magnetic dipole moment $m_y$. Specializing this expression to give the vertical E-field ($E_\theta$), on the ground ($\theta = 90°$) in the backward (i.e., the -$x$-direction where with $\phi = 180°$ and $r = x$ ), gives the expression

$$E_\theta(x) = \frac{j\omega}{4\pi} Z_o \frac{e^{-jkx}}{x}\left[\left(jk + \frac{1}{x}\right)\frac{m_y}{c} + \left(jk + \frac{1}{x} + \frac{1}{jkx^2}\right)p_z\right]. \qquad (7)$$

For the ideal p×m antenna, $p_z$ and $m_y$ are related by $p_z$ = - $m_y$ /$c$, and the expression for the field in the backward direction becomes

$$E_\theta(x) = \frac{j\omega}{4\pi} Z_o \frac{e^{-jkx}}{x}\left(\frac{1}{jkx^2}\right)p_z, \qquad (8)$$

However, if the load resistance is not correctly set, the ratio $-m_y / c\, p_z = \alpha$ which is different from unity, and the resulting E-field is

$$E_\theta(x) = \frac{j\omega}{4\pi} Z_o \frac{e^{-jkx}}{x}\left[(1-\alpha)\left(jk + \frac{1}{x}\right) + \frac{1}{jkx^2}\right] p_z \ . \qquad (9)$$

Notice that for very low frequencies ($kx \ll 1$) , the quasi-static $1/jkx^2$ term in Eq.(7) is dominant, and the $E_\theta$ field does *not* depend on the magnetic dipole moment at all. Furthermore, it can be shown that for this case, the E-field in the forward direction is essentially the same as that in the backward direction. This gives rise to the symmetric $E_\theta$ field plot, as illustrated in Figure 4 of [1]. As the frequency increases to the point where $kx \approx 1$, the term $(1-\alpha)jk$ in Eq.(9) becomes important, and imbalance in the dipole moments becomes noticeable in the backward field behavior.

Thus, the method for determining the proper load resistance of the p×m antenna is clear. The vertical E-field must be measured in the *backward* direction at a distance (or frequency) at which $kx > 1$, and the load resistance varied until the E-field is ***minimized.***

## 3. Design Data for Various P×M Antenna Structures over a Perfect Ground

For an antenna located over a perfectly conducting ground plane, the static calculations of the electric and magnetic dipole moments provide the simplest way of determining the correct load resistance for p×m operation. Using this approach, it is possible to develop design curves for several different types of antenna shapes. In most cases discussed here, the antennas are assumed to be driven at one end by a voltage source and loaded at another end by a termination resistance $R_L$. The only exception is for the half toroidal antenna, which has a uniformly distributed resistance load. Aside from these load resistances, it is assumed that there are no other losses in the antenna.

### *3.1 The Transmission Line P×M Antenna*

To illustrate the preceding discussion with a numerical example, consider the transmission line p×m structure that was discussed in ref. [1]. The geometry of this line is illustrated in Figure 4, and the following parameters are assumed: $d$ = base length of the line = 30 m, $h$ = line height = 3 m, and $a$ = wire radius = 0.1 cm. This provides a total conductor length $L$ = 36 m.

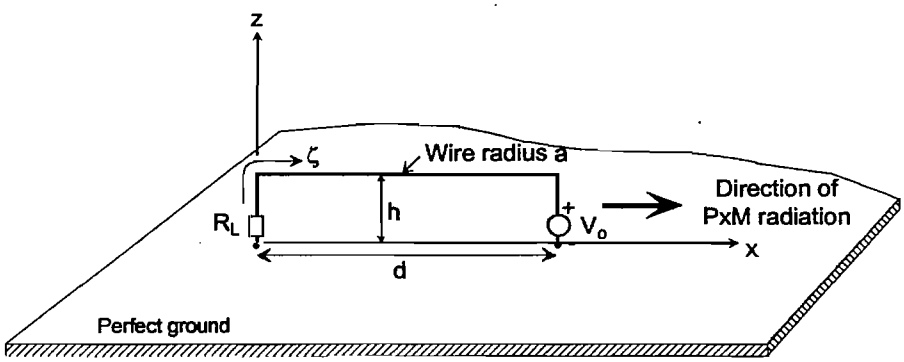


**Figure 4. The transmission line p×m antenna.**

By applying the integral equation (5) to this geometry, the solution for the charge on the conductors may be found. Figure 5 shows the linear charge density $\rho$ as a function of the distance parameter $\zeta$, normalized by the value $c/V_o$ In this manner, the quantity being plotted has the dimensions (Coulombs/s)/V or Siemens.

Observe that while the charge density is approximately constant along the horizontal wire, there are significant variations at the ends of the wire. Moreover, there is a small localized dip of the charge on the conductors right at the 90° bends. This decrease in the charge is consistent with the incremental negative lumped capacitance used to represent a bend in a transmission line [8].

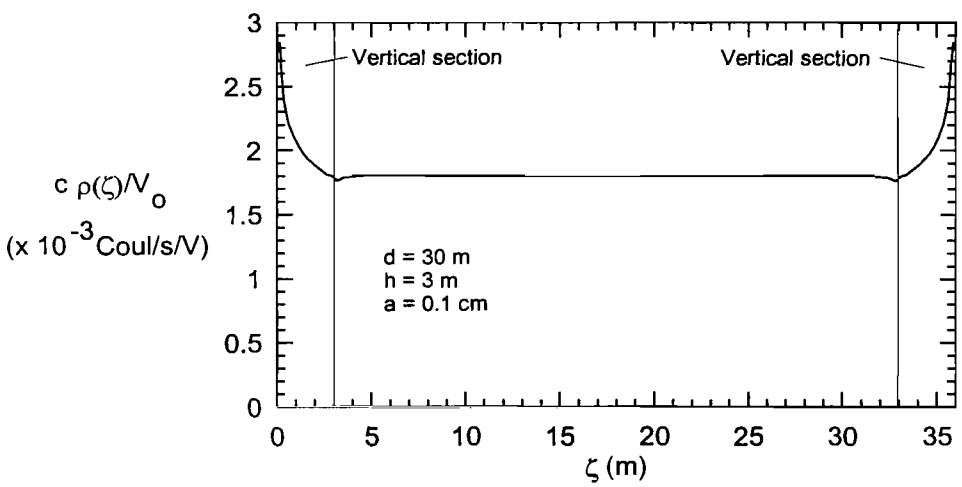


**Figure 5. Plot of the static normalized per-unit-length charge on the conductors in Figure 4, as a function of distance $\zeta$ along the wires.**

Using this charge distribution to calculate the electric dipole moment and then to compute the required termination resistance for proper p×m operation, it is found that the required resistance is $R_L$ = 502 Ω. This is in contrast to the value of $R_L$ = 522 Ω found in ref.[1] for the same structure using a simple transmission line argument. The reason for

this difference is that the transmission line model does not take into account the effects of the charge densities at the vertical ends of the line.

To provide useful design information for the required load resistance for this type of transmission line antenna, a parametric study involving the three antenna parameters $a$, $d$ and $h$ has been conducted. Three different conductor sizes have been considered: $a$ = 0.01, 0.1 and 1.0 cm, and a number of different values of the conductor height have been used. Figure 6 presents the required load resistance $R_L$ for this antenna for various combinations of the geometrical parameters.

Notice that for lines greater than about 20 meters in length, the variation of the load resistance with line height is not large. However, for shorter lines, there can be a very significant change in resistance as the height varies. This behavior is due to the fact that the charge densities on the vertical ends of the line play a significant role in determining the electric dipole moment for short lines. As the line becomes longer, it is the charge on the horizontal section of line that becomes more important.

It is useful to examine the behavior of the dipole moments $cp_z$ and $m_y$ as the frequency increases from DC to a point where the antenna is comparable to a wavelength. As noted in ref. [1] representing the antenna by these dipole moments is accurate at low frequencies where quasistatic assumptions are valid. But as the frequency increases, the higher order moments of the current and charge begin to dominate, and the fields produced by the antenna begin to deviate from the desired cardioid pattern of the ideal p×m antenna.

To gain a better understanding of the high-frequency behavior of the dipole moments, the NEC code [9] can be used to calculate the induced current and charge distributions on the antenna structure using an integral equation solution. Once these source distributions are known, a separate calculation can be performed to evaluate the integrals in Eqs.(2) and (4) to find the dipole moments.

Using the same 30 meter long transmission line examined in ref. [1], a series of calculations was performed for the dipole moments with the load resistance taking on values ranging from a short circuit to an open circuit. Figure 7 presents the results of these calculations[2], shown as a function of $kL = 2\pi f L/c$, where $L$ = 36 (m) is the total length of the conductor comprising the line. Part (a) of the figure plots the normalized electric dipole moment magnitude, and part (b) shows the magnitude of the magnetic moment. Part (c) of the figure illustrates the ratio of these magnitudes, which of course, should be unity for proper p×m operation.

---

[2] At very low frequencies, the NEC results are seen to contain anomalous oscillations, especially for the open-circuit or short-circuit cases. This behavior arises from numerical inaccuracies in the matrix definition and solution in the program, and are not part of the actual antenna behavior.

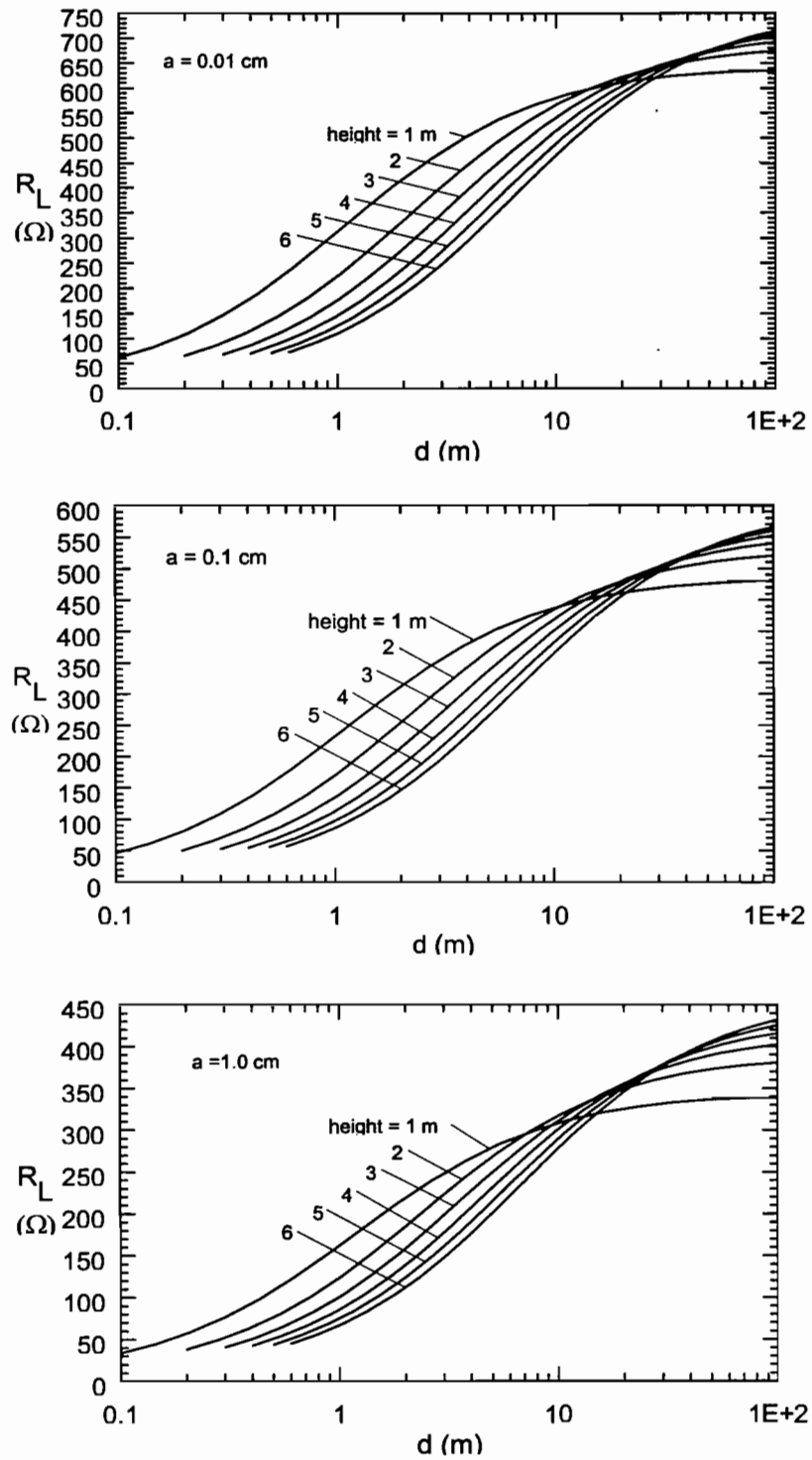


**Figure 6. Load resistance $R_L$ for the transmission line p×m antenna for wire radii $a$ = 0.01, 0.1 and 1.0 cm.**

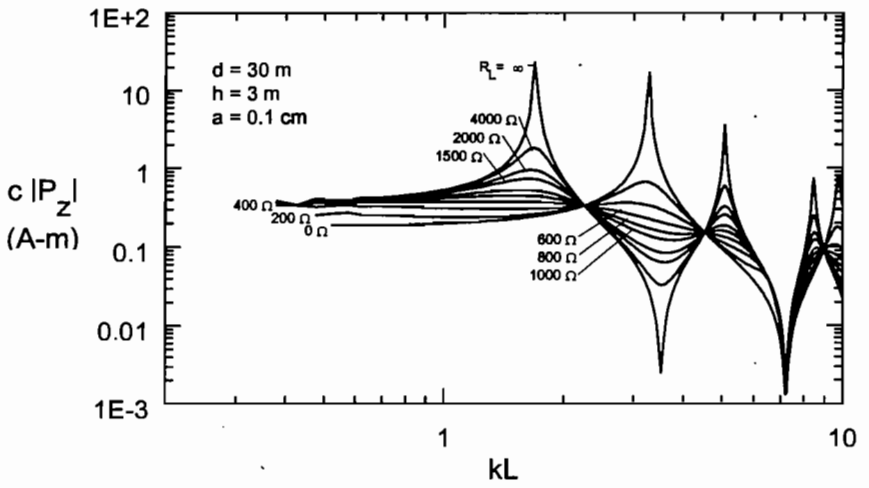


(a) Normalized electric dipole moments.

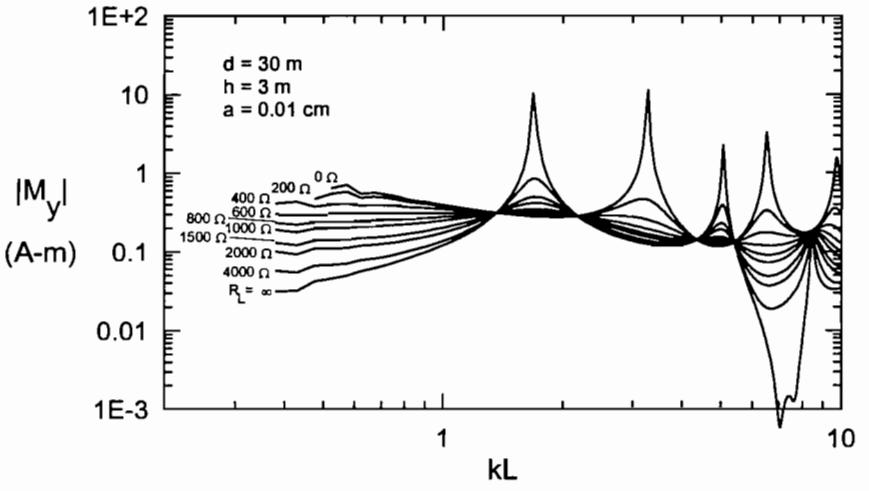


(b) Magnetic dipole moments.

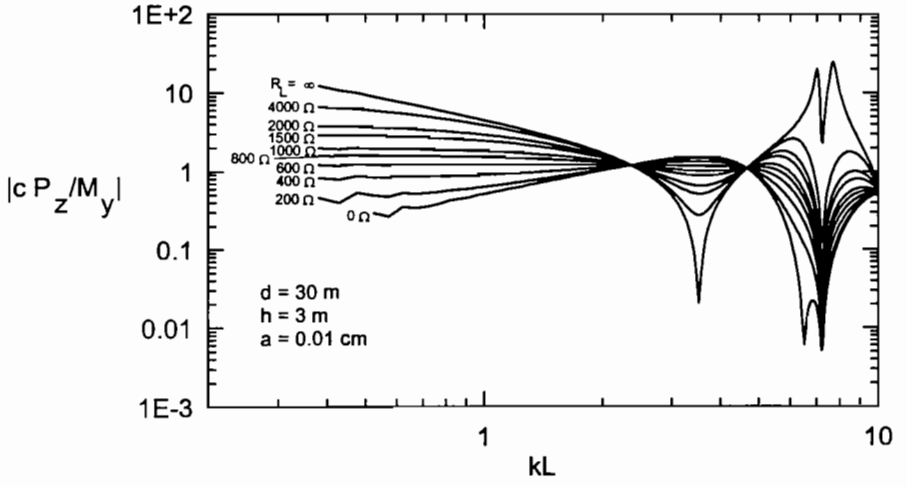


(c) Ratio of dipole moments.

**Figure 7. Dipole moment magnitudes for the p×m transmission line antenna, shown as a function of *kL*.**

Notice that for the open- or short-circuited cases, there are significant resonances and anti-resonances in the dipole moments, a fact that is well known for highly resonant structures. As the load resistance approaches the optimal value of 502 Ω for this geometry, we note that not only does the low-frequency behavior of the dipole moment ratio approach unity, but the excursions of the peak and null values in the high frequency spectrum are minimized.

Figure 8 extracts the dipole moment curves from Figure 7 for the case of optimal termination resistance of $R_L$ = 502 Ω. Note that for frequencies such that $kL < 3$, (i.e., for about f < 4 MHz for the present structure) the imaginary part of the dipole moment ratio is less than the real part, and the antenna appears primarily as a p×m antenna. However, as seen from Figure 28 of ref. [1], the far-field radiation pattern for this antenna with $kL = \pi$ is already significantly different from the ideal p×m cardioid pattern. Thus, a reasonable estimate for the upper limit for p×m radiation from this structure is probably on the order of $kL \approx 1.5 \approx \pi/2$.

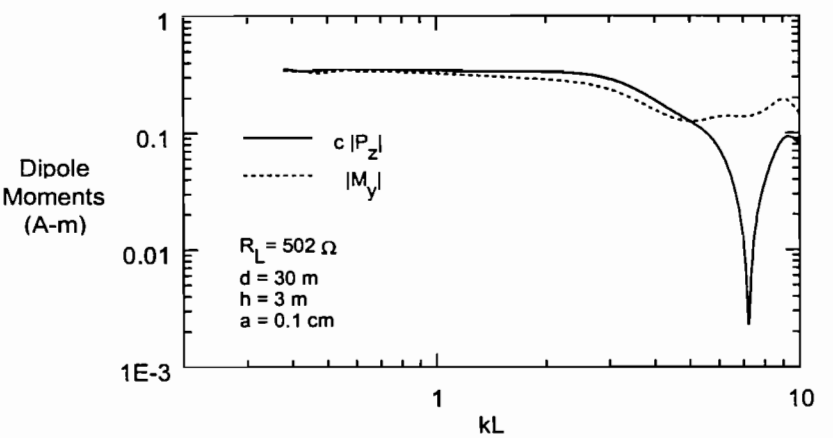


(a) Dipole moment magnitudes

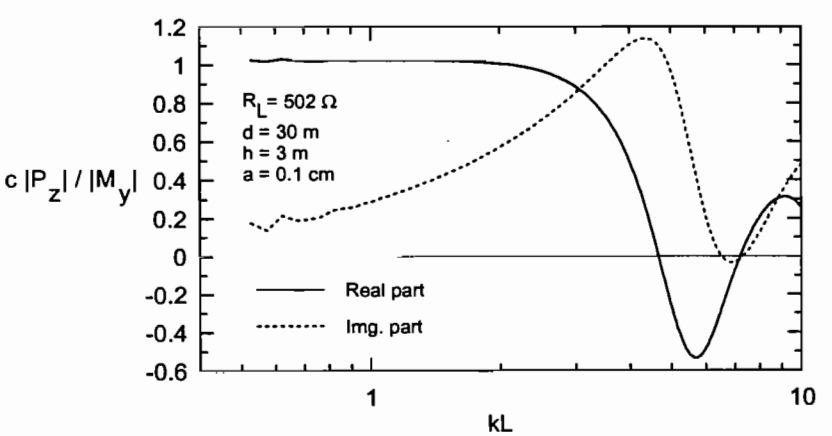


(b) Ratio of the electric to magnetic dipole moment

**Figure 8. Behavior of the dipole moments for the optimally loaded p×m transmission line antenna.**

It is interesting to examine the behavior of the wave impedance in the main beam of the p×m antenna as the frequency changes. Figure 9 provides surface and contour plots of the wave impedance magnitude $|Z_w|$ in the forward direction of the transmission line p×m antenna at the location $(x, y, z) = (60, 0, 0)$ meters in the main beam. This surface is shown as a function of both the normalized frequency $kL$ and the antenna load resistance $R_L$. The thick dotted line denotes the load resistance value of 502 Ω which is calculated from the static dipole moments. The thick contour line is the 377 Ω impedance level for the fields, and it is seen that the 502 Ω resistance level provides an acceptable impedance level even at this near-field location.

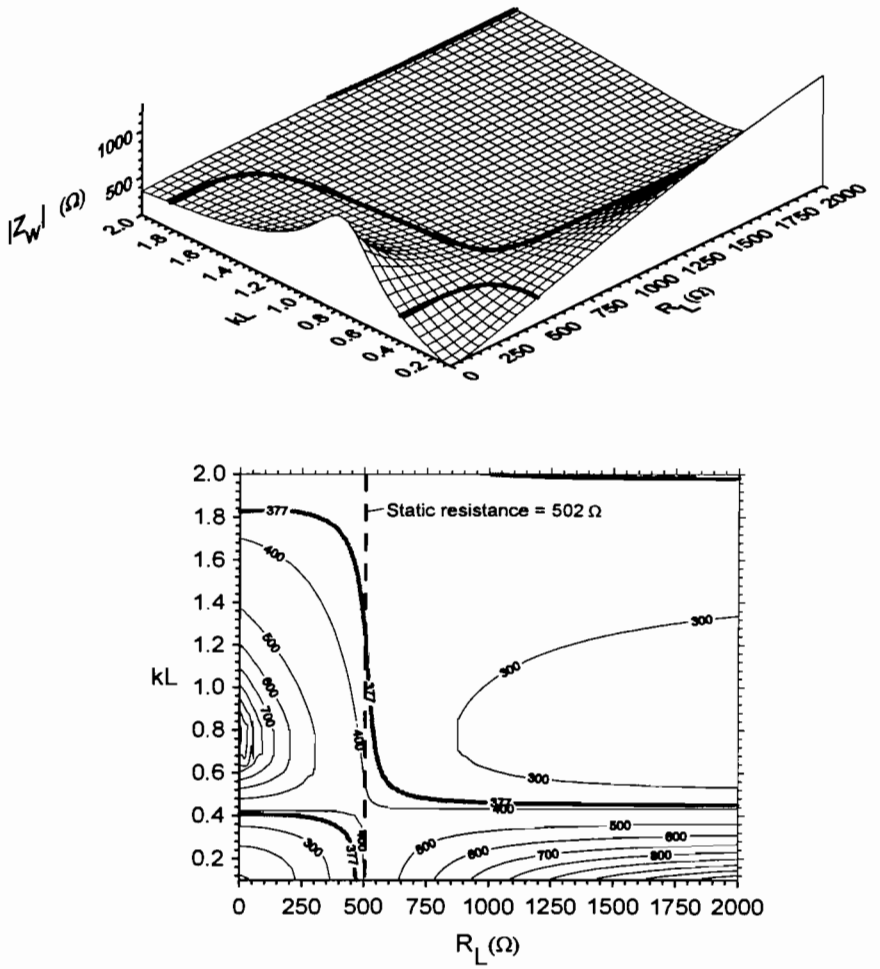


**Figure 9. Surface and contour plots of the wave impedance magnitude $|Z_w|$ in the forward direction at a location $(x, y, z) = (60, 0, 0)$ m for the transmission line p×m antenna of Figure 4.**

### *3.2 The Triangular Wire Antenna*

A variation of the transmission line p×m antenna is the triangular wire antenna shown in Figure 10. From a practical standpoint, this type of antenna is easier to deploy in the field, as only one support post is necessary. However, for a fixed height and base distance, the loop area is ½ that of the transmission line antenna, with a subsequent reduction of the dipole moments.

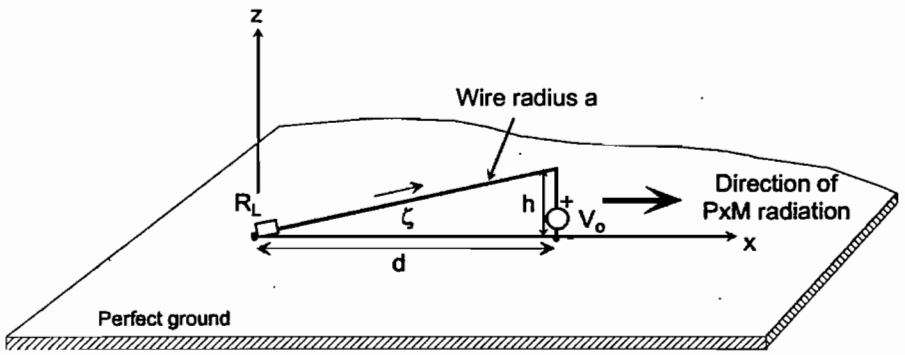


**Figure 10. Geometry of the triangular wire antenna.**

Figure 11 presents typical behavior of the static charge distribution on this antenna for the case of a base length $d = 30$ m, height $h = 6$ m and radius $a = 0.1$ cm line. This example is chosen so that the antenna has the same cross-sectional area as the transmission line antenna considered earlier. Notice that the charge on the non-vertical section increases smoothly from the top of the antenna down to the load resistance on the ground plane.

Figure 12 summarizes the resulting load resistances for the p×m operation of this antenna for the three different wire radii. Although these plots appear similar in shape to the load curves for the transmission line antenna in Figure 6, we note that there is a difference between the two antennas. For example, for the 6 meter high antenna just mentioned, the optimum loading resistance has been calculated to be 465 Ω, in contrast to the 502 Ω load for the transmission line structure.

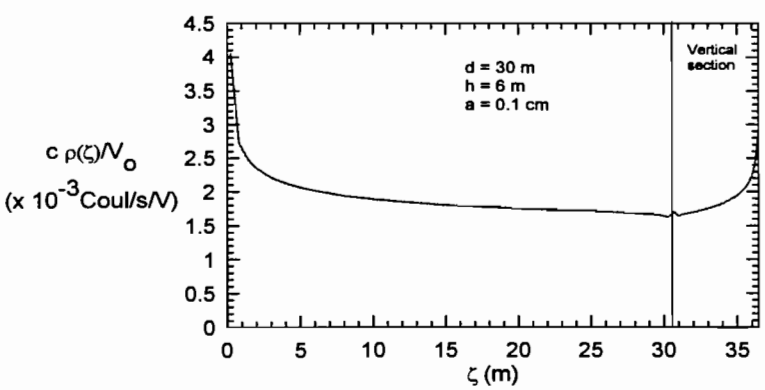


**Figure 11. Plot of the static normalized per-unit-length charge on the conductors in Figure 10, as a function of distance ζ along the wires.**

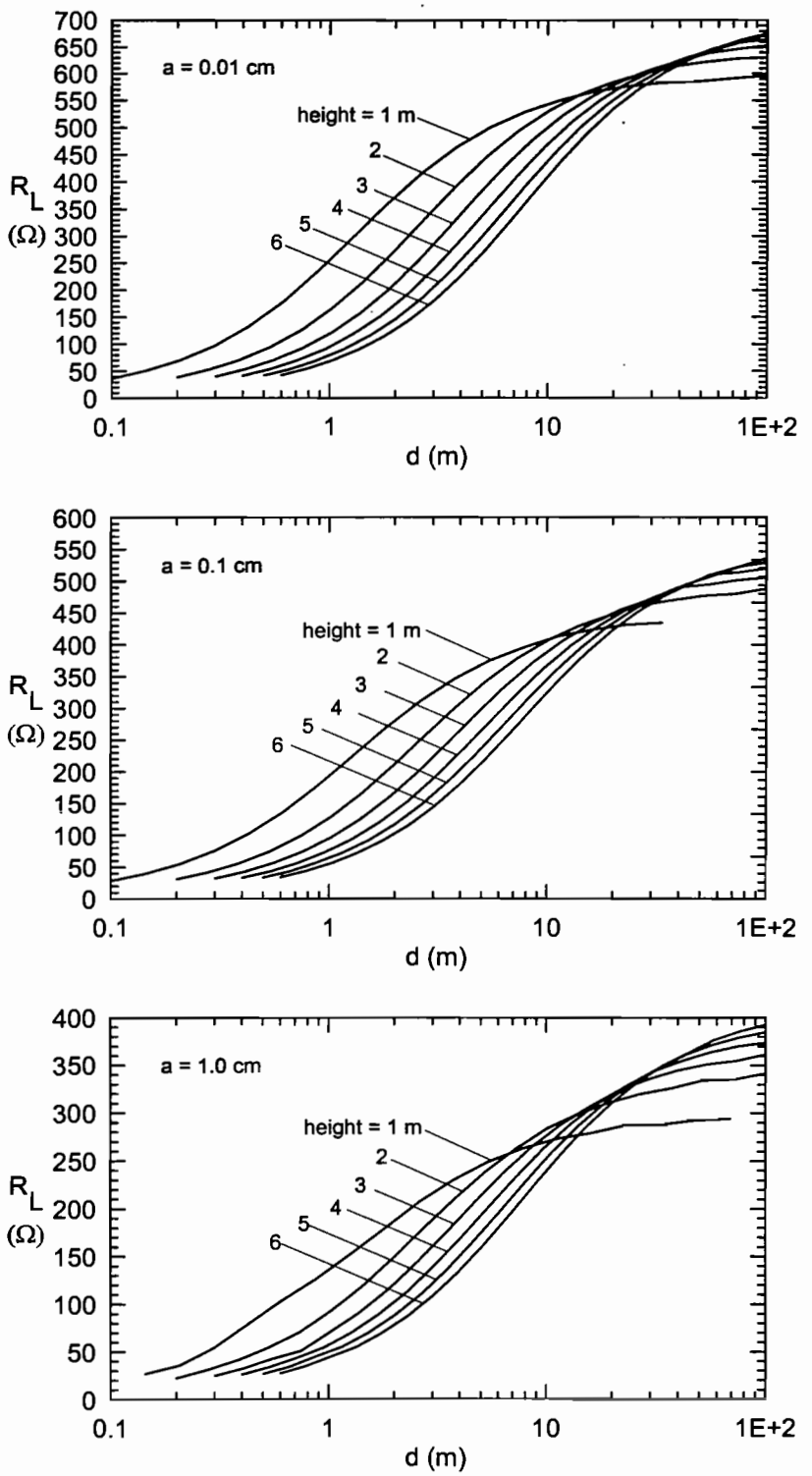


**Figure 12. Load resistance $R_L$ for the triangular wire p×m antenna for wire radii $a$ = 0.01, 0.1 and 1.0 cm.**

Figure 13 illustrates the frequency domain behavior of the magnitude of the dipole moment ratios for the example antenna as the load resistance varies from a short circuit to an open circuit condition. Its behavior is similar to the corresponding ratio for the transmission line structure in Figure 7c, and it is evident that the proper p×m resistance should be around 450 Ω. In this example, the total conductor length is L = 36.59 m.

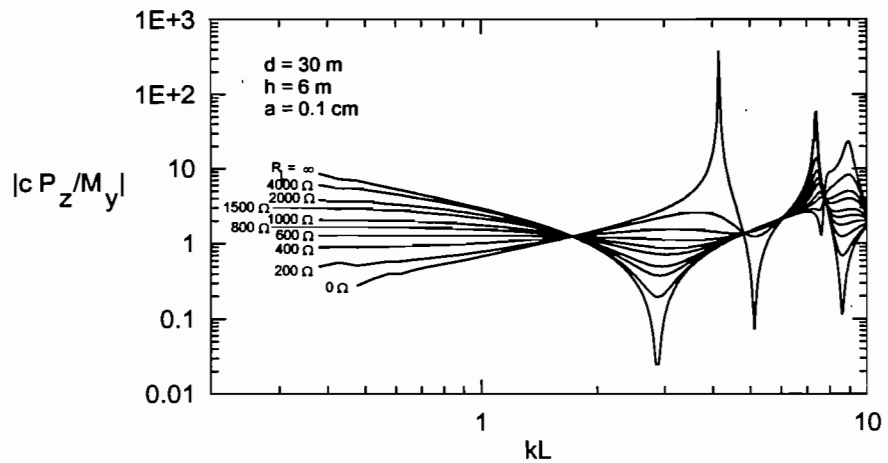


**Figure 13. Dipole moment ratios for the triangular p×m antenna with various load resistances, shown as a function of *kL*.**

Figure 14 shows the real and imaginary parts of the dipole moment ratio for the optimally loaded triangular antenna. Comparing this with Figure 8 for the transmission line antenna, we note that the high frequency excursions of the moment ratio is significantly larger for the triangular wire structure. The reason for this is not evident and it calls for more study.

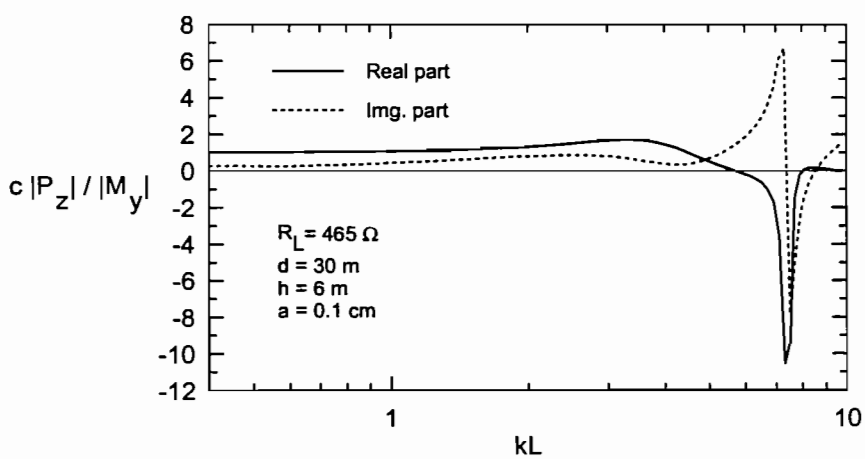


**Figure 14. Behavior of the dipole moment ratio for the optimally loaded triangular p×m antenna.**

The main-beam wave impedance of this antenna is shown in Figure 15. As before, the thick dotted line in these plots denotes the contours for the computed load resistance of 465 Ω.

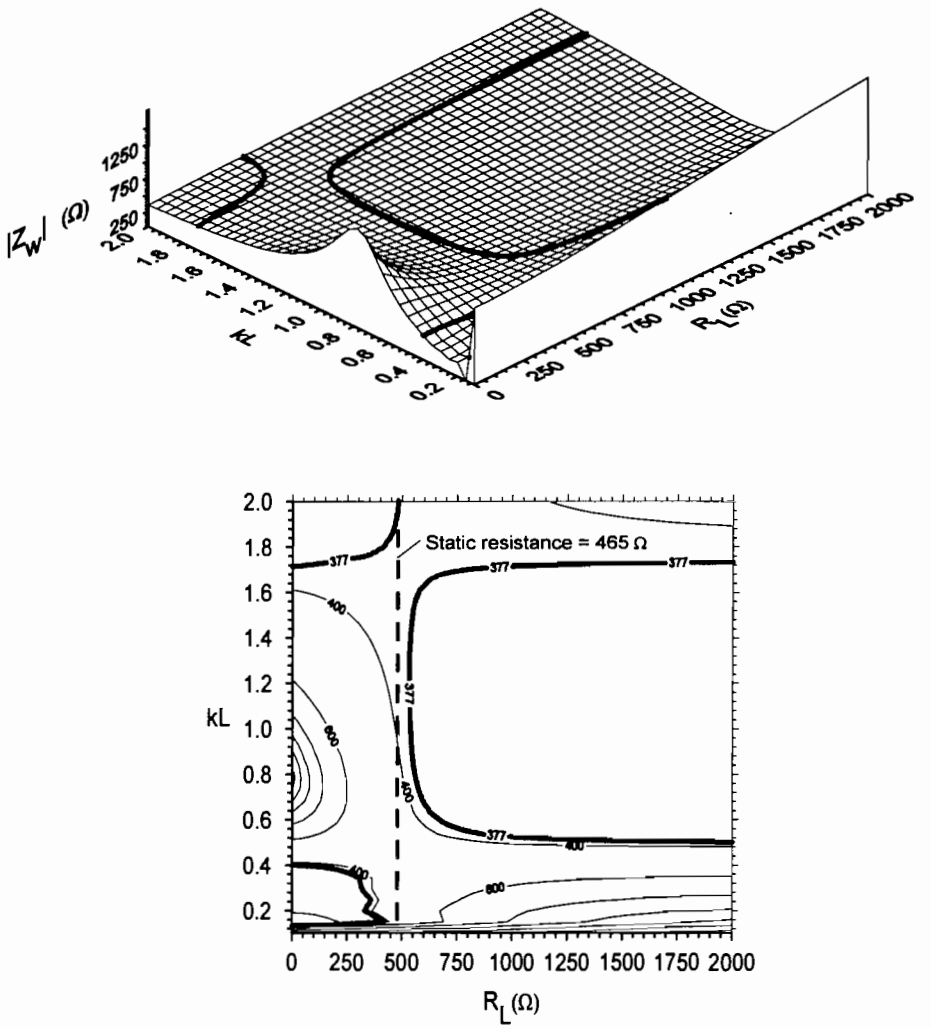


**Figure 15. Surface and contour plots of the wave impedance magnitude $|Z_W|$ in the forward direction at a location $(x, y, z) = (60, 0, 0)$ m for the triangular p×m antenna of Figure 10.**

### *3.3 The Inverted V Antenna*

Another possible p×m antenna geometry is the inverted V structure shown in Figure 16. It is supported at the wire midpoint by a nonconducting post, with both the load and the source at the wire ends on the groundplane. For this antenna, it is expected that the static charge distribution will be symmetric about the middle of the wire, due to the structural symmetry. The charge calculation shown in Figure 17 confirms this fact.

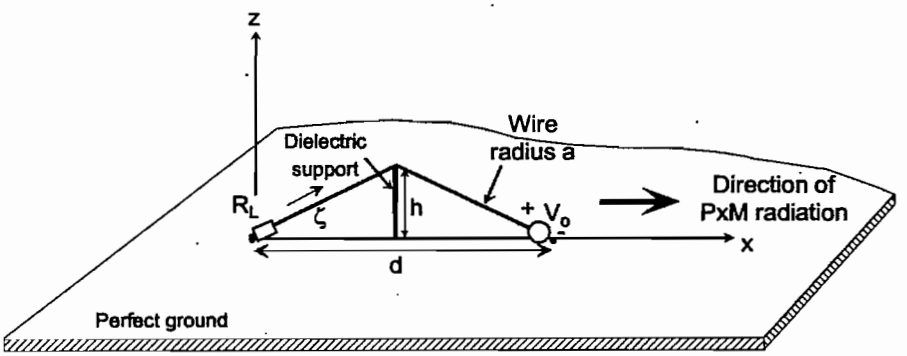


**Figure 16. Geometry of the inverted V antenna.**

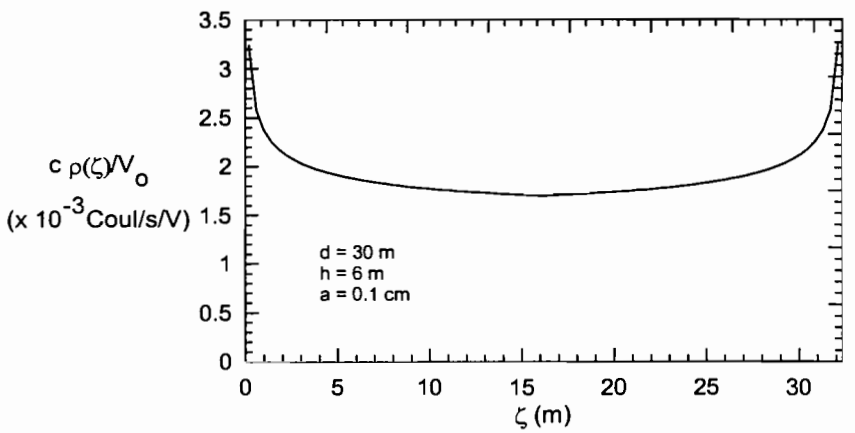


**Figure 17. Plot of the static normalized per-unit-length charge on the conductors in Figure 16, as a function of distance ζ along the wires.**

For this antenna, the same set of response plots as provided for the triangular antenna are presented. Figure 18 summarizes the design curves for the p×m load resistance for this structure, Figure 19 presents the magnitude of the dipole moment ratios for various load resistances on a special case of this antenna ($d$ = 30m, h = *6* m and $a$ = 0.1 cm), and finally, Figure 20 presents the frequency behavior of the dipole moment ratios for the optimal resistance loading of $R_L$ = 521 Ω. The main beam wave impedance of this antenna is shown in Figure 21, with the thick dotted line denoting the computed load resistance of 521 Ω.

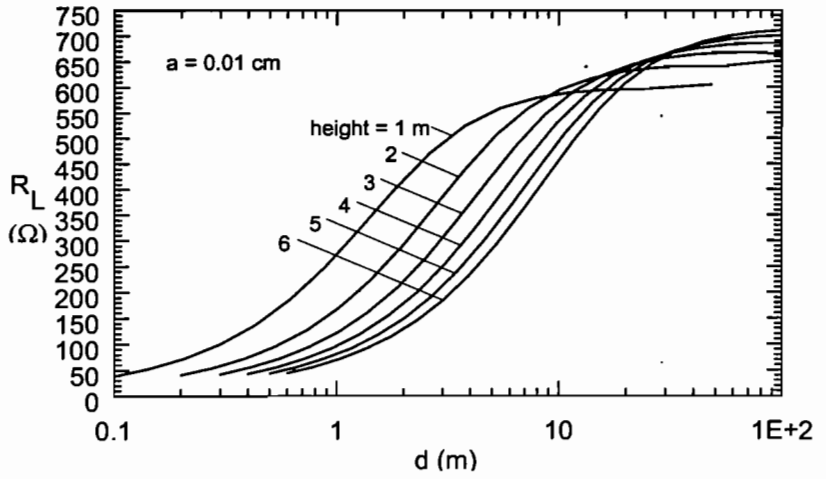


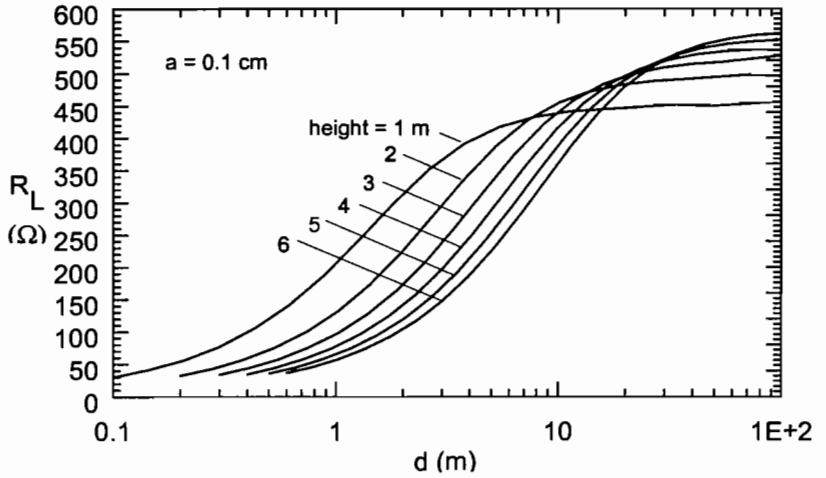


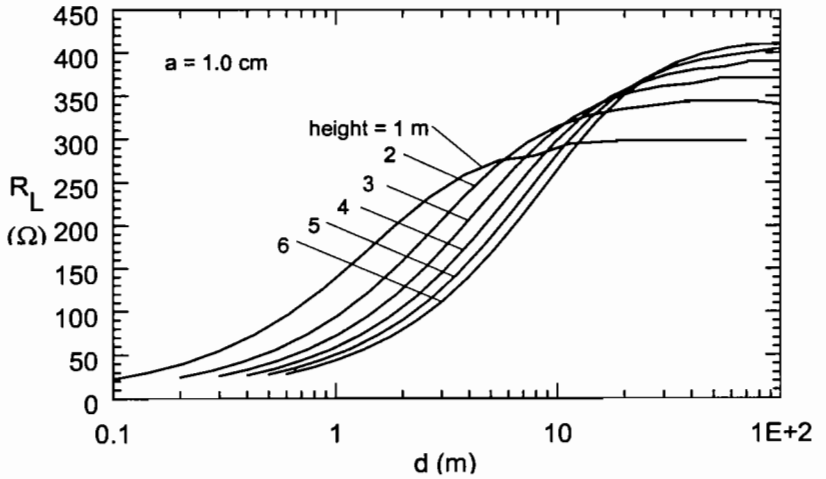


**Figure 18. Load resistance $R_L$ for the inverted V antenna for wire radii $a$ = 0.01, 0.1 and 1.0 cm.**

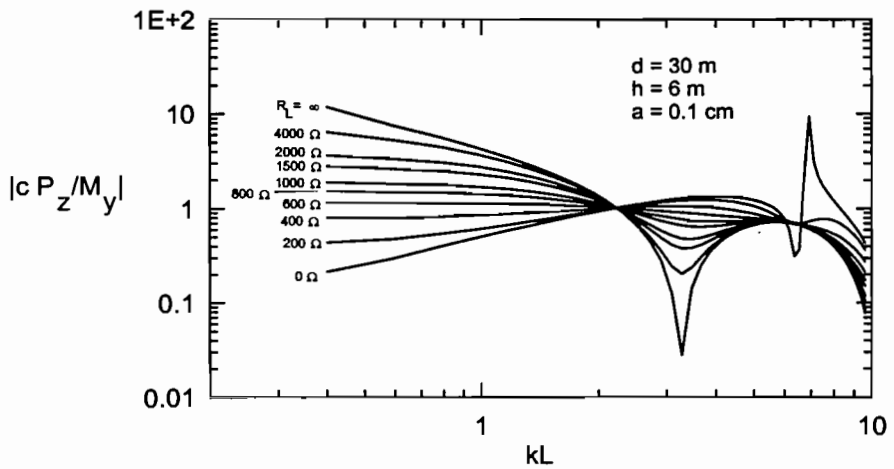


**Figure 19. Dipole moment ratios for the inverted V antenna with various load resistances, shown as a function of *kL*.**

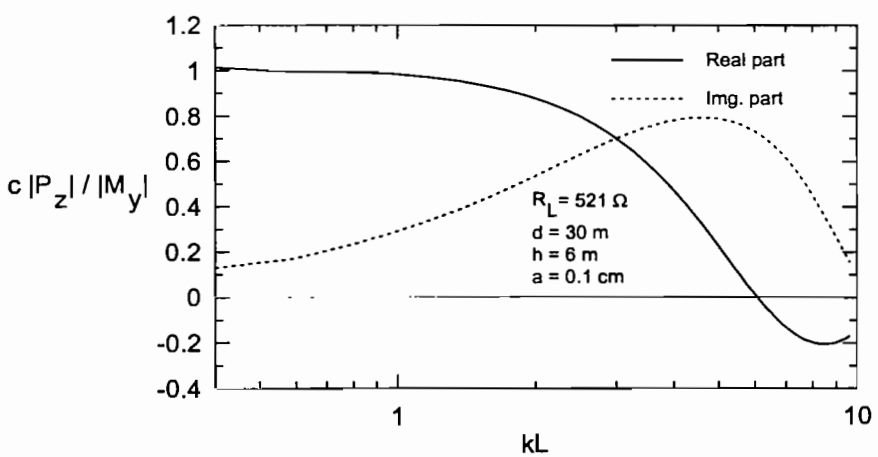


**Figure 20. Behavior of the dipole moment ratio for the optimally loaded inverted V antenna.**

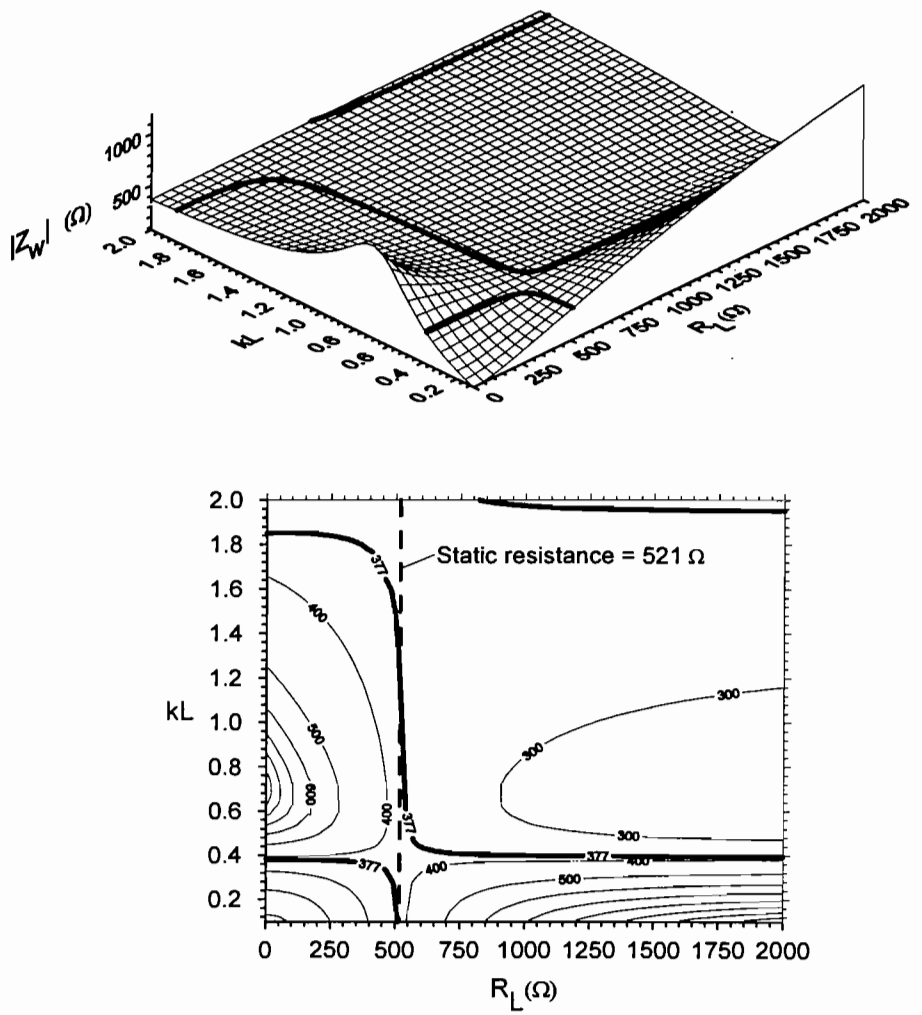


**Figure 21. Surface and contour plots of the wave impedance magnitude $|Z_W|$ in the forward direction at a location $(x, y, z) = (60, 0, 0)$ m for the inverted V antenna of Figure 16.**

It is interesting to examine the behavior of the phase of the wave impedance in the forward direction for this antenna. As discussed earlier, the phase of $Z_W$ in the main beam is zero for a point p×m source, even in the near field. For an extended antenna, we expect that this phase will deviate slightly, due to the extended nature of the antenna. Figure 22 presents the calculated phase of the wave impedance at the same location as in Figure 21, with the heavy line representing the zero phase contours. Notice that the load resistance with the best fit for zero phase for a wide range of frequencies is $R_L \approx 521\ \Omega$, which is the same value as obtained from the impedance magnitude plots in Figure 21.

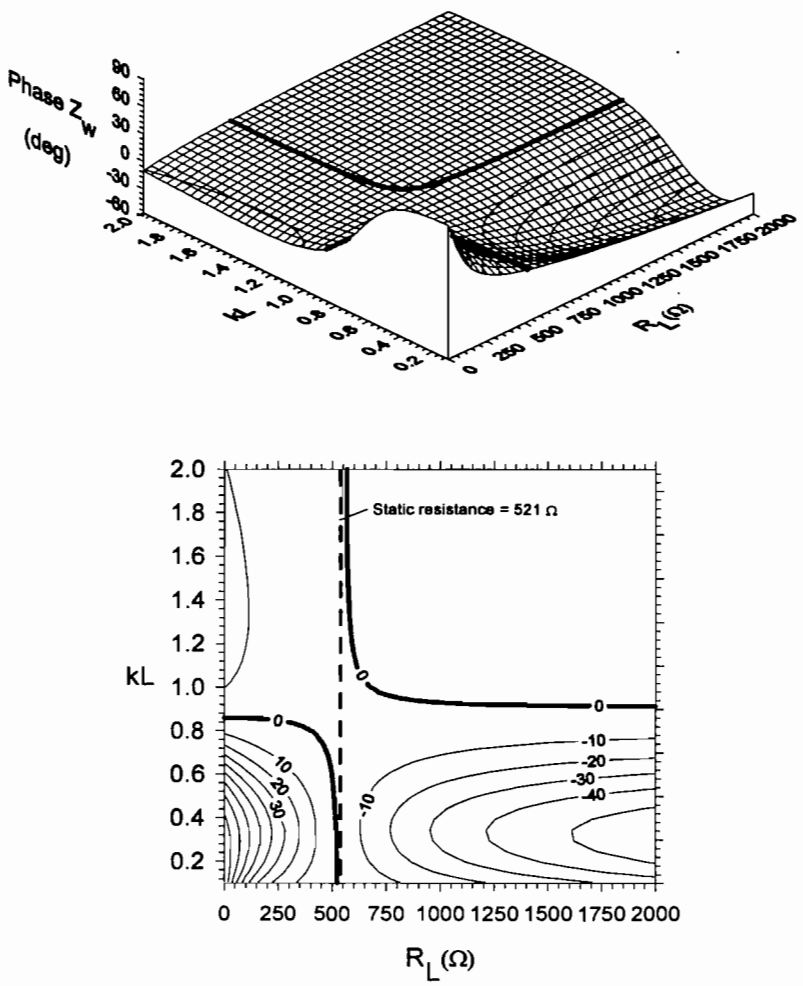


**Figure 22. Surface and contour plots of the phase of the wave impedance $Z_W$ in the forward direction at a location $(x, y, z) = (60, 0, 0)$ m for the inverted V antenna of Figure 16.**

### *3.4 The Half-Toroidal Antenna*

A commonly used antenna configuration for EMP testing is a half-toroidal antenna [10]. Loop antennas have been analyzed in[11], [12], and [13] and these references provide insight into the p×m operation of the antenna. Unlike the previous structures, this antenna is described by only two parameters: the loop diameter $d$ (or equivalently, its radius $b$) and the wire radius $a$. From a practical standpoint, however, this structure is not very practical to realize in the field, as a nonconducting support structure must be used to maintain the toroidal shape.

This antenna can be loaded by a lumped resistance at the connection point to the ground opposite the voltage source, just like the earlier antennas. The TORUS antenna discussed in [11], however, considers a *distributed* resistance along the conducting

structure, and from this reference, one is able to determine analytically the required resistance loading for the loop. In this section, both the distributed resistive load and the lumped resistive load cases are considered for the toroidal antenna. In both cases discussed here, the determination of the optimal resistive load for p×m operation proceeds in the same manner as before — by using a static numerical calculation of the charge on the conductor and then balancing of the dipole moments by adjusting the lumped or distributed resistance. Appendix A summarizes the analysis undertaken in [11], and shows how the proper load resistance for the case of the uniformly distributed impedance loading can be found analytically.

### 3.4.1 Distributed Resistance Loading

The half-toroidal structure under consideration in this section is shown in Figure 23. A uniformly distributed resistance R' is located along the circumference, with a total resistance on the half-loop being

$$R_L = \frac{\pi d}{2} R' \ (\Omega). \tag{10}$$

Because there is no lumped load at the end of the antenna opposite the source, the potential on the wire at this point is essentially the same as the reference conductor. Consequently, we expect only a small charge on the wire at the end of the wire. The major portion of the charge occurs in the vicinity of the source. Figure 24 shows the numerically calculated charge distribution for the special case of a large loop with diameter $d = 12$ m and a wire radius $a = 0.1$ cm.

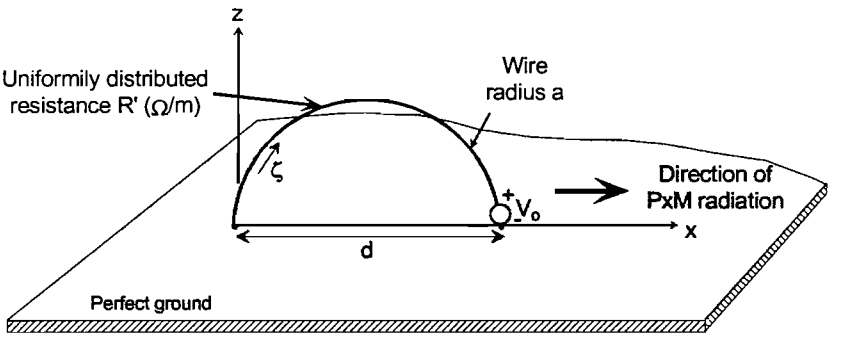


**Figure 23. Geometry of the uniformly loaded toroidal antenna.**

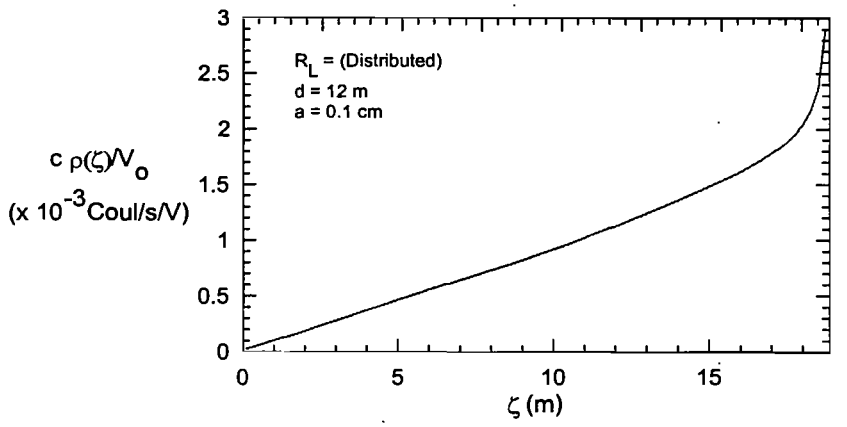


**Figure 24. Plot of the static normalized per-unit-length charge on the conductors in Figure 23 for uniformly distributed resistance loading, as a function of distance $\zeta$ along the wires.**

Figure 25 presents the computed optimum lumped resistance loading for the half loop structure as a function of the loop diameter for different radii. In Appendix A, it is shown that the optimum resistance loading on a half-loop structure for the case of a uniformly distributed resistance should be

$$R_L = \frac{Z_o}{4}\left(\ln\left(\frac{8b}{a}\right) - 2\right) \ (\Omega) \tag{11}$$

where $b$ is the radius of the half-loop. For the 12 meter loop, the theoretical value of the load impedance is $R_L$ = 827 Ω. In comparison, the numerically calculated value of resistance is $R_L \approx$ 876 Ω. This difference can be attributed to inaccuracies in integrating the singular contribution of the charge density near the source to compute the electric dipole moment.

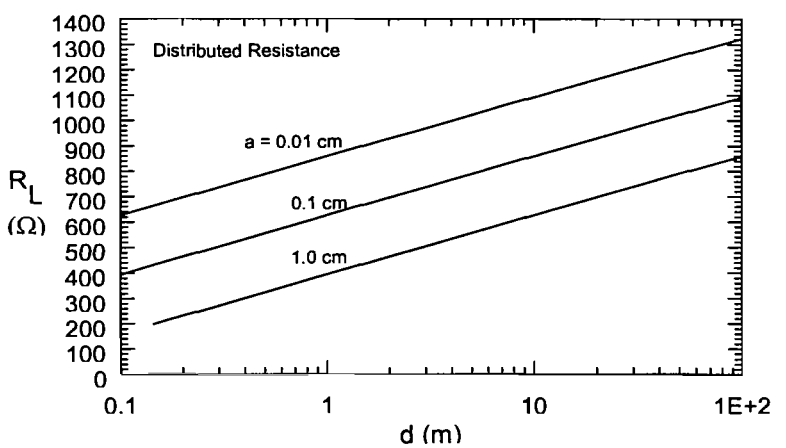


**Figure 25. Total distributed load resistance $R_L$ for the half toroidal loop of diameter $d$ for wire radii $a$ = 0.01, 0.1 and 1.0 cm.**

Figure 26 presents the magnitude of the dipole moment ratios for different load resistances for the example case of this antenna ($d$ = 12m, $a$ = 0.1 cm), and we see that a total half-loop load resistance somewhere between 800 and 900 Ω is needed. Using the numerically calculated value of $R_L$ = 876 Ω, Figure 27 presents the frequency behavior of the dipole moment ratios for the optimal resistance loading.

Figure 28 plots the main beam wave impedance of this antenna, with the computed load resistance of 876 Ω illustrated by the thick dotted line.

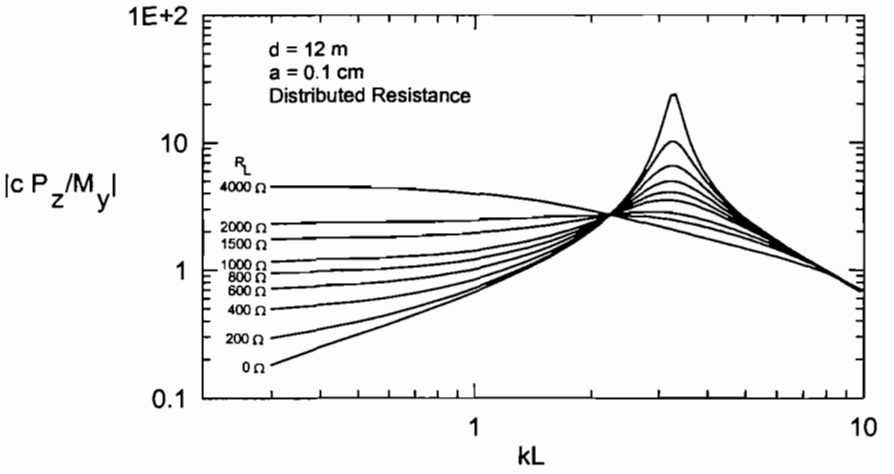


**Figure 26. Dipole moment ratios for the toroidal V antenna with various distributed load resistances, shown as a function of *kL*.**

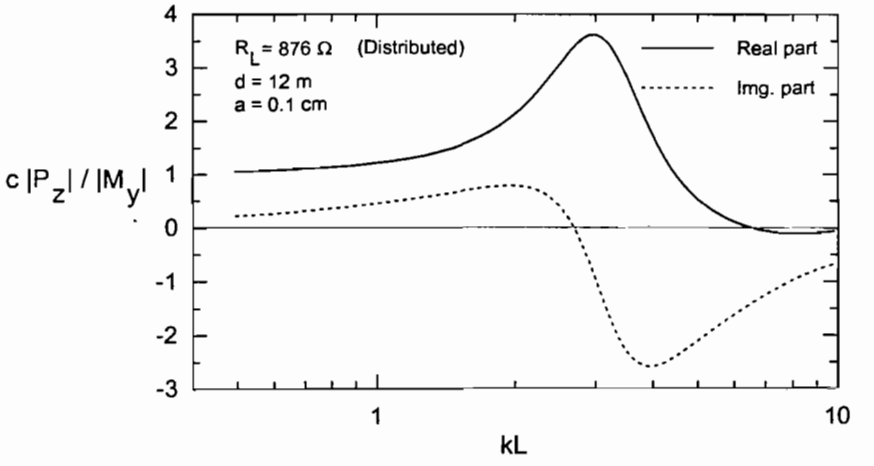


**Figure 27. Behavior of the dipole moment ratio for the optimally loaded toroidal antenna with distributed resistance.**

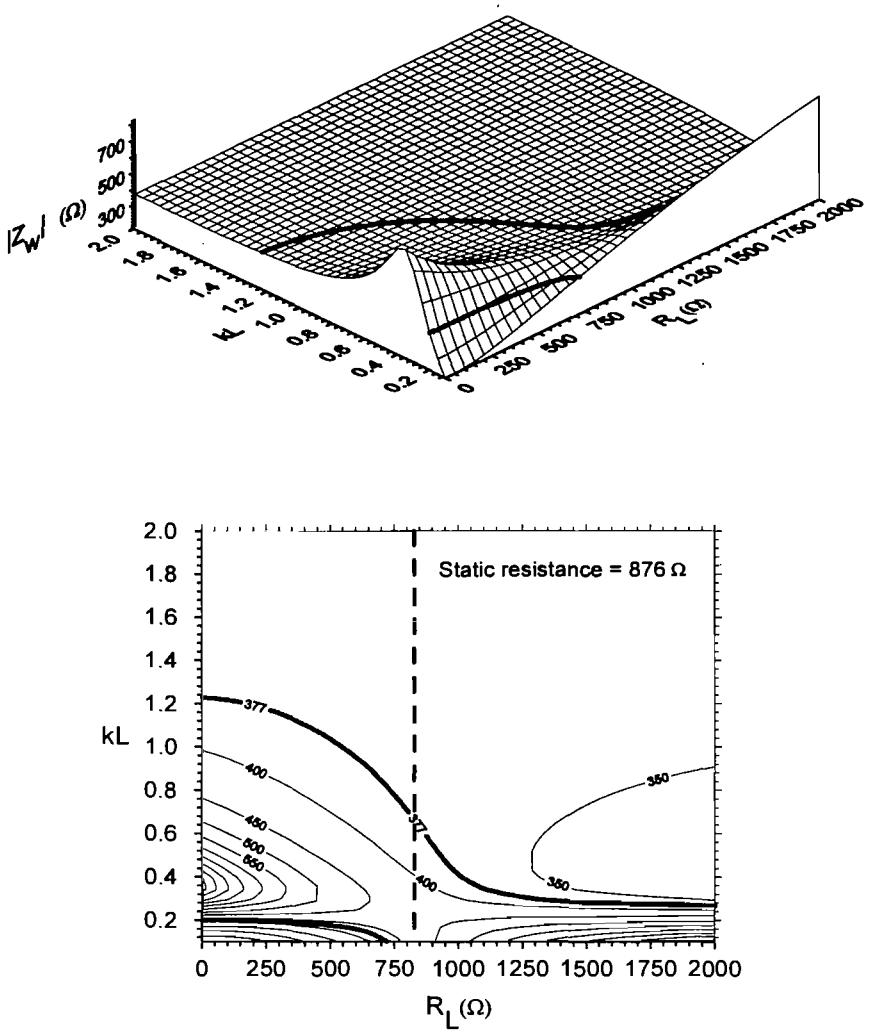


**Figure 28. Surface and contour plots of the wave impedance magnitude $|Z_W|$ in the forward direction at a location $(x, y, z) = (60, 0, 0)$ m for the uniformly loaded half-toroid antenna of Figure 23.**

### 3.4.2 Lumped Resistance on the Antenna

Figure 29 shows the geometry of this antenna, with a lumped load $R_L$ at one side of the half-loop, and the source on the other side. This structure is similar of the inverted V antenna of Figure 16 and consequently, we expect that the charge distribution on the antenna will be symmetric about the middle of the loop. This is confirmed in Figure 30 where the computed charge for the lumped load case is presented for the case of a 12 m diameter loop with a wire radius of 0.1 cm.

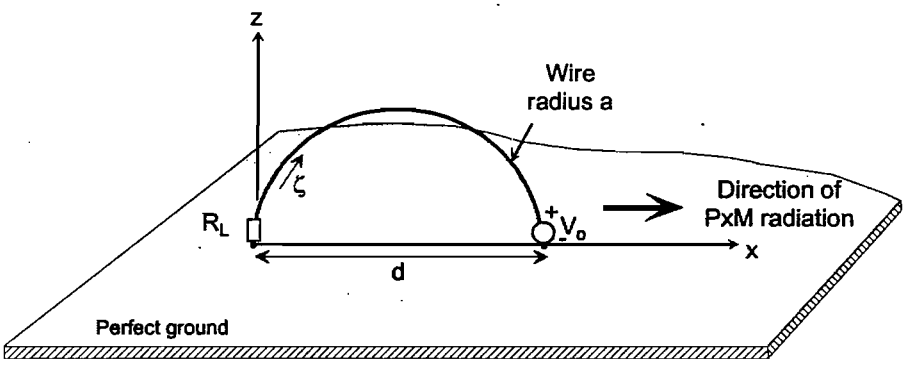


**Figure 29. Geometry of the resistively loaded toroidal antenna.**

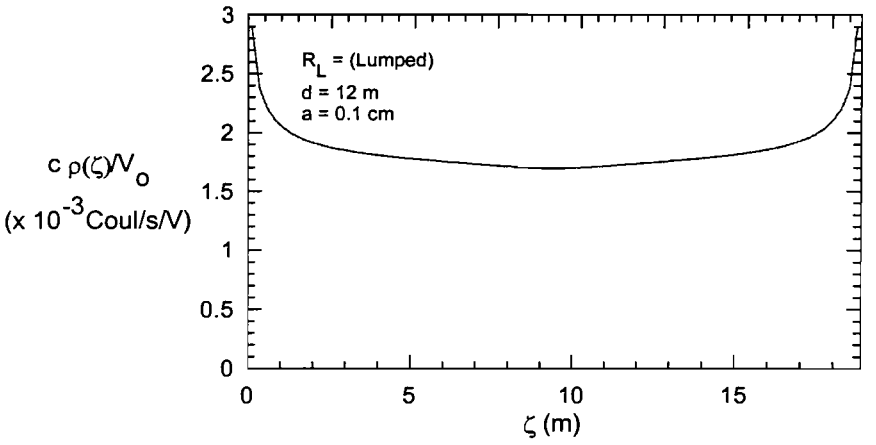


**Figure 30. Plot of the static normalized per-unit-length charge on the conductors in Figure 29 for lumped resistance loading, as a function of distance ζ along the wires.**

Figure 31 presents the calculated lumped resistance loading for the loop of diameter *d*. It is interesting to observe that this value of resistance is approximately ½ that needed for the distributed loading case. Unfortunately, it is not possible to get a simple closed-form expression for the optimum load resistance because, as discussed by Smith [13], all of the modes on the loop are coupled together and this results in an infinite set of modal coefficients that must be determined. One should remember, however, that only the lowest order modes static modes need to be evaluated.

The dipole moment ratio for the 12 meter loop antenna is shown in Figure 32 for varying load resistances, and a value of between 400 and 500 Ω is seen to be needed. The numerically calculated value was $R_L \approx 443\ \Omega$, and Figure 33 uses this value to compute the dipole moment ratio for the special example of the loop antenna.

Figure 34 plots the main beam wave impedance of this antenna, with the computed load resistance of 443 Ω illustrated by the thick dotted line.

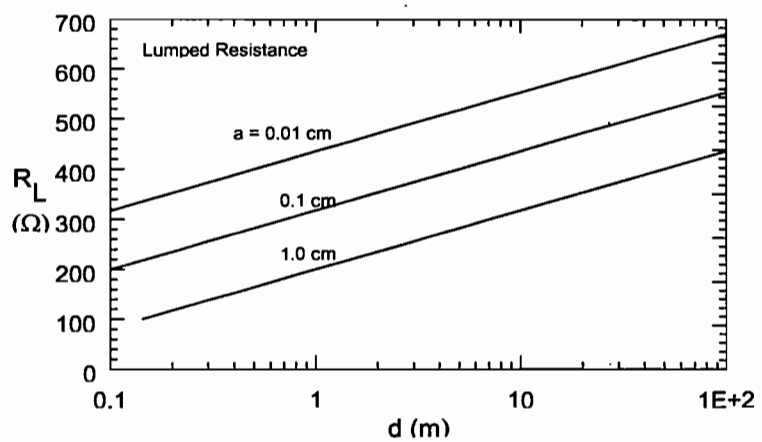


**Figure 31. Lumped load resistance $R_L$ for the toroidal loop of diameter $d$ and wire radii $a$ = 0.01, 0.1 and 1.0 cm.**

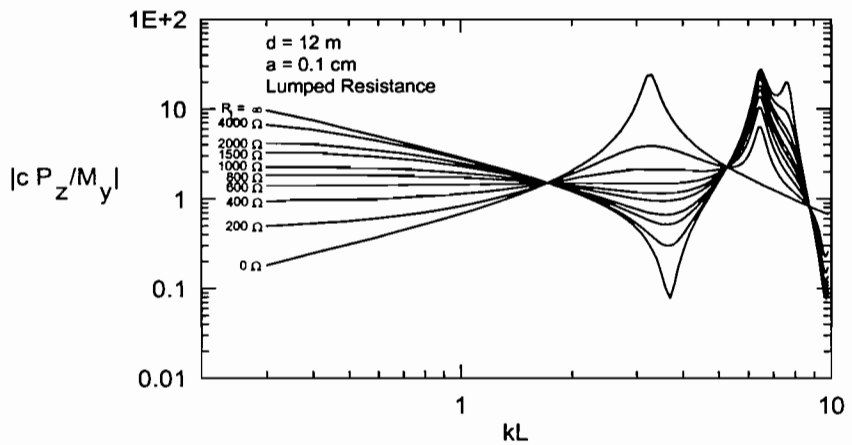


**Figure 32. Dipole moment ratios for the toroidal V antenna with various lumped load resistances, shown as a function of $kL$.**

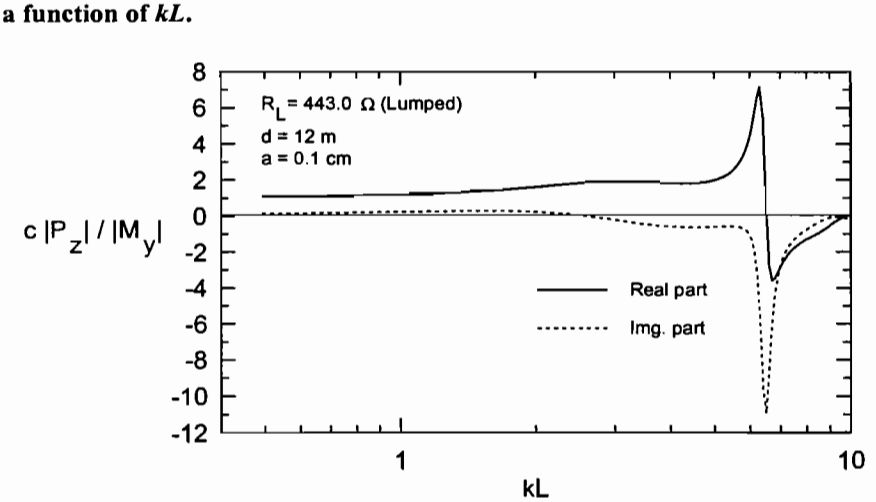


**Figure 33. Behavior of the dipole moment ratio for the optimally loaded toroidal antenna with lumped resistance .**

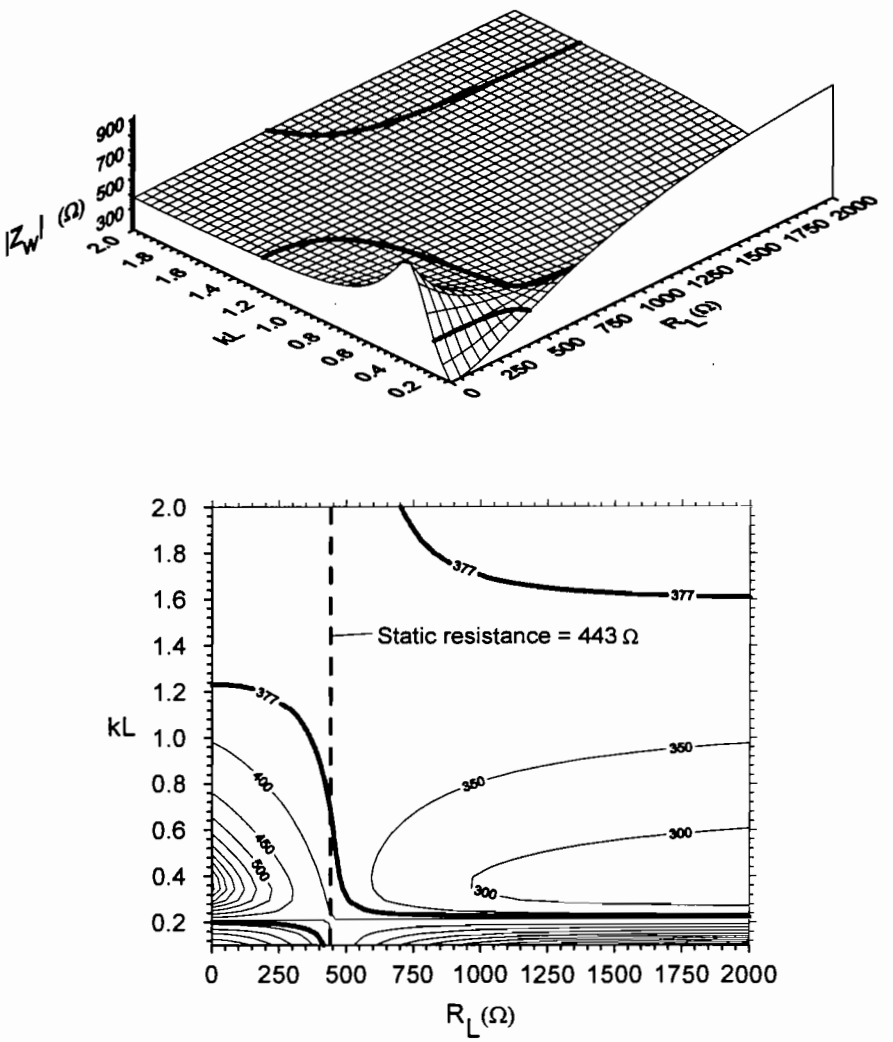


**Figure 34. Surface and contour plots of the wave impedance magnitude $|Z_W|$ in the forward direction at a location $(x, y, z) = (60, 0, 0)$ m for the half-toroid antenna of Figure 29 with a lumped load.**

### *3.5 Comparison of Antenna Responses*

It is useful to compare the responses of the above antennas on a common basis. One way of conducting a comparison is to assume that each antenna has the same loop area $A_{eq}$. In this comparison, we shall assume that the area is 90 $m^2$. Table 1 summarizes the pertinent data for each antenna considered here.

**Table 1 - Geometry and Load Resistance for Sample Antennas**

| Antenna Type | Loop Area $A_{eq}$ (m$^2$) | Base $b$ (m) | Height $h$ (m) | Wire Radius $a$ (cm) | Total Wire Length $L$ (m) | $kL$ at $f=2$ MHz | Load Resistance $R_L$ (Ω) |
|---|---|---|---|---|---|---|---|
| Transmission Line | 90 | 30 | 3 | 0.1 | 36 | 1.50 | 502 |
| Triangular | 90 | 30 | 6 | 0.1 | 36.59 | 1.53 | 465 |
| Inverted V | 90 | 30 | 6 | 0.1 | 32.31 | 1.35 | 521 |
| Loaded Loop (Discrete) | 90 | 15.14 | - | 0.1 | 23.78 | 1.00 | 455 |
| Loaded Loop (Continuous) | 90 | 15.14 | - | 0.1 | 23.78 | 1.00 | 901 |

The frequency selected for illustrating the antenna responses is 2 MHz, which is near the highest frequency for which these antennas can be represented by the first-order electric and magnetic dipole moments. At a low frequency, ref.[1] has noted that the radiation efficiency of p×m antennas is small. Figure 35 presents the radiation efficiency of each of the antennas as a function of frequency. Note that at the p×m frequency limit of about 2 MHz, the efficiency is less than 1 per-cent.

It is interesting to note that the toroidal antenna with a lumped load has the highest radiation efficiency, probably due to the fact that it has the highest elevation over the ground plane. In contrast, the transmission line antenna has the lowest efficiency — a fact that is well known in transmission line theory.

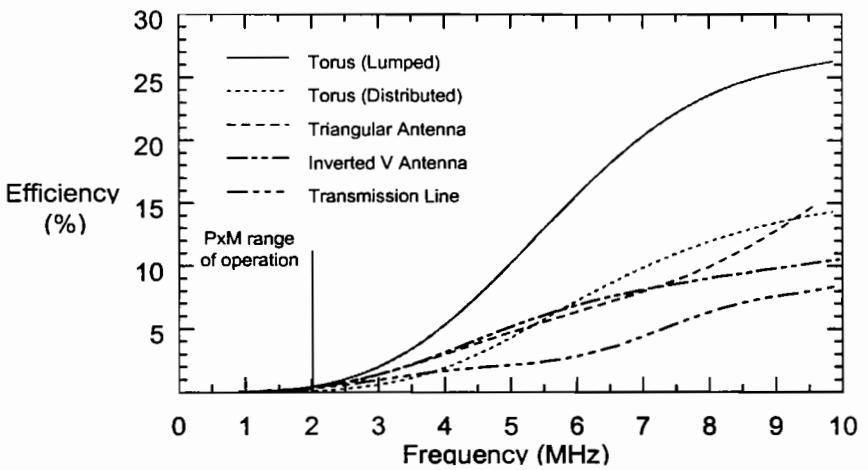


**Figure 35. Plot of the radiation efficiency of the different antennas of Table 1 as a function of frequency.**

While the radiation efficiency in Figure 35 is very small, this does not detract from the usefulness of these antennas in making measurements. The radiation efficiency is essentially a far-field observable. Even though the efficiency of the antenna may be

small, there can be large near fields, and as noted in [1], the near E and H fields can be made to appear like a plane wave — if the termination resistance $R_L$ is chosen properly.

Figure 36 presents the near field wave impedance magnitude $|Z_w| = |-E_z/H_y|$ as a function of distance from the antenna along the x-axis in the direction of the p×m field maximum (see Figure 4). In this figure, the distance is measured from the voltage source exciting the antenna. Notice that after a distance of 10 to 20 meters from the nearest end of the antenna, the near field impedance $Z_w$ is very close to the required free-space value of 377 Ω. The inverted V antenna appears to have the best impedance characteristics, with a close observer distance of several meters being possible before the impedance begins to deviate significantly. On the other hand, the toroid with the distributed impedance has the worst performance with regard to the impedance.

The achievable levels of the E-field for the various antennas is shown in Figure 37 as a function of position from the voltage source, for $f = 2$ MHz. Notice that the inverted V antenna has the lowest field strength of all of the antennas considered, thereby offsetting the advantage gained by having a relatively constant impedance close to the antenna. From this figure, we see that at a test object distance of about 10 meters, the resulting E-field strength will be on the order of 2 - 4 mV/m per volt of excitation voltage applied to the antenna structure.

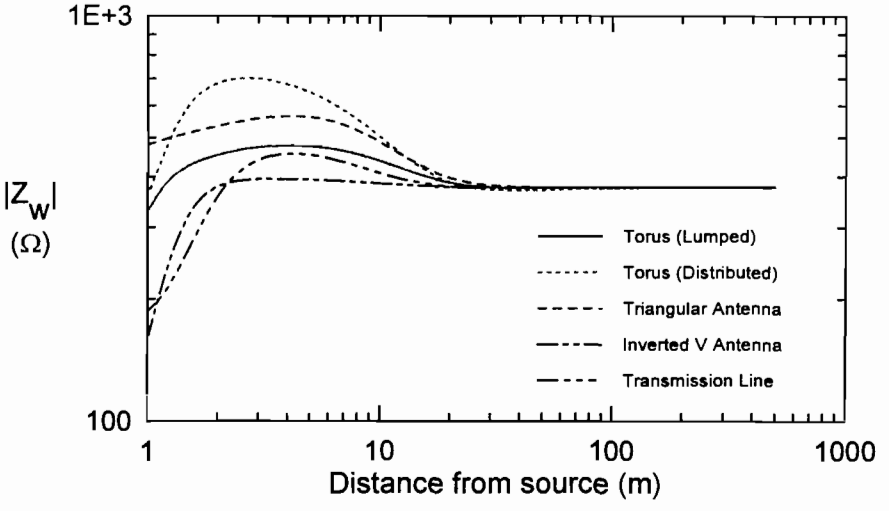


**Figure 36. Plot of the magnitude of the near field E/H ratio of the p×m antennas at $f = 2$ MHz.**

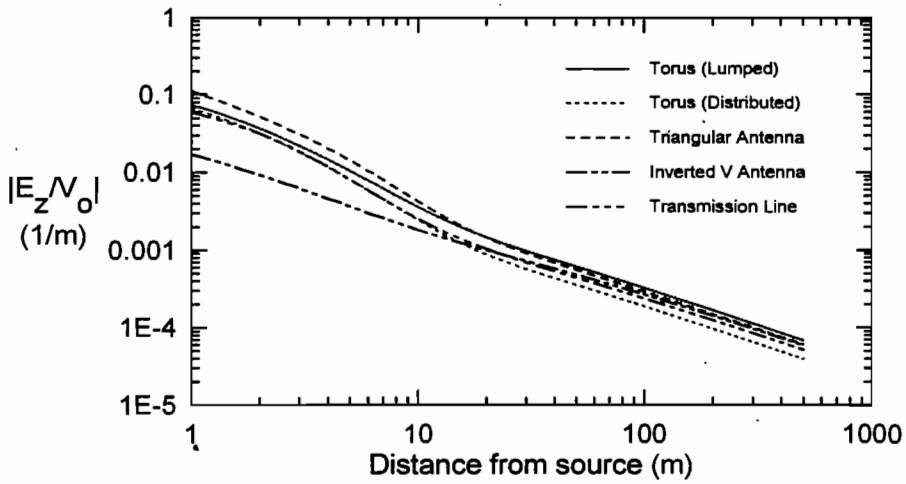


**Figure 37. Plot of the magnitude of the normalized $E_z$ field of the p×m antennas at $f = 2$ MHz.**

## 4. Effects of Antenna Shape Variation

As noted in the parametric studies of the various antennas in Section 3, the shape of the antennas has an effect on the load resistance required to maintain the proper *p/m* ratio for the antenna. Given a particular choice of the antenna shape, however, it is not evident what the best height to base ratio should be — even if the *p/m* ratio were to be correctly set. In this section, we continue with the examination of the symmetric, inverted V antenna structure shown in Figure 16 to determine the best shape for a possible experimental antenna.

### *4.1 Geometry*

For this portion of the study, the inverted V antenna is chosen with a fixed height $h = 6$ m and radius $a = 0.1$ cm. The overall base length of the antenna, $d$, is allowed to vary, from 0.1 to 100 meters, and the $E_\theta$ component of the a near-zone E-field on the ground at a location in the forward direction is computed. This observation location is chosen to be at a distance of 60 meters from the source of the antenna; hence it is described by the $x$-coordinate $x = d + 60$. The ground in this problem is assumed to be perfectly conducting.

### *4.2 Near Zone E-Field Behavior*

For this particular antenna, the curve denoted by $h = 6$ m in the middle part of Figure 18 provides the necessary load resistance as a function of the base length. Using the NEC code, several calculations were made for different base lengths, as a function of frequency. Figure 38 illustrates surface and contour plots of $|E_\theta|$ on the ground plane in the forward direction at a distance of 60 meters from the source. The thick lines in these plots denote the locus of points where $kL = \pi/2$, which roughly defines the limit of the

p×m operation of the antenna. The region of the curve to the left and below these lines is where the antenna behaves as a p×m radiator.

These data provide some interesting insight into the proper design of the p×m antenna. It is clear that for increasing the maximum operating frequency of the antenna, one should have the smallest antenna base possible. This is because antennas with an extended base dimension do not appear as a point radiator for observation locations close to the antenna: reducing the base length tends to make the antenna more compact and closer to the ideal point dipole.

Thus, the best p×m operation for this antenna occurs when the base of the antenna is less than its height. Decreasing the base too much, however, reduces the E-field strength, so a trade-off between the field strength and the highest frequency of p×m operation must be made in any realistic antenna design.

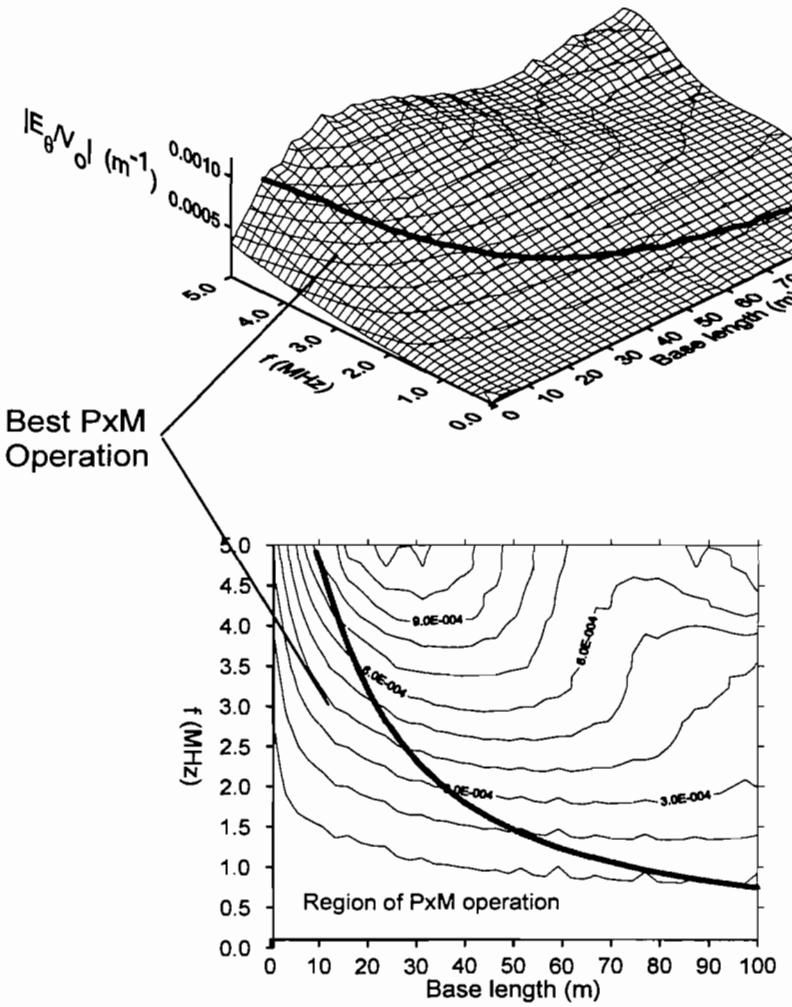


**Figure 38. Surface plot of $|E_\theta|$ on the ground plane in the forward direction at a distance of 60 meters from the source, produced by the inverted V antenna with a varying base length.**

### *4.3 Far-Field Radiation Efficiency*

In addition to the near field strength, the far-field radiation efficiency also serves to characterize the antenna. Figure 39 illustrates the calculated radiation efficiency (given in percent) for the inverted V antenna, for a limited range of base values ($d$ = .1 to 20 m) over which the antenna is best suited for p×m operation. As may be seen, the radiation efficiency is highest for the antenna with the smallest base length. This is because as the base length increases, the resistive loading on the antenna must also increase in order to maintain the proper p×m ratio. This increase resistance implies that there is a decrease in the efficiency, since more power is absorbed by the load.

However, as pointed out earlier, the idea of a p×m antenna is not necessarily to try to maximize the radiated far-field power, but to create a near field having the proper E/H ratio. Thus, while the efficiency plots Figure 39 are interesting in illustrating typical far-field behavior, the data in Figure 38 are more pertinent in designing a p×m radiating antenna.

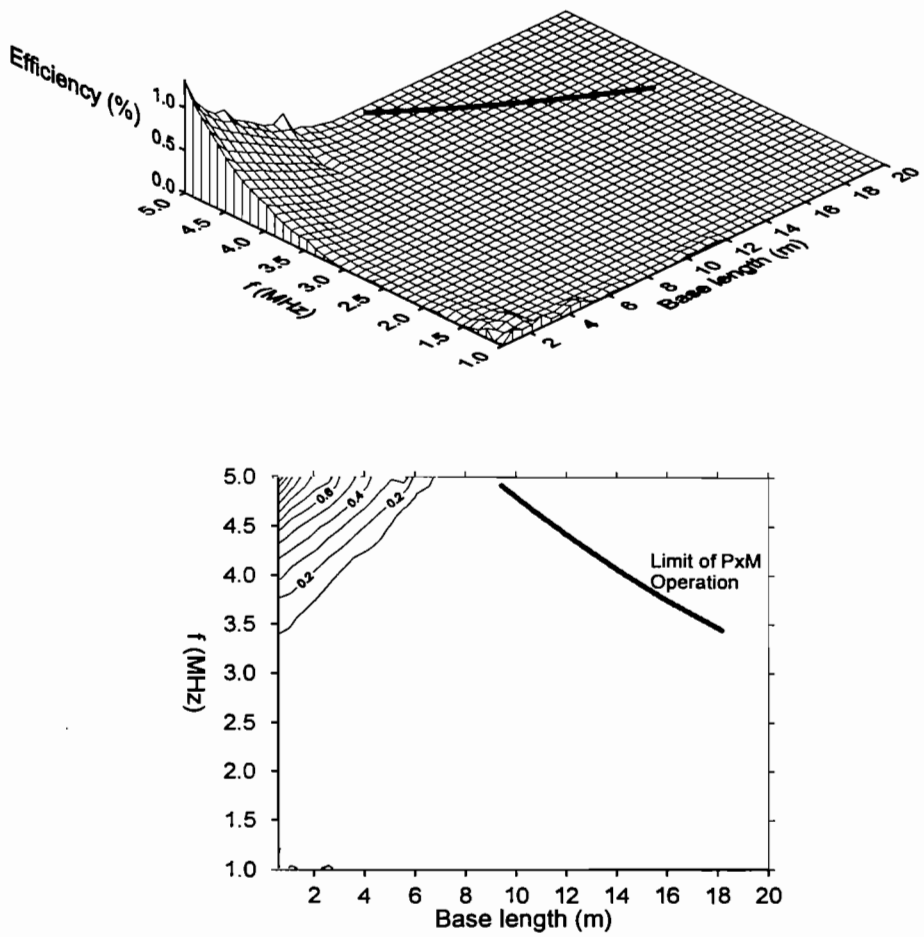


**Figure 39. Plot of the radiating efficiency of the inverted V antenna on a perfect ground plane, as a function of the frequency and the antenna base length (h = 6 m, a = 0.1 cm).**

## 5. Effects of a Lossy Earth on P×M Antenna Operation

### *5.1 Overview*

The preceding studies of the p×m antenna have assumed that the ground plane is a perfect conductor. In any realistic situation, however, the ground will be lossy, and it is well established that the radiating characteristics of an antenna located over an imperfect earth can be considerably different from those of the same antenna over a perfect ground [14]. Thus, it is expected that the lossy earth modifies the p×m antenna performance. In this section, the effects of the lossy earth on the p×m antenna behavior is examined. Only one structure, the inverted V antenna, will be considered, as it is expected that all of the other antennas will have similar responses.

For lossy earth problems, an important issue is understanding how the antenna is connected to the earth. In the case of the perfect ground, the antenna was connected to the ground plane at two different locations and the return current flowed on the ground plane. For the lossy ground case, one could think of either connecting the antenna to earthing electrodes, or providing another conductor lying on the earth's surface to make the connection. Both of these possibilities are examined in here.

### *5.2 The Grounded, Inverted V Antenna*

For this configuration of the inverted V antenna, we assume that there is a ground stake extending into the earth to a depth of $\ell = 15$ meters at each end of the antenna, as shown in Figure 40. This rather large depth is chosen in attempt provide a very low grounding impedance for the antenna, and this configuration could be realized by using multiple grounding electrodes, or perhaps by a grounding mesh[3]. The other antenna parameters chosen for this study are $d$ = 30m, $h$ = 6 m, $a$ = 0.1 cm. The ground is assumed to be modeled by a frequency-independent conductivity $\sigma$ and a relative dielectric constant $\varepsilon_r = 10$.

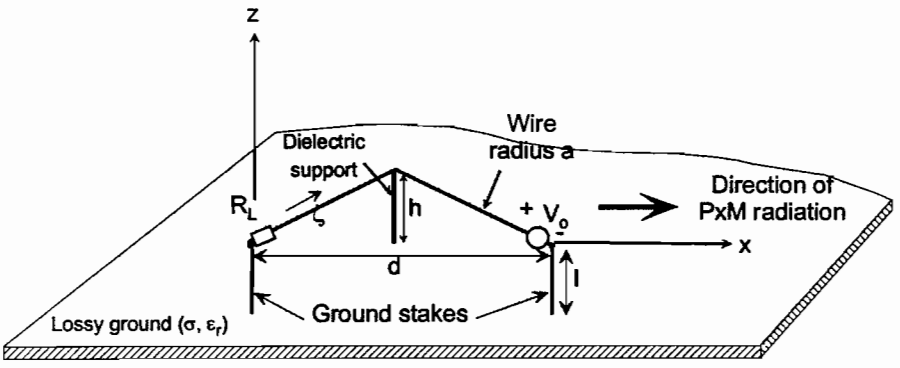


**Figure 40. The grounded, inverted V antenna in the presence of a lossy earth.**

[3] It is probable, however, that the presence of the grounding net will change the characteristics of the antenna somewhat, due to its finite size. This implies that the design of the net must be included in the design of the antenna. The presence of possible grounding electrodes will also effect the antenna design

With this geometry, the total above-ground wire length is $L$ = 32.3 m, and at an assumed operating frequency of 2 MHz, the parameter $kL$ = 1.35. From Figure 20, we see that this is about the highest frequency possible for the p×m operation of the antenna when it is located over a *perfect* ground plane.

As discussed in Section 2, if the ground plane is a perfect conductor, image theory can be used to compute the electric and magnetic dipole moments of the antenna, given the charge and current distributions on the antenna wires. Unfortunately, for a real earth such a simple image theory is not possible. With the lossy earth present, the induced charge and current in the soil are volumetric quantities and they are not easily calculated. Moreover, even if they were to be calculated, the determination of the dipole moments is a difficult task, and the selection of the antenna load resistance for optimum p×m performance is not simple. This leads to the necessity of determining the required load resistance by one of the alternate methods outlined in Section 2.

The basis for the analysis of the p×m antenna near the lossy earth is the integral equation solution for the antenna current and charge [15]. This solution involves the fundamental expressions for the general EM fields produced by an infinitesimal vertical or horizontal current element at an arbitrary height over the ground [13], [16], [17]. This modeling approach is well established, and has been implemented in the NEC code [9], which is the tool used for the present studies. As the purpose of the present report is the investigation of the behavior of specific p×m antennas, and not the fundamentals of analysis of lossy earth problems, detailed discussions of these models are not included here. The interested reader should consult the literature for additional information on the modeling of antennas over a lossy earth.

### 5.2.1 Wave Impedance in the Forward Direction for the Grounded Antenna

As it is important to adjust the load resistance to the correct value for p×m operation of the antenna, a useful calculation is to examine the wave impedance of the near-field in the forward direction, as done for the transmission line antenna in Figure 9. Figure 41 presents the surface and contour plots of the near field wave impedance magnitude of the primary $E$ and $H$ components in the forward direction at a location ($x$, $y$, $z$) = (60, 0, 0) meters for the inverted V antenna, assuming that the lossy earth has the parameters $\varepsilon_r$ = 10, $\sigma$ = 0.01 S/m. For the perfect earth, this antenna had a calculated optimum resistance value of $R_L$ = 521 Ω; however, for this particular value of earth conductivity, a much higher value of $R_L$ = 1300 Ω appears to be appropriate. (This resistance value is illustrated by the straight dashed line in the figure.) Furthermore, we note that even with this selected value of load resistance, the near-field impedance approaches several thousand ohms at a frequency of $f$ = 1.75 MHz — a marked contrast to the rather slowly varying impedance surface for the same antenna over a perfect ground, as is evident in Figure 21.

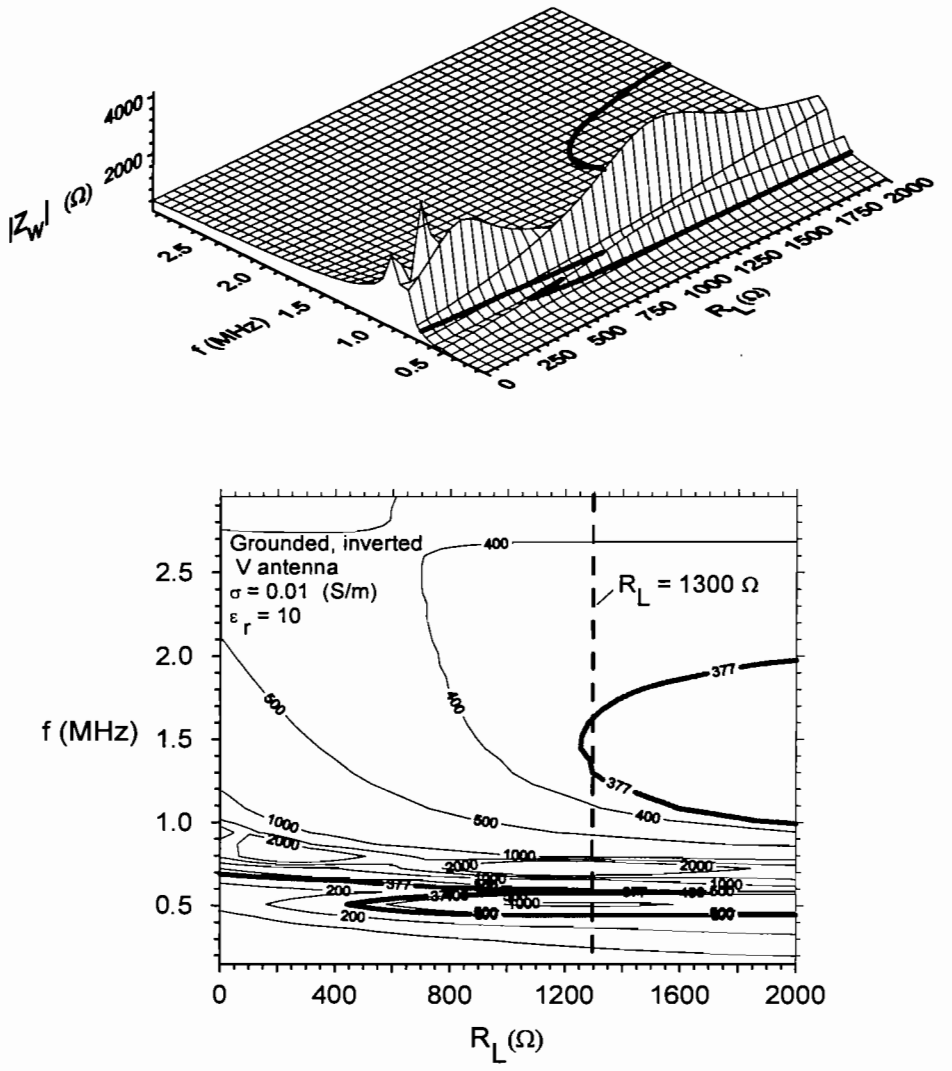


**Figure 41. Surface and contour plots of the wave impedance magnitude $|Z_W|$ in the forward direction at a location $(x, y, z) = (60, 0, 0)$ m for the grounded, inverted V antenna over a conducting earth of parameters $\varepsilon_r = 10$, $\sigma = 0.01$ S/m.**

### 5.2.2 Far Field Radiation Patterns

Using the NEC code, the far-zone radiation field from the grounded inverted V antenna can be calculated, taking into account the lossy ground effects. For this calculation, the coordinate system shown in Figure 42 is used.

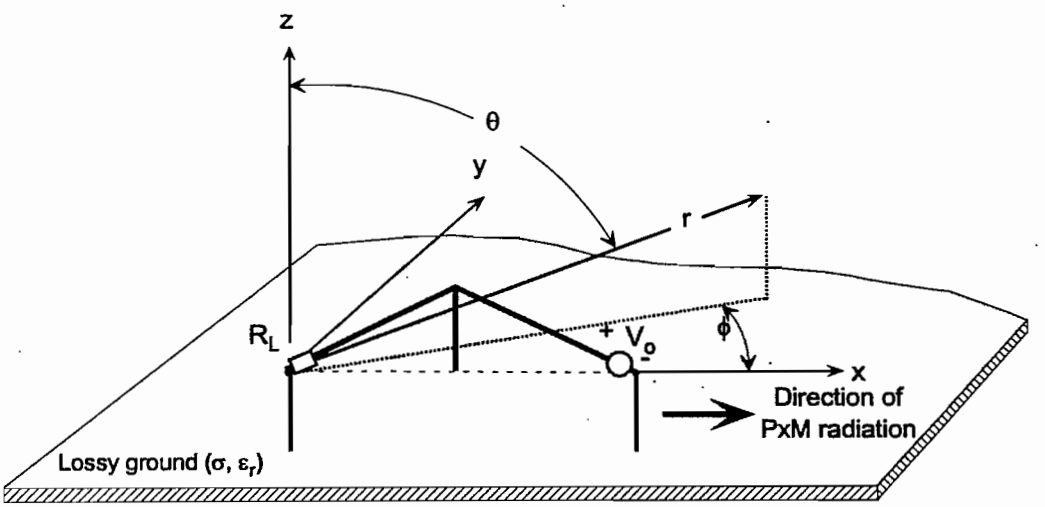


**Figure 42. Coordinate system for computing the EM fields produced by the V antenna.**

In Section 3.3 the optimum load resistance for the V antenna over a perfect earth was determined to be $R_L$ = 521 Ω. Using this value, the left-hand figures of Figure 43 show the magnitudes of the far-field $E_\theta$ component radiated by the inverted V antenna over a perfect earth at $f$ = 2 MHz. Similarly, the right-hand figures show the radiation pattern for the antenna over the lossy earth with a conductivity $\sigma$ = 0.01 S/m and relative dielectric constant $\varepsilon_r$ = 10. The antenna resistance for this latter case was the estimated value of $R_L$ = 1300 Ω. Part *a* of this figure presents a perspective view of the radiation pattern, taken with look angles of $\theta$ = 75° and $\phi$ = -75°. Part *b* of the figure illustrates a back-side view of the radiation pattern from the antenna, view with look angles of $\theta$ = 90° and $\phi$ = 180°. This shows how the backward null in the field moves to either side as the conductivity decreases. Part *c* presents the same radiation pattern from a side view with look angles of $\theta$ = 90° and $\phi$ = -90°. In these latter plots it is evident that the $E_\theta$ field on the surface of the earth is significantly reduced in the presence of the lossy earth.

Notice that for the perfectly conducting earth, an observer on the ground sees a large $E_\theta$ field in the +$x$ direction (the direction of the maximum p×m radiation), and the expected null in the field in the -$x$ direction. For the imperfect earth, however, we note that the $E_\theta$ field on the earth surface becomes quite small and the overall shape of the radiation pattern is distorted. Moreover, the null in the backward direction moves laterally off to the side of the radiation pattern (i.e., nulls move to the ± $y$ directions in the pattern.)

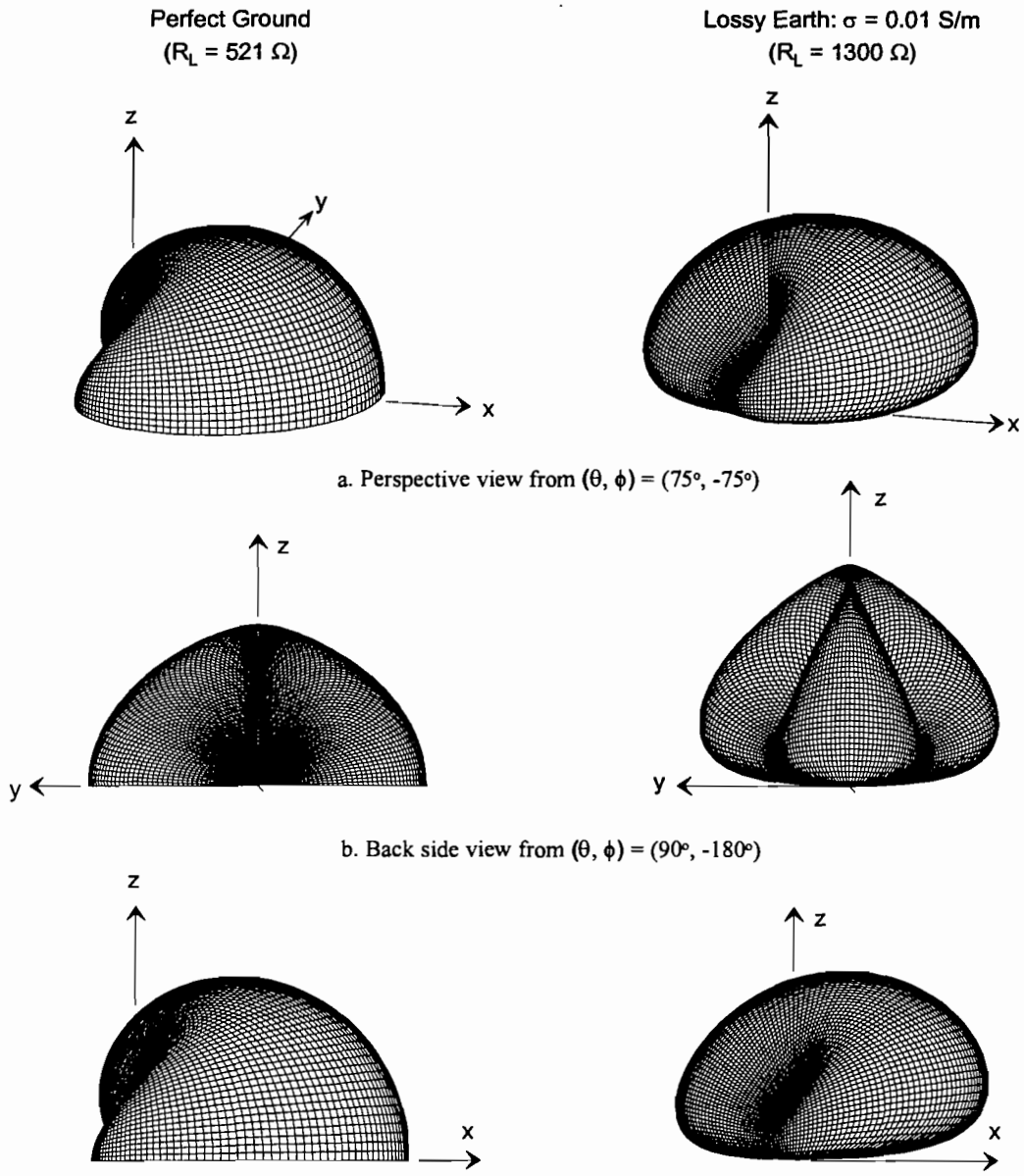


**Figure 43. Spatial plots of the far-field $E_\theta$ component radiated by the grounded, inverted V antenna for different earth conductivities at a frequency of $f$ = 2 MHz.**

### 5.2.3 Near-Zone E--Field

It is clear from the far-field patterns that the p×m antenna is not very useful for producing vertical E-fields on the earth's surface. As noted earlier, the radiation efficiency of the antenna is low, and the main benefit of this type of antenna is to be able to locate the antenna close to an object under test to increase the field strength while maintaining a proper E/H ratio. Thus, a study of the *near field* behavior of the antenna is desirable.

Considering a nominal radial distance of $r$ = 100 m, Figure 44 presents spatial plots of the near-zone $E_\theta$ for different earth conductivities. Notice that the null in the field still moves about as the conductivity changes, but the $E_\theta$ field on the earth surface now has a non-zero value, indicating that a ground-based system located along the $+x$ axis would receive useful vertical E-field excitation.

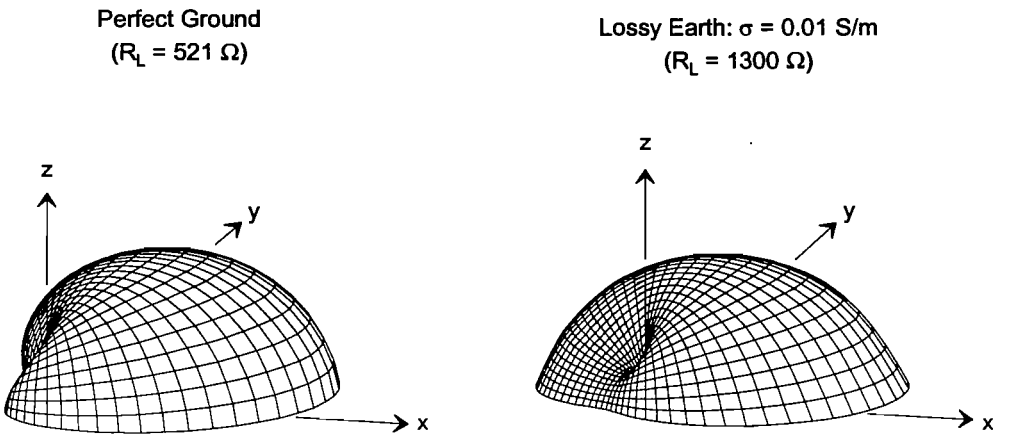


**Figure 44. Spatial plots of the near field $E_\theta$ magnitude produced by the grounded, inverted V antenna at a distance of r = 100 m for different earth conductivities for a frequency of $f$ = 2 MHz.**

It is instructional to plot the behavior of the normalized $E_\theta$ field magnitude in the primary vertical plane (the x-z plane) as a function of the angle $\theta$. This is illustrated in Figure 45, where the negative $\theta$ angles correspond to the "back" side of the antenna, (where $\phi = 180°$) and the positive $\theta$ angles correspond to $\phi = 0°$ (the "front" side). This plot clearly shows that for the perfectly conducting ground, the near field $E_\theta$ magnitude is very small in the backward direction. However, as the earth conductivity decreases, this backward field increases as the antenna becomes non-ideal in its p×m characteristics.

As suggested in Section 2.3, the optimum value of the load resistance for the antenna over the lossy earth can be estimated by trying to minimizing the $E_\theta$ field in the backward direction ($\theta = 90°$ and $\phi = 180°$). Note that at this location, $E_\theta = -E_z$, which is the vertical E-field at the earth surface. Due to the overall complexity of the analysis, a direct analytical solution to this minimization problem is not possible, and numerical results again must be used. One way of doing this is illustrated in Figure 46 where surface and contour plots of the normalized field $E_\theta / V_0$ are shown as a function of both the load resistance $R_L$ and the ground conductivity $\sigma$. In these calculations, the load resistance varied from 1 to 10,000 Ω, and the conductivity varied from 0.001 to 1.0 S/m. Due to these rather large ranges, the logarithm of these variables is used in the plotting on the $x$ and $y$ axes of the plot.

In this figure, the locus of points corresponding to a minimum in the vertical field is shown by the heavy dark line. Notice that for a large conductivity of $\sigma$ = 1.0 S/m, the

load resistance is approximately $R_L \approx 501\ \Omega$ (or $\log R_L \approx 2.7$), which is close to the perfect earth case of 521 Ω. For the case of an earth conductivity of 0.01 S/m, the required load resistance is on the order of 1000 Ω, which is comparable to the value of $R_L \approx 1300\ \Omega$ (or $\log R_L \approx 3.1$), estimated from Figure 41.

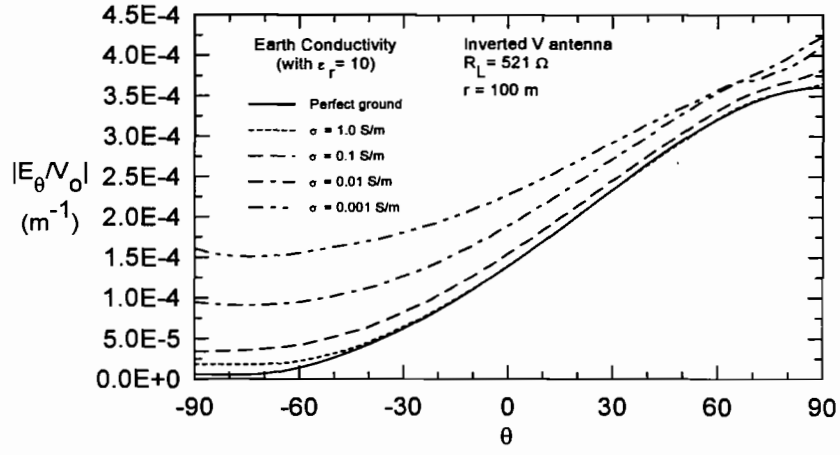


**Figure 45. Plot of the $E_\theta$ near field magnitude in the $\phi = 0°$ plane at a distance of $r = 100$ m for the grounded, inverted V antenna with different earth conductivities for a frequency of $f = 2$ MHz. (Assuming a constant load resistance of 521 Ω.)**

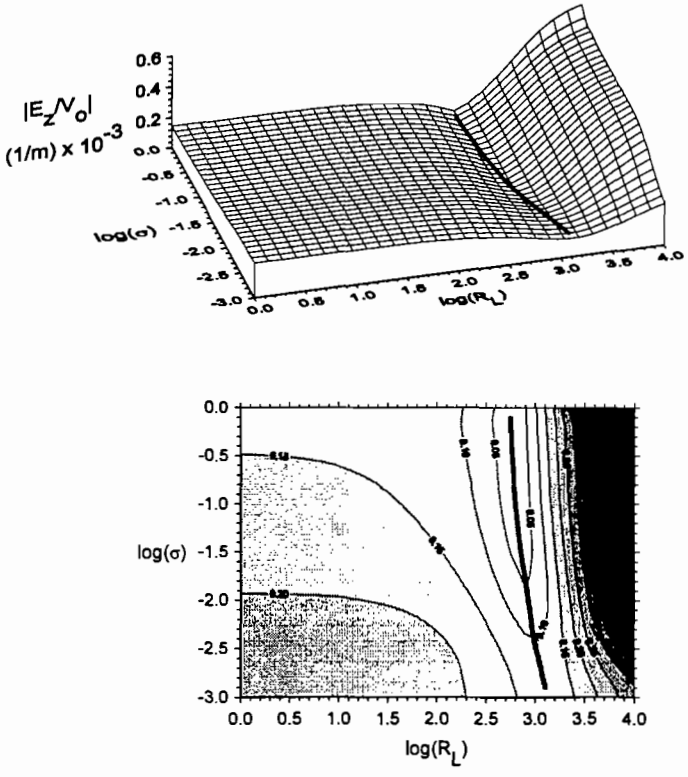


**Figure 46. Plot of the vertical $E$ field magnitude on the ground at $r = 100$ m in the backward direction ($\phi = 180°$) for the grounded, inverted V antenna for different earth conductivities and loading resistances for a frequency of $f = 2$ MHz.**

### *5.3 The Ungrounded Inverted V Antenna with a Return Wire*

The behavior of the grounded V antenna in the previous section is not particularly good if the earth is lossy. Both the electric and magnetic dipole moments are affected by the lossy earth, and at DC, the ratio between these two parameters depends on the ground properties. As the ground conductivity becomes extremely low, the return current path passing through the earth sees a high resistance, and this limits the magnetic dipole moment of the antenna. A possible solution to this difficulty is to use a return wire lying on the earth's surface to maintain a low resistance DC current path, as illustrated in Figure 47. In this model, it is assumed that there are no direct electrical connections between the antenna and the lossy earth.

For this antenna, the same parameters used for the grounded antenna are considered: $d$ = 30m, $h$ = 6 m, $a$ = 0.1 cm, and the $\varepsilon_r$ = 10.

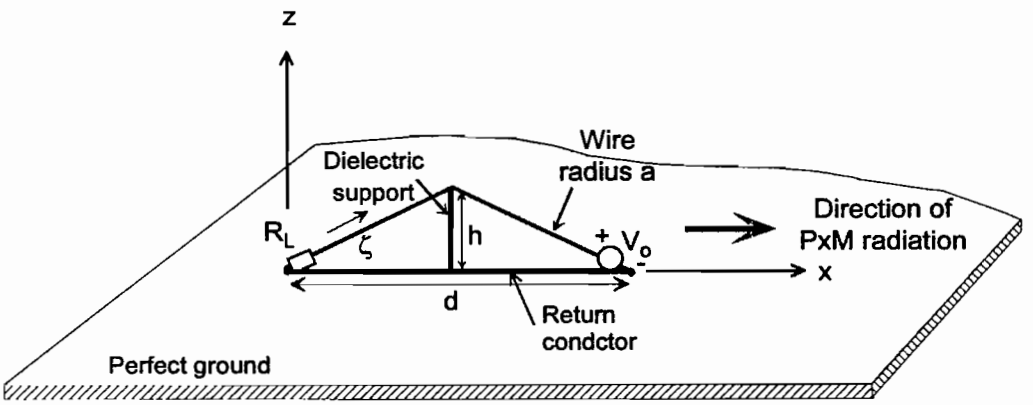


**Figure 47. The ungrounded, inverted V antenna with a return conductor, in the presence of a lossy earth.**

#### 5.3.1 Wave Impedance in the Forward Direction for the Antenna with Return Conductor

In an attempt to adjust the load resistance for p×m operation for this antenna, Figure 48 presents the wave impedance of the near-field in the forward direction, as was done in Figure 41. As before, the field observation location was at ($x$, $y$, $z$) = (60, 0, 0) meters and the earth has the parameters $\varepsilon_r$ = 10, $\sigma$ = 0.01 S/m. For the lossy earth, the variation of the wave impedance is much less than for the grounded V antenna, indicating that this ungrounded configuration of antenna may be more desirable. From the data in Figure 48, it is evident that an antenna resistance of $R_L$ = 1100 Ω is appropriate for the load.

It is also interesting to examine the behavior of the phase of the wave impedance for this antenna. Figure 49 illustrates the behavior of the phase for this case and it may be compare it with the phase of the same antenna over the perfectly conducting ground in Figure 22. It is evident that for frequencies below about 1 MHz, there are some rapid variations in the phase.

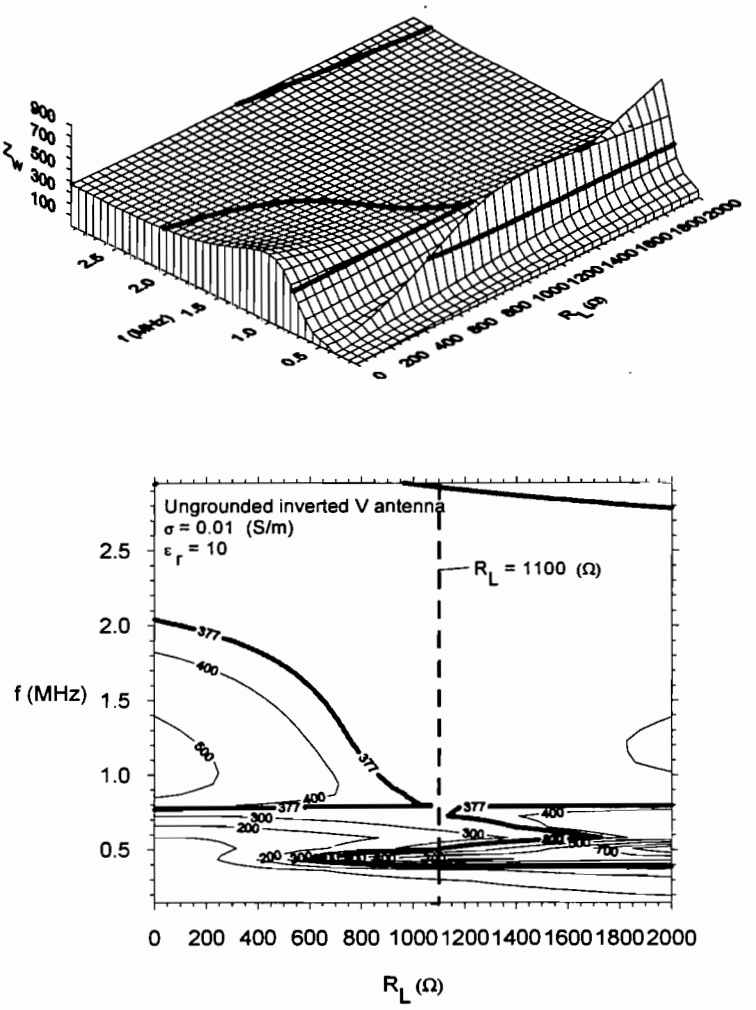


**Figure 48. Surface and contour plots of the wave impedance magnitude $|Z_W|$ in the forward direction at a location $(x, y, z) = (60, 0, 0)$ m for the ungrounded, inverted V antenna with a return conductor over a conducting earth of parameters $\varepsilon_r = 10$, $\sigma = 0.01$ S/m.**

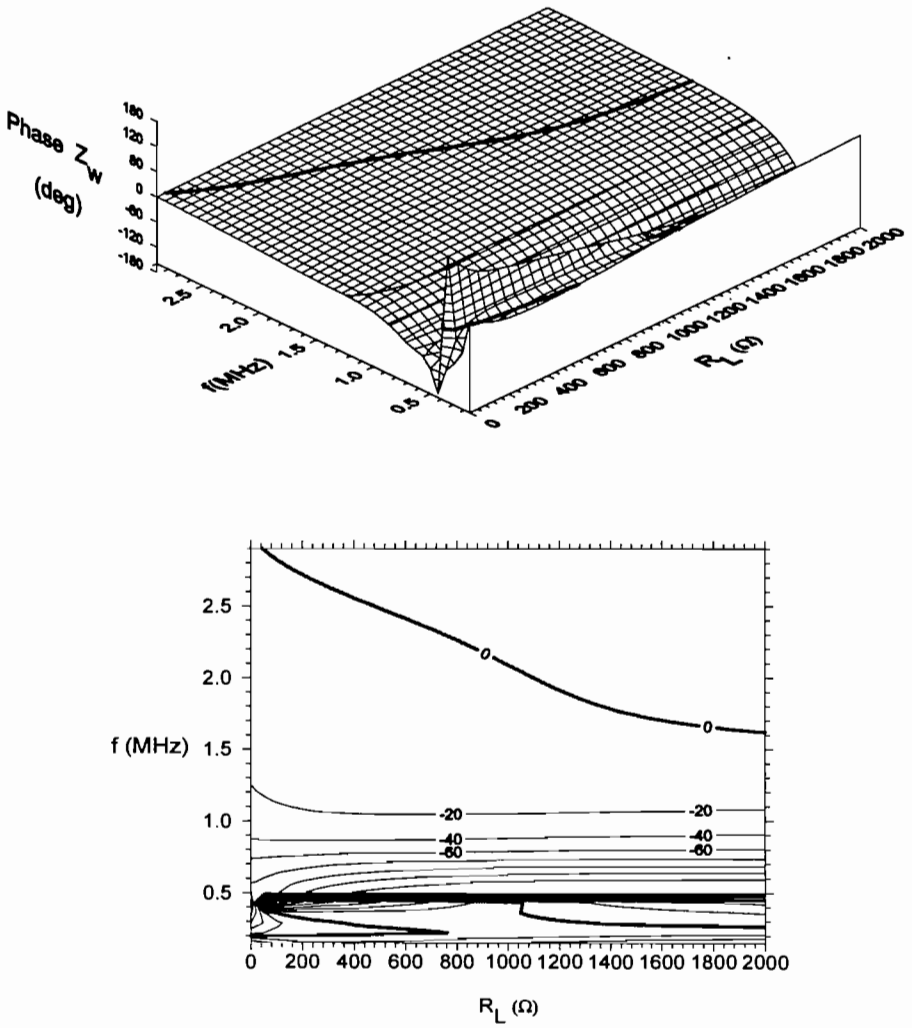


**Figure 49. Surface and contour plots of the wave impedance phase in the forward direction at a location ($x$, $y$, $z$) = (60, 0, 0) m for the ungrounded, inverted V antenna with a return conductor over a conducting earth of parameters $\varepsilon_r = 10$, $\sigma = 0.01$ S/m.**

### 5.3.2 Far Field Radiation Patterns

Using the same coordinate system shown in Figure 42, radiation patterns from the ungrounded inverted V antenna at $f = 2$ MHz have been calculated and are presented in Figure 50. The left-hand figures show far-field $E_\theta$ components for a perfect earth (the same data as in Figure 43), and the right-hand figures illustrate the corresponding patterns for the antenna over the lossy earth ($\sigma = 0.01$ S/m and $\varepsilon_r = 10$). The antenna resistance for this latter case was that shown in Figure 48 ($R_L = 1100\ \Omega$).

In these plots, it is evident that although the earth still modifies the shape of the radiation pattern, the null in the E-field in the backward direction is maintained and does

not approach the side of the antenna, as observed in Figure 43 for the grounded antenna. Thus, this antenna configuration provides a field more like that desired for the p×m antenna over a perfect ground. Similar radiation patterns were noted for other earth conductivities.

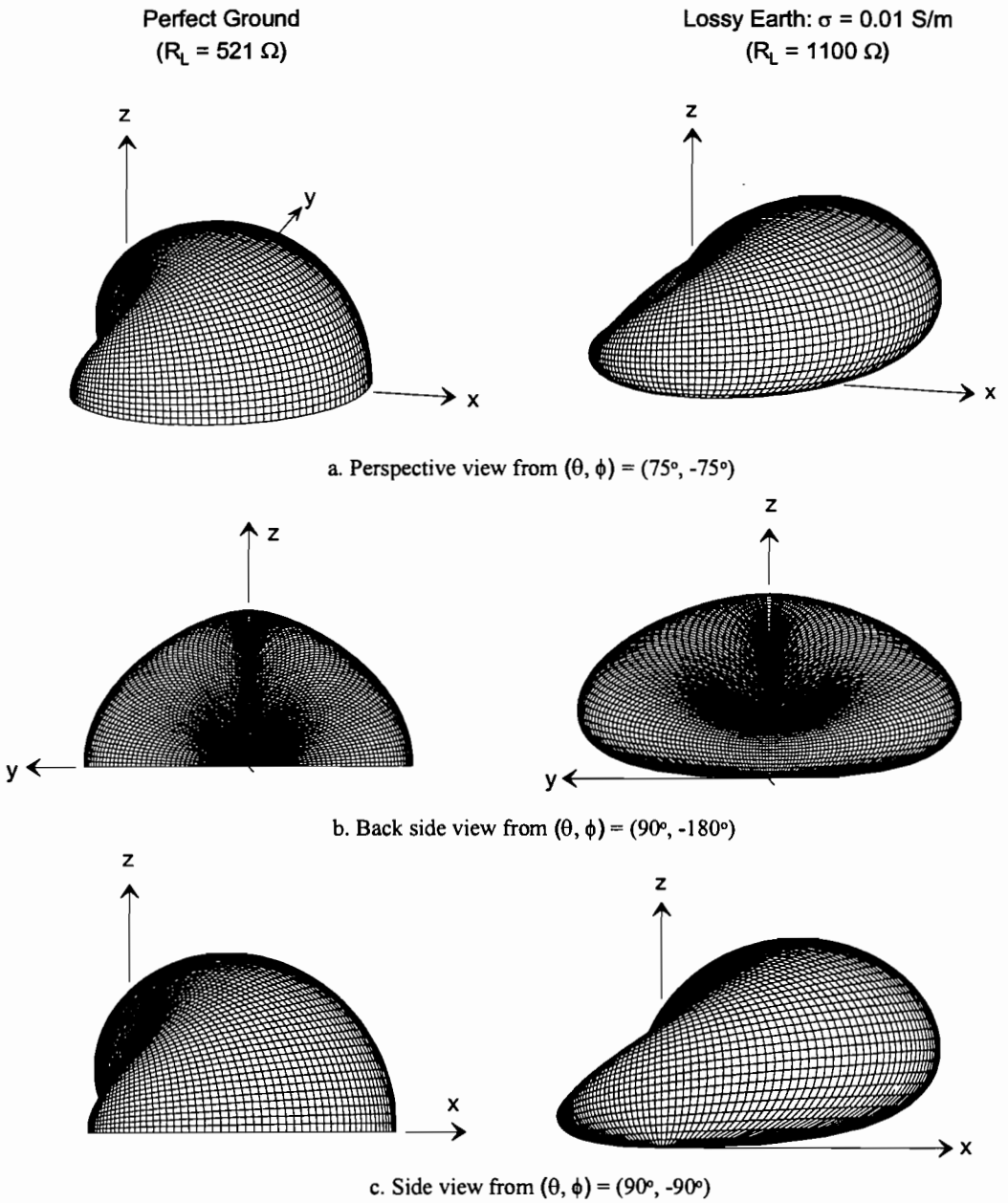


**Figure 50. Spatial plots of the far-field $E_\theta$ component radiated by the ungrounded, inverted V antenna for different earth conductivities at a frequency of $f$ = 2 MHz.**

### 5.3.3 Near-Zone E-Field

Figure 51 presents the magnitude of the near-zone $E_\theta$ field magnitude at a radial distance of $r$ = 100 m from the coordinate origin, both for the perfect ground and for the lossy earth. In this case, the overall p×m antenna field shape still remains for the lossy earth case, although the null in the field in the backward direction is not as strong as for the perfectly conducting earth.

Figure 52 presents plots of the $E_\theta$ near field magnitude in the $\phi = 0°$ plane at a distance of $r$ = 100 m for the ungrounded, inverted V antenna with different earth conductivities for a frequency of $f$ = 2 MHz. As before, this assumes a constant load resistance of 521 Ω, which is the correct impedance for the perfectly conducting earth. As a consequence, this particular value of resistance may not be correct for other earth conductivities.

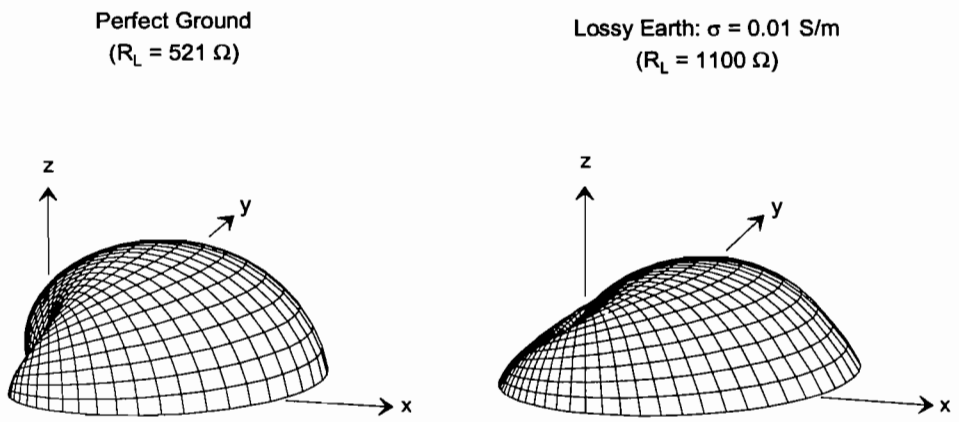


**Figure 51. Spatial plots of the near field $E_\theta$ magnitude produced by the ungrounded, inverted V antenna at a distance of r = 100 m for different earth conductivities for a frequency of $f$ = 2 MHz.**

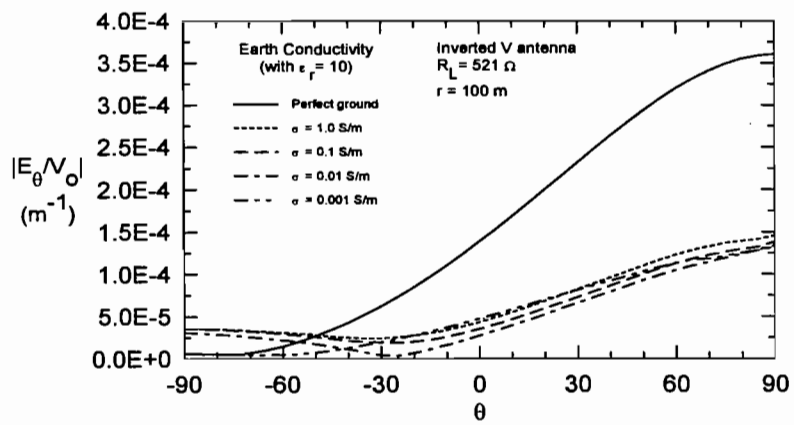


**Figure 52. Plot of the $E_\theta$ near field magnitude in the $\phi = 0°$ plane at a distance of $r$ = 100 m for the ungrounded, inverted V antenna with different earth conductivities for a frequency of $f$ = 2 MHz. (Assuming a constant load resistance of 521 Ω.)**

Finally, estimates of the proper load resistance for this antenna are provided by the data in Figure 53, which shows the normalized vertical E-field in the backward direction for the ungrounded, inverted V antenna over the lossy earth. This figure was computed at a frequency of $f$ = 2 MHz and at a distance of $r$ = 100 meters from the antenna origin.

For a ground conductivity of 0.01 S/m, Figure 53 estimates a load resistance of $R_L$ ≈ 630 Ω, which is significantly lower than the 1100 Ω value estimated in Figure 48. This discrepancy between the two values of optimum load resistance points to the rather complex nature of the lossy earth and its influence on antenna behavior. Clearly, it is not easy to obtain optimum p×m antenna operation in a real earth environment.

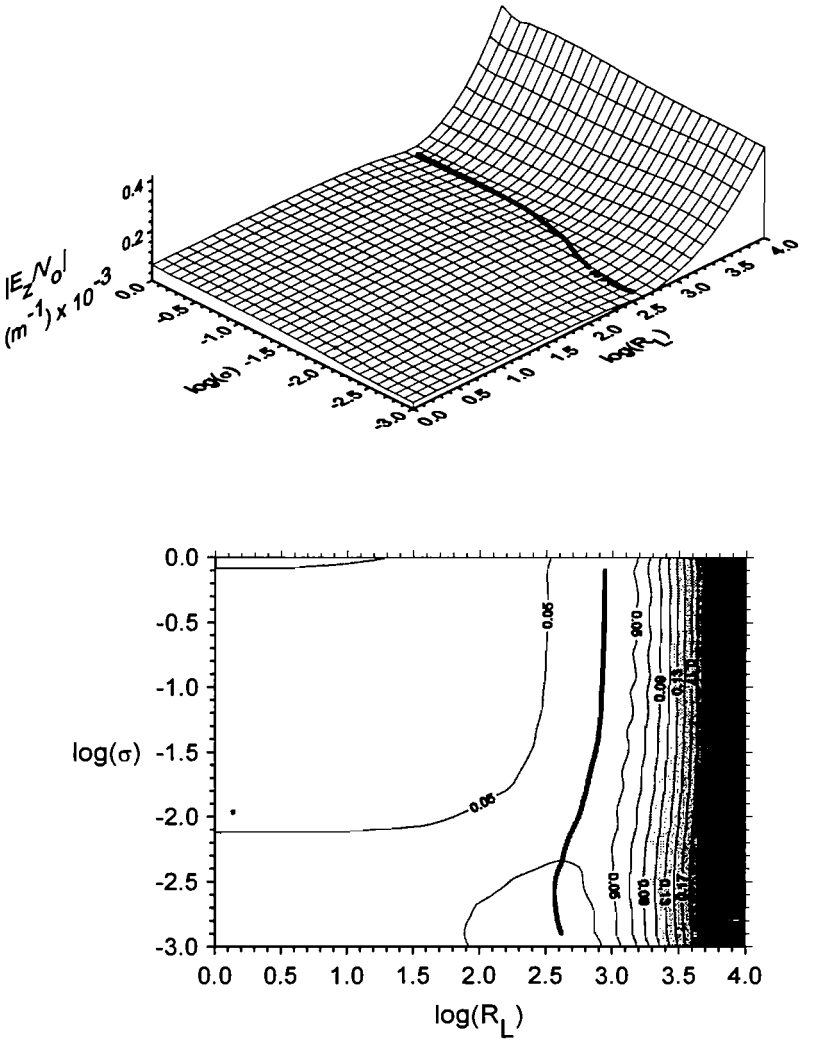


**Figure 53. Plot of the vertical $E$ field magnitude on the ground at $r$ = 100 m in the backward direction ($\phi$ = 180°) for the ungrounded, inverted V antenna for different earth conductivities and loading resistances for a frequency of $f$ = 2 MHz.**

## 6. P×M Antenna Measurements

### *6.1 Overview*

The theoretical studies of the P×M antenna in this note and in its predecessor [1], have explored various aspects of the antenna design and operation, including the optimum antenna loading for p×m operation, the antenna efficiency, near-field impedance behavior, the EM field signal strength in the near zone, and the effects of a lossy earth on the antenna operation.

To further the understanding of this type of antenna, a test program was developed and various p×m antenna responses were measured. These measurements permit a comparison of the actual antenna responses with the theoretical models and lead to a better understanding of the p×m antenna. In this section, the experiments on this antenna are discussed and results are summarized. In all cases, the experimental results are compared with computed responses.

### *6.2 Antenna Configurations*

While several different antenna configurations have been analyzed in the previous sections of the report, we have examined experimentally only one: the inverted V antenna. The theoretical investigations have shown that the other antennas — the transmission line antenna, the triangular antenna and the half-loop structure — all have responses that are similar to the inverted V structure. Thus, we believe that measured responses from this antenna will be representative of the other p×m antennas.

Based on the information presented in Figure 35, the best configuration for the inverted V antenna is one having a large height to base ratio, together with a return conductor, as suggested in Figure 54. For the measurement program, two different cases were considered: a large p×m antenna located over a real (lossy) earth, and a small-scale version of the same antenna, which was located over a highly conducting ground plane.

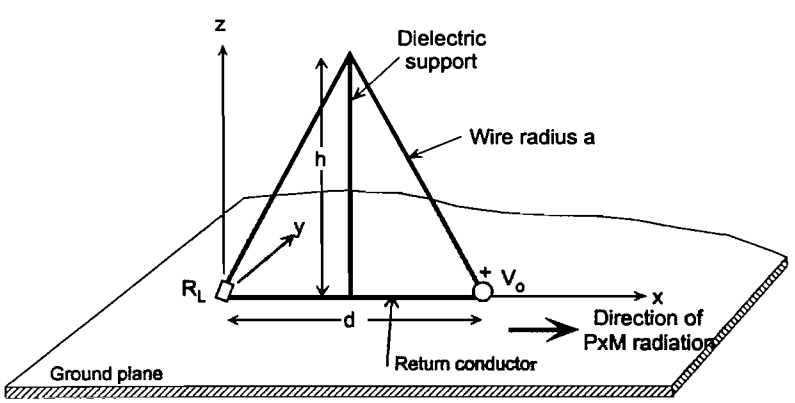


**Figure 54. Shape of the inverted V antenna used in the measurements.**

### 6.2.1 The Large P×M Antenna

Figure 55 illustrates the large p×m antenna in place for the experimental program. For this antenna a dielectric mast (actually a long fishing pole) of height $h = 4.5$ meters was used to support the antenna wires, which had a radius of $a = 0.4$ mm. The base length of the antenna ($d = 5.20$) m was chosen to form an equilateral triangle. As this antenna must be electrically small for p×m operation, the total wire length $L =$ 15.6 m dictates the highest operating frequency at which the antenna will function properly, which is approximately 5.6 MHz.

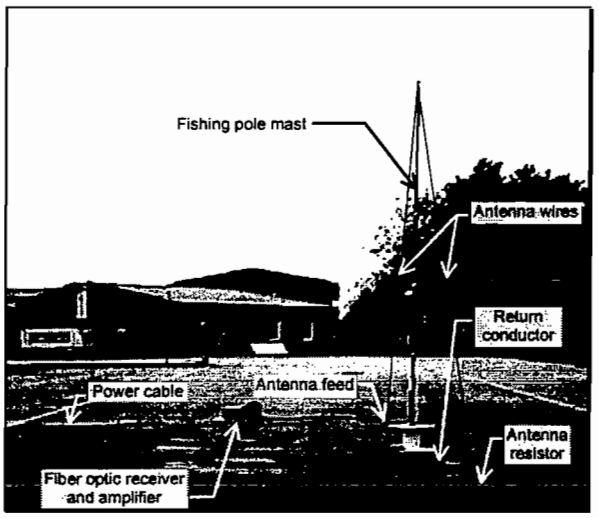


**Figure 55. The large p×m antenna over an imperfectly conducting ground, supported by a non-conducting mast.**

This antenna was located on an empty parking lot covered with asphalt. Consequently, the effective ground conductivity and relative permeability are unknown. In an attempt to minimize the effects of the earth conductivity on the low-frequency antenna operation, a return wire connection between the two ends of the antenna wires was made at its base. As discussed in Section5.3, this connection completes the DC circuit between the source and load impedance without requiring current to flow in the ground. This makes the p×m condition for the antenna less dependent on the local ground properties. This antenna was not connected to the earth directly.

For this measurement setup, the distances to nearby above ground scattering objects were large enough to allow for estimations of errors in the measurements due to reflections. At the source end of the antenna, the amplified output of a network analyzer was fed to the antenna. As shown in Figure 56, the network analyzer output was sent via a fiber optic cable to a fiber optic receiver, and then into an RF power amplifier. Details of the antenna feed point are shown in Figure 57, where a coaxial cable from the amplifier is shown connected directly to the wires of the antenna.

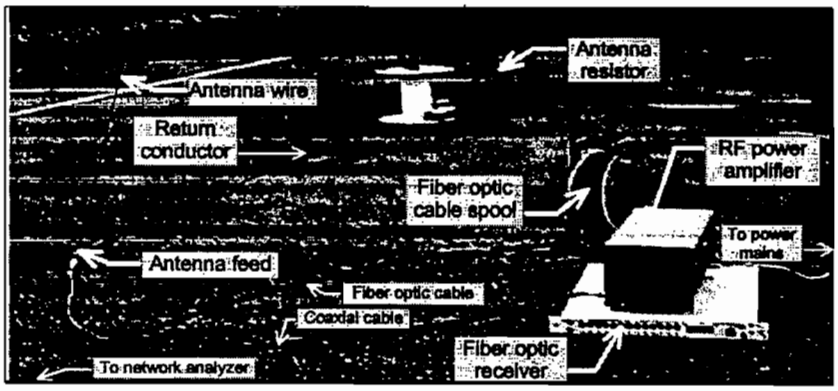


**Figure 56. Configuration of the equipment feeding the large p×m antenna.**

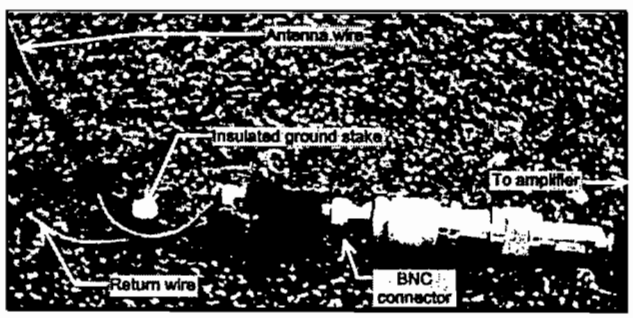


**Figure 57. Details of the feed point for the large p×m antenna.**

At the opposite (load) end, various resistors with different values were used during the experiment.

Figure 58 shows a close-up view of the load connections, in which two alligator clips were connected to the antenna wires and used to connect to resistors of various values. Due to the large power consumption in these load resistors, their values were checked periodically during the testing to insure that their values did not drift due to thermal damage.

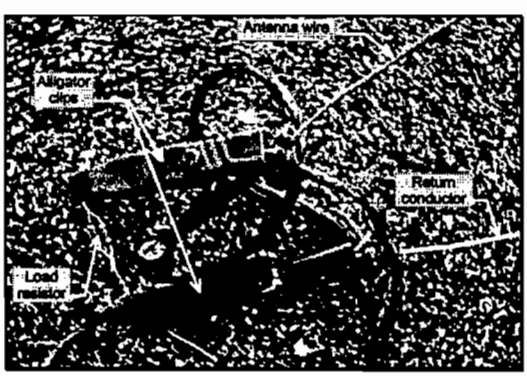


**Figure 58. Details of the resistive load for the large p×m antenna.**

### 6.2.2 Scale Model Antenna

In order to validate the theoretical results, the 1:10 scale model of the antenna located over a metallic ground plane was also considered. This antenna is shown in the photo in Figure 59. By considering this special case, we remove a number of uncertainties found in the full size model due to the lossy ground. However, such a scale model will be more critically dependent on the smoothness and the continuity of the ground plane.


**Figure 59. The scale model p×m antenna located on a conducting ground plane.**

This smaller antenna was supported by a dielectric post of height $h$ = 45 cm, which was fastened to an aluminum plate. The base dimension was $d$ = 52 cm and the total antenna wire length was $L$ = 156 cm long wire. Deviating slightly from the 1:10 scaling factor, the wire radius in this case was $a$ = 0.3 mm. For this antenna, the upper frequency limit for p×m operation is approximately 56 MHz.

The measurement site for the scale model antenna is shown in Figure 60. At the source end of the antenna, the same connection to the transmitter used for the larger antenna was employed. At the load end, a resistor fixture was used which permitted the easy replacement of the various resistors used in the measurements. This antenna model was placed over a kyckling wire mesh, which was rolled out on top of the asphalt surface. The size of the ground plane was 11 x 5 meters. Although the environmental condition was very wet due to persistent raining during the testing, the edges of the ground net were not perfectly connected to the earth. As in the large antenna measurements, fiber optics systems were used to connect the network analyzer with the power amplifier and to send the measured field results back to the network analyzer for processing.

In this photo, the probe is shown to be located at test point 3, which is located 2.5 meters from the antenna in the $x$-direction. The locations of this and the other test points will be discussed later in Section 6.2.4.

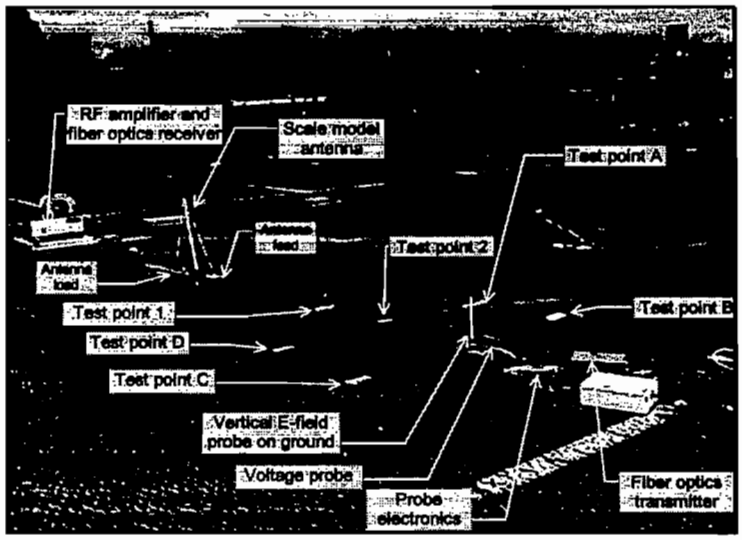


**Figure 60. Experimental setup of the scale model antenna and the E-field probe.**

### 6.2.3 Measurement Equipment Configuration

Figure 61 illustrates the measurement equipment configuration used for the experiments. The heart of the system is a HP 9195A network analyzer, which was controlled by a computer. The output signal from the network analyzer was divided by a signal splitter, and half was fed into the 50 Ω reference input of the analyzer and the other half went to a Nanofast OP 300 fiber optic transmitter, where it was sent to the equipment near the antenna input by a fiber optic cable.

The signal from the network analyzer via the fiber optic cable was received, and fed into an Amplifier Research 15A250 15 watt RF power amplifier which excited the p×m antenna input. Details of these connections are shown in Figure 56 and Figure 60

The measured E or H-field responses were also sent back to the network analyzer by a fiber optic transmission system, as indicated in Figure 61. Details of field sensors used in these measurements are presented in Section 6.3.

Note that this measurement configuration permits not only the magnitudes of the E and H fields, but also the phase. Thus, it is possible to obtain a knowledge of both the magnitude and phase of the near-field wave impedance of the antenna.

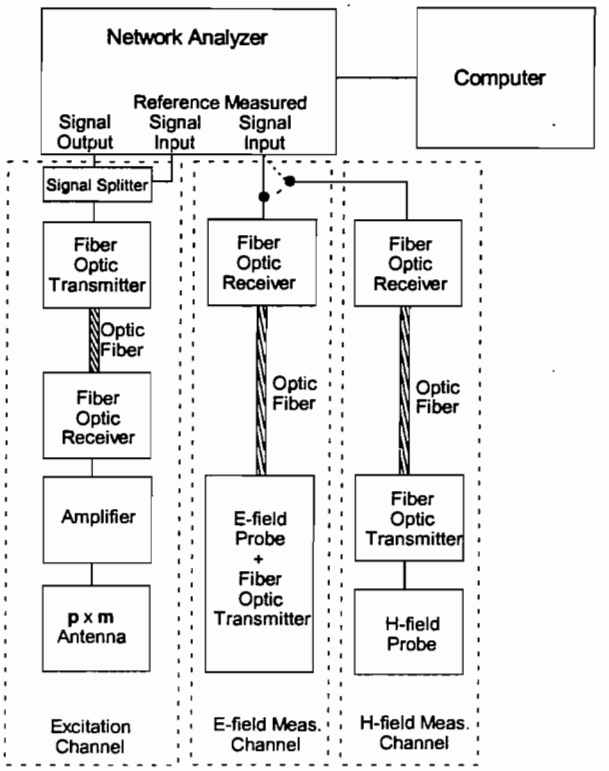


**Figure 61. Measurement equipment configuration for p×m antenna testing.**

### 6.2.4 Test Point Locations

For the measurements, a number of test point locations were defined at which the E-fields or H-fields were measured. The definition of these test points uses the coordinate system shown in Figure 54. Test points 1 through 9 were located along the $x$-axis in the positive direction, as shown in Figure 62. In addition, test points A, B, C, and D were located off of the positive $x$-axis in an attempt to study the lateral variation in the fields. Test point R was located in the backward direction of the antenna. Some of these test points are seen in the photo of the scale model antenna in Figure 60.

Table 2 presents the $x$ and $y$ coordinates of these test points, assuming that the $x$ = 0 coordinate center is located at the antenna load position, as noted in the figure. The dimensions shown in this table and in Figure 62 are for the large antenna. For the scale model antenna, the same test point configuration is used, with the dimensions reduced by a factor of 10. During the course of the measurements, different field sensor heights $z$ were used and these values are noted, as appropriate.

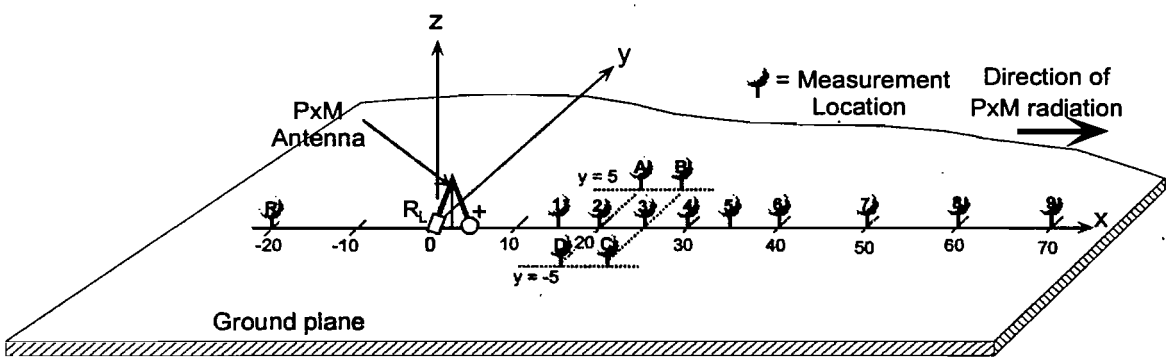


**Figure 62. Test point locations for the p×m antenna measurements. (For the 1:10 scale model antenna, divide all dimensions shown by 10.)**

**Table 2. Coordinates of the measurement point locations‡**

| Measurement point | x-coordinate† (m) | y-coordinate (m) |
|---|---|---|
| 1 | 15 | 0 |
| 2 | 20 | 0 |
| 3 | 25 | 0 |
| 4 | 30 | 0 |
| 5 | 35 | 0 |
| 6 | 40 | 0 |
| 7 | 50 | 0 |
| 8 | 60 | 0 |
| 9 | 70 | 0 |
| A | 20 | 5 |
| B | 25 | 5 |
| C | 25 | -5 |
| D | 20 | -5 |
| R | -20 | 0 |

† The x-coordinate is measured from the antenna source location.

‡ Divide all values by 10 for the scale model antenna.

## 6.3 *Sensors for Measuring the Electric and Magnetic Field*

### 6.3.1 E-field probes

An active spherical probe (Nanofast 709-2) without conductive connections was used to measure the electric field strength. This probe is illustrated in Figure 63. All electronic circuits and the fiber optic transmitter are contained in the sphere, and the measured signal was transmitted by a fiber optic link to the network analyzer. This minimizes the unwanted cable interactions and gives good accuracy in the measured values.

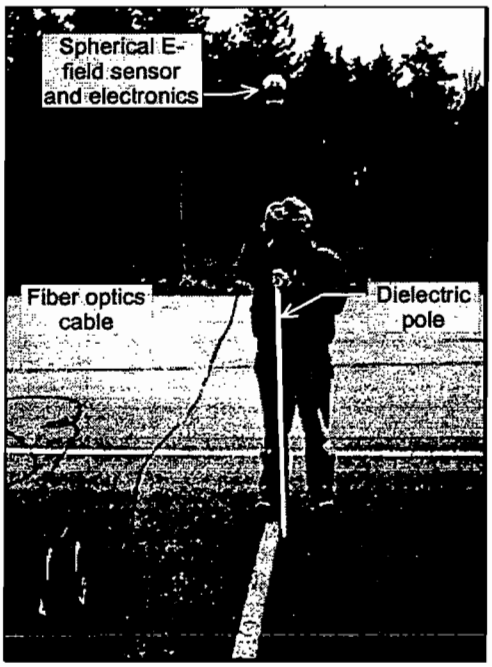


**Figure 63. The spherical E-field sensor, shown at a measurement height of 2.5 m over the ground.**

This spherical probe cannot be used close to the ground, however. Consequently, for such measurements, another type of E-field probe was used. This probe was constructed by soldering a short, vertical rod to the tip of a high impedance FET probe. The probe body was covered by copper tape, forming a small hump on the ground plane. This type of field probe is seen in the photo in Figure 60.

This probe was calibrated in a test chamber with a D-dot sensor used as a standard reference probe, per the requirements of IEEE Std. 1309-1996 [18]. For these measurements, the D-dot sensor was not sensitive enough to be useful.

### 6.3.2 H-field probes

To measure the magnetic field strength away from the ground plane, a balanced loop sensor with a 30 cm diameter was used. This sensor is shown in the photo in Figure 64. Unlike the spherical E-field sensor, this loop has no internal electronics or fiber optics capability, so the output signal from the sensor is fed to a near-by fiber optics transmitter by a coaxial cable, and then on to the network analyzer by the fiber optic cable.

For measurement on the ground plane, a different sensor was used. This sensor consisted of a short-circuited half circular loop, connected at both ends to a brass plate. The current in this half-loop was measured using a clamp-on current probe. This sensor configuration was calibrated in the a chamber with a B-dot sensor used as a standard reference.

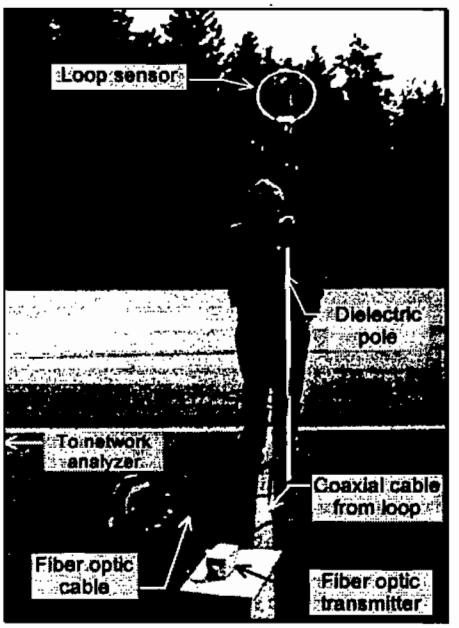


**Figure 64. The H-field loop sensor and fiber optic transmitter, shown for a measurement height of 2.5 m over the ground.**

### *6.4 Summary of P×M Measurement Results*

The overall goal of this measurement program was to gather data to better understand the behavior of p×m antennas. This was done by trying to analyze and understand the measurements, and by comparing the measurements with results from numerical simulations. In these measurements, several specific issues were investigated, including

- How to experimentally determine the required loading of the antenna for p×m operation
- Mapping of the E- and H-fields on the center line of the antenna at different distances
- Investigation of the E- and H-field variations off of the antenna axis
- Study of the EM wave impedance variations near the antenna
- Investigation of the effects of a lossy earth on the antenna

In this subsection, the results of the various measurements are summarized and compared with numerically calculated values. Subsections 6.4.1 — 6.4.4 deal with the scale model antenna, and subsections 6.4.5 — 6.4.9 treat the large antenna. For these calculations, the NEC model of the antenna has been used. Generally, we note that the agreement between the theory and experiment is much better for the case of the scale model antenna and highly conducting ground plane, than for the large antenna and the lossy earth. This is not unexpected, given the large uncertainties as to the exact nature of the earth near the large antenna.

### 6.4.1 Measurement #1 - Load Impedance Determination for the Scale Model Antenna

The first measurement sequence was designed to determine the optimum resistance loading for the p×m antenna selected for this experiment. The design curves for the antenna load presented in Figure 16 show that a load resistance of approximately $R_L \approx$ 275 Ω is needed for the this p×m antenna, if the wire radius is $a$ = 1 mm. Refining this calculation for the scale model wire radius of $a$ = 0.3 mm provides a load resistance of $R_L$ = 240 Ω . Resistance values of 100, 220, 270, 330, 390, 470, 560, 680 and 820 Ω were chosen to bracket this calculated estimate, and measurements of the E-field produced by the antenna were taken.

To find the best choice for the antenna load resistance, the vertical E-field was measured on the ground plane at a point located 2 m from the closest point of the antenna in the backward direction (point R in Figure 62). Figure 65 illustrates the relative values of the measured $E_z$ fields for the scale model antenna for different load resistances. These E-fields have been normalized by the voltage source $V_o$ shown in Figure 54. As discussed in Appendix B, this voltage is different from the reference voltage $V_{ref}$ which is measured by the network analyzer. As a consequence, the measured values must be corrected to account for this difference. Furthermore, the presence of the 55 dB amplifier in the antenna excitation channel must be taken into account. This also is discussed in the appendix.

For the observation distance of -2 meters, the frequency at which $k\alpha \approx 1$ is approximately 25 MHz. Consequently, the E-field minimization process should be carried out near this frequency. The various measurements of the E-field strength show that the minimum value is not very distinct in practice; the field cancellation is not perfect. Based on the data shown in the figure, the best resistance value was judged to be $R_L \approx 270\ \Omega$, which is the thicker trace in the figure. For this case, the E-field strength is minimized over most of the frequency range. It is interesting to note that for the very low frequencies the measurements show that the E-field strength is *independent* of the load resistance. This observation is consistent with the results from the quasi-static charge on the antenna, as discussed in Section 2.1, since the static integral equation for the charge derived from Eq.(5) does not contain a dependence on the load resistance. (The load resistance enters into the determination of the current, and hence, is important in determining the low frequency behavior of the magnetic dipole moment.) In all of the remaining measurements of the smaller p×m antenna, this 270 Ω resistance value has been used.

As mentioned in Section 2.2 another possibility for setting the correct antenna resistance can be envisioned. This involves making 2 field measurements of appropriate components of $E$ and $H$ in the forward direction to compute the wave impedance. We then require that the resistance be adjusted so that this impedance is equal to the free-space wave impedance. In our measurements for the scale model antenna, we elected to use the $E$-field minimization procedure because it required only one measurement per

resistor value. For the larger antenna, this alternate method of determining the load resistance was used, and will be illustrated later.

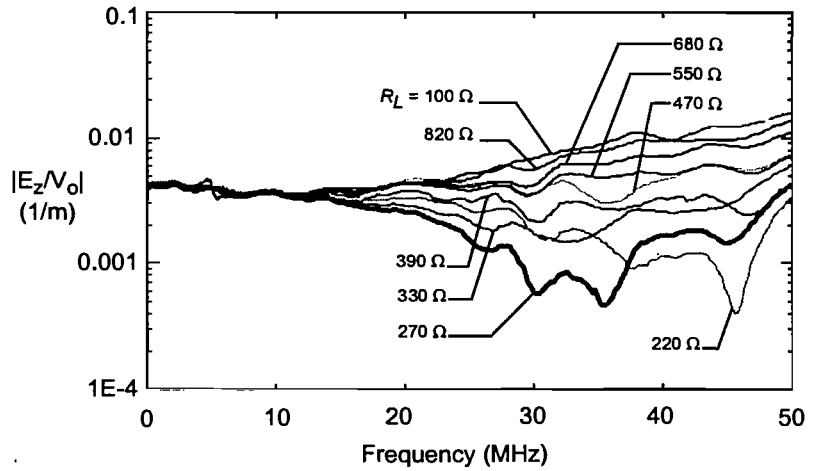


**Figure 65. Plot of the measured $E_z$ field magnitude on the mesh groundplane for the scale-model p×m antenna in the backward direction at $x$ = -2 m (point *R*), for different antenna load resistances.**

It is useful to compare these measured E-field responses in the backward direction with theoretical results for the same antenna shape using an integral equation analysis. Figure 66 presents the computed E-fields for the same load resistors used for Figure 65, as computed with the NEC code.

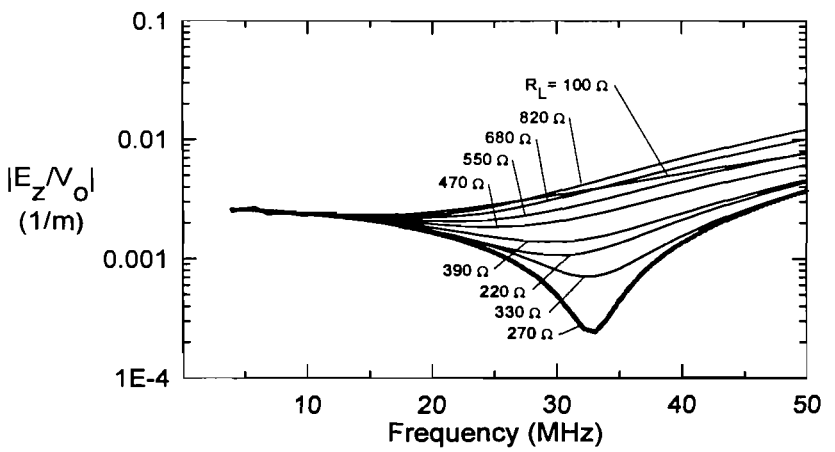


**Figure 66. Plot of the computed $E_z$ field magnitude for the scale-model p×m antenna on a perfect ground in the backward direction at $x$ = -2 m (point *R*), for different antenna load resistances.**

In examining the data in Figure 65 and Figure 66 we see that the behavior of the E-fields is similar and the choice of the 270 Ω load resistance is confirmed. However, the low-frequency measured asymptotic value for the family of curves is on the order of $E_z/V_o = 3.99 \times 10^{-3}$ (1/m), and the computed values are about $2.50 \times 10^{-3}$ (1/m). Thus, the

computed values are about 37% lower than the measured responses. This difference can be due to a wide variety of factors, including:

- errors in the sensor calibration
- uncertainties in the 55 dB amplifier gain
- errors in field probe placement, and
- modeling errors in the numerical analysis using NEC

Of all of these factors, the sensor calibration error is thought to be most significant. Although the sensors were carefully constructed and calibrated in a measurement chamber, a number of uncertainties in the calibration data and the sensor wire shape are possible. Furthermore, the hump on the ground plane can provide errors in the measurements.

### 6.4.2 Measurement #2 - E-Field Mapping in the Forward Direction of the Scale Model Antenna

With the determination of the proper antenna load resistance of 270 Ω, it was desired to determine how the E-fields produced by the antenna varied spatially. A total of twelve test points were chosen in the forward direction of the antenna, forming a possible *test volume* for the antenna. Eight test points were along the symmetry line, and these included points *1*, *2*, *3*, *4*, *6*, *7*, *8*, and *9*. In addition, measurements were made at points *A*, *B*, *C*, and *D* , as well as at point *R* in the backward direction.

#### *6.4.2.1 E-fields along the antenna centerline*

Figure 67 illustrates the measured vertical electric field on the ground at the test points along the $x$-axis. These data are again normalized by the voltage excitation source of the antenna, $V_o$. Test points *1* — *9* are in the forward direction, and test point *R* is in the backward direction. In this plot, the upper frequency limit for p×m operation at approximately 56 MHz is indicated by the dashed line.

It is interesting to compare the responses in the forward and backward direction. Test point *3* is symmetric with the test point *R* in the backward direction — both are 2 meters from the closest extent of the antenna. This figure clearly shows that at low frequencies ($kr < 1$) the E-fields in the forward and reverse direction approach the same value. At this point, the antenna is behaving like a small electric dipole, as far as the E-field is concerned.

A comparison of these measured results with calculated responses at the same test point locations is possible. Figure 68 presents the calculated results, for frequencies starting at 5 MHz. Lower frequencies posed a problem for the NEC code, and consequently, these responses are not shown. As may be noted in comparing Figure 67 and Figure 68, the agreement between the two is reasonable.

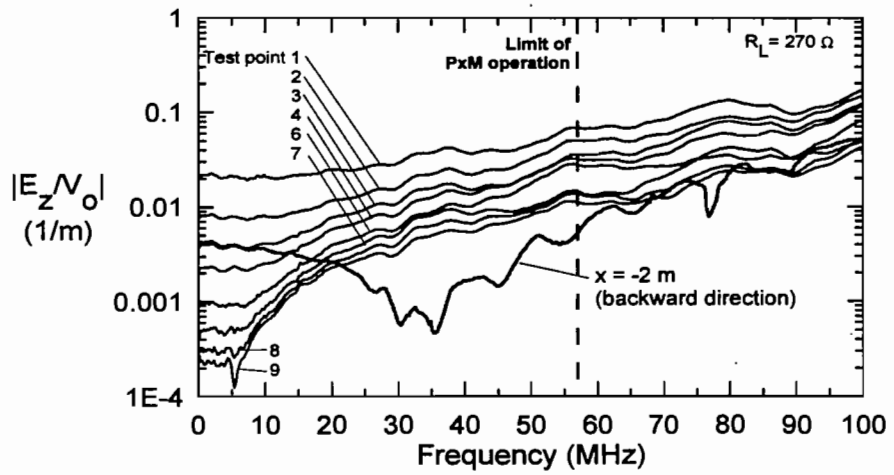


**Figure 67. Plot of the measured $E_z$ field magnitude on the mesh groundplane for the scale-model p×m antenna at various test points. (Antenna load resistance $R_L$ = 270 Ω.)**

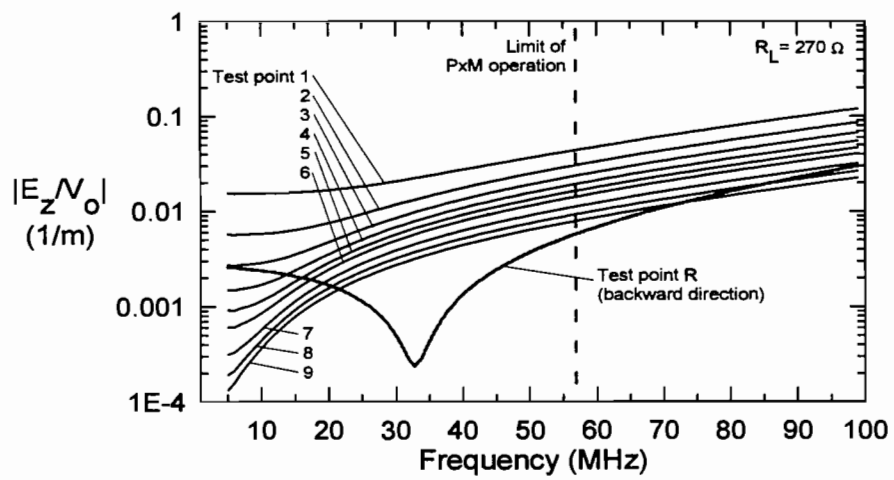


**Figure 68. Plot of the computed $E_z$ field magnitude for the scale-model p×m antenna at various test points. (Antenna load resistance $R_L$ = 270 Ω.)**

*6.4.2.2 E-fields along the A-B-C-D contour*

It is useful to understand how the primary E-field varies in the transverse direction. Measurements of the vertical field were also made at test points *A, B, C* and *D* and the results are shown in Figure 69. Also shown are the measurements for test points 2 and 3 which are located along the *x*-axis centerline.

Ideally, the vertical E-field at points A and D, and at B and C, should be the same. The differences between these two sets of measurements illustrate the asymmetry in the field near the antenna, and perhaps is due to unwanted scattering from the ground plane mesh or other imperfect ground interactions.

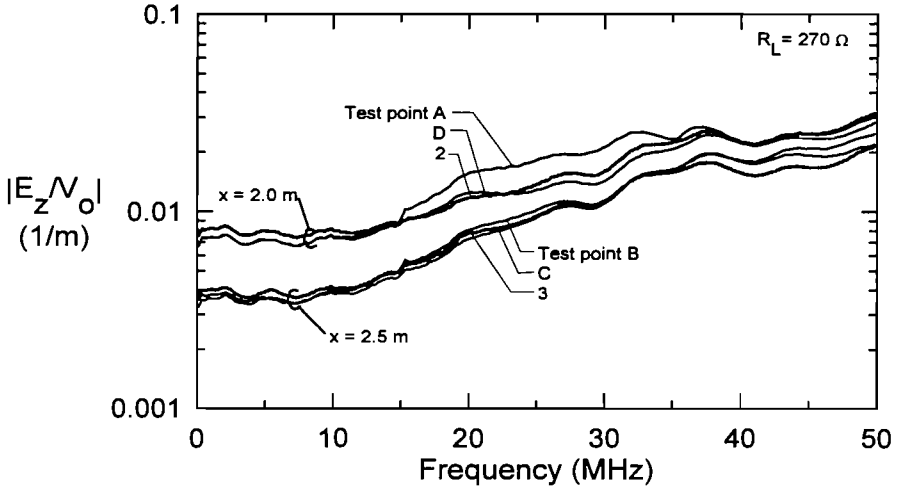


**Figure 69. Plots of the measured $E_z$ field on the ground plane along the rectangular contour bounded by test points A, B, C and D for the scale model p×m antenna.**

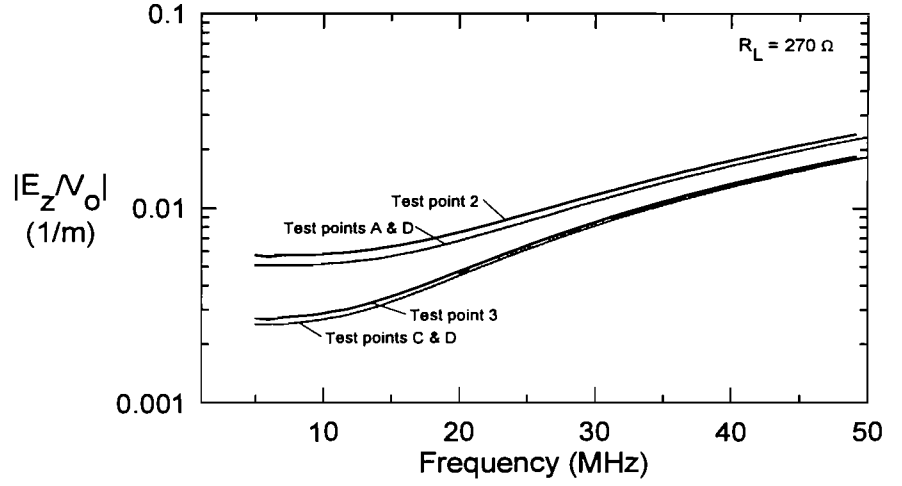


**Figure 70. Plots of the computed $E_z$ field on the ground plane along the rectangular contour bounded by test points A, B, C and D for the scale model p×m antenna.**

### 6.4.3 Measurement #3 - H-Field Mapping in the Forward Direction of the Scale Model Antenna

*6.4.3.1 H-fields along the antenna centerline*

For the scale model antenna, magnetic field measurements were made at the test points *1, 2, 3, 4, 6, 7, 8* and *9*. The results of these measurements for the primary $H_y$ component normalized by the voltage $V_o$ are presented in Figure 71. (Note that the frequency scale in this plot is logarithmic, as opposed to the linear plots for the E-fields).

The behavior of the magnetic field is similar to that of the electric field. At low frequencies, the field approaches a constant value, corresponding to that of a magnetic dipole moment. Figure 72 plots the corresponding calculated H-field components at the same test points, and the agreement with the measurements is good.

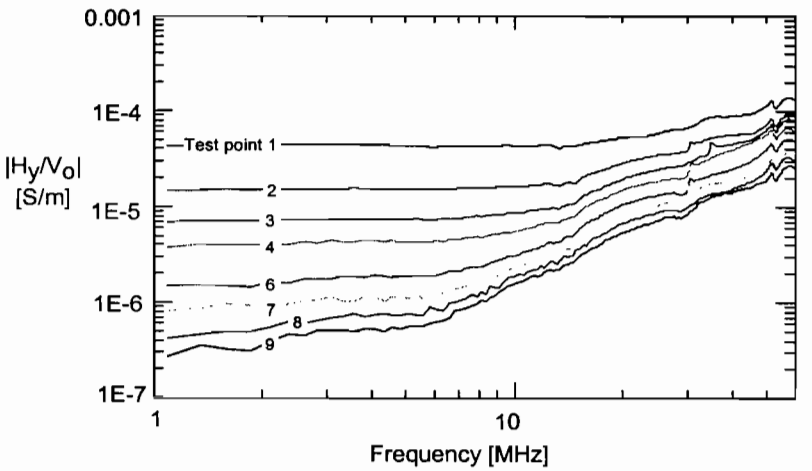


**Figure 71. Plot of the measured $H_y$ field magnitude on the mesh groundplane for the scale-model p×m antenna in the forward direction at different test point locations.**

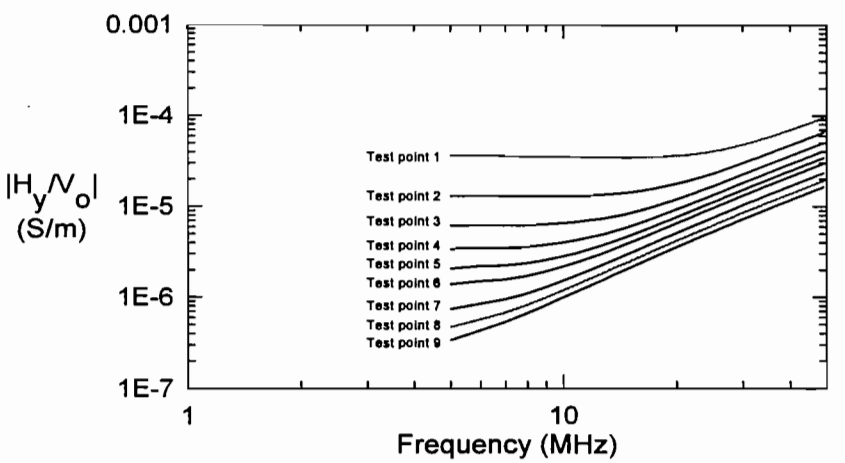


**Figure 72. Plot of the calculated $H_y$ field magnitude for the scale-model antenna on a perfect ground plane in the forward direction at different test point locations.**

*6.4.3.2 H-fields along the A-B-C-D contour*

Measurements of the $H_y$ field were conducted at test points *A, B, C* and *D,* and the results are shown in Figure 73. The corresponding theoretical values are plotted in Figure 74. In these figures, the responses for points 2 and 3 along the *x*-axis centerline are included. These plots indicate a significant variation in the H-field over the ABCD area. It is interesting to note that the $H_y$-field at test point 2 is larger than at points *A* or *B*. This difference is still evident at the more distant points *B, 3* and *C,* but the difference is not as large.

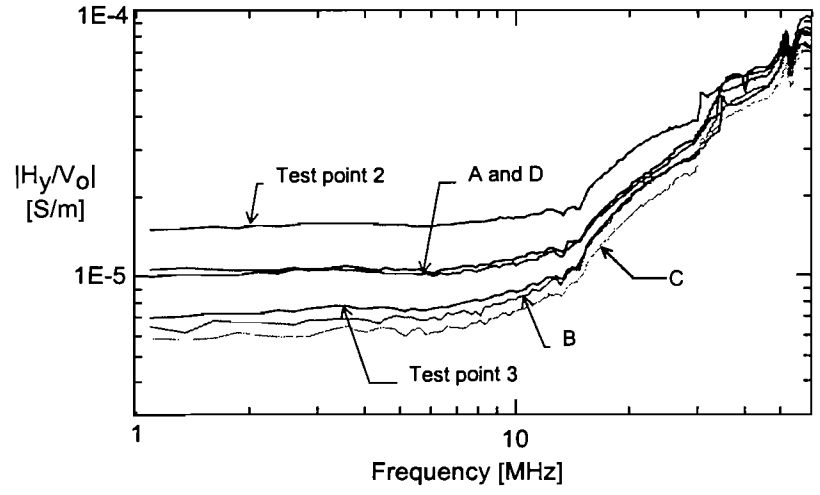


**Figure 73. Plots of the measured $H_y$ field for the scale model antenna on the ground plane along the rectangular contour bounded by test points A, B, C and D.**

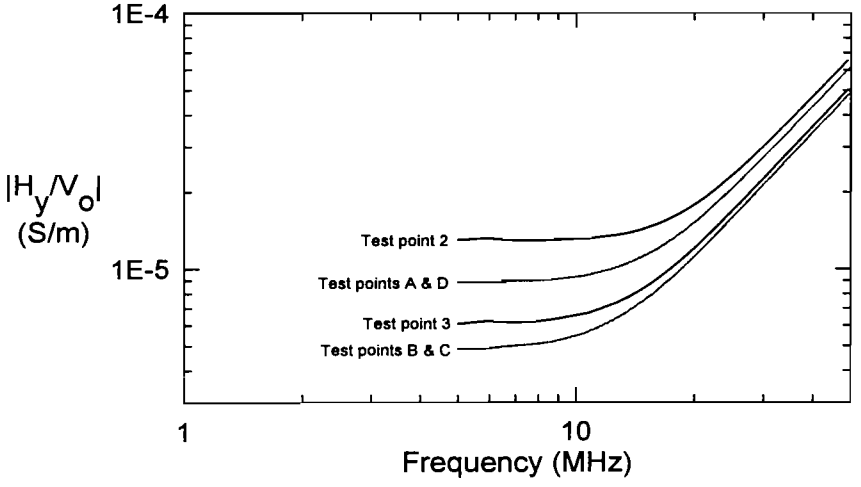


**Figure 74. Plots of the calculated $H_y$ field for the scale model antenna on a perfect ground plane along the rectangular contour bounded by test points A, B, C and D.**

### 6.4.4 Wave Impedance in the Forward Direction of the Scale Model Antenna

*6.4.4.1 Impedance along the antenna centerline*

With the E and H-field measurements in the forward direction, it is possible to take the ratio $-E_z/H_y$ to obtain the wave impedance for the primary field components. In doing this, the resulting data are presented as a function of normalized frequency $kx = 2\pi fx/c$, so as to permit a comparison with the near-field impedance of point dipole sources (see figure 6 of [1] ). These derived results are presented in Figure 75 for the test locations 1, 2, 3, 4, 6, 7 and 8. Test point 5 was not measured and the data for test point 9 are omitted, because the magnetic field measured at this location was small and rather noisy, providing questionable results for the impedance.

Figure 76 illustrates the calculated wave impedance for the same scale model antenna over a perfect ground plane at test point locations 1 through 9. In addition, the theoretical value of the impedances for the point electric and magnetic dipoles located at the antenna origin are replotted in this figure for comparison purposes.

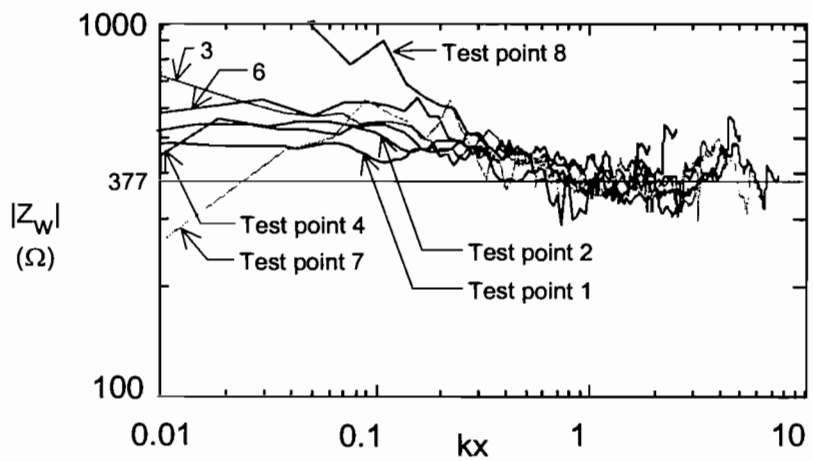


**Figure 75. Plot of the measured wave impedance $Z_w$ magnitude on the mesh groundplane for the scale-model p×m antenna in the forward direction at different $x$ locations, as a function of normalized frequency $kx$.**

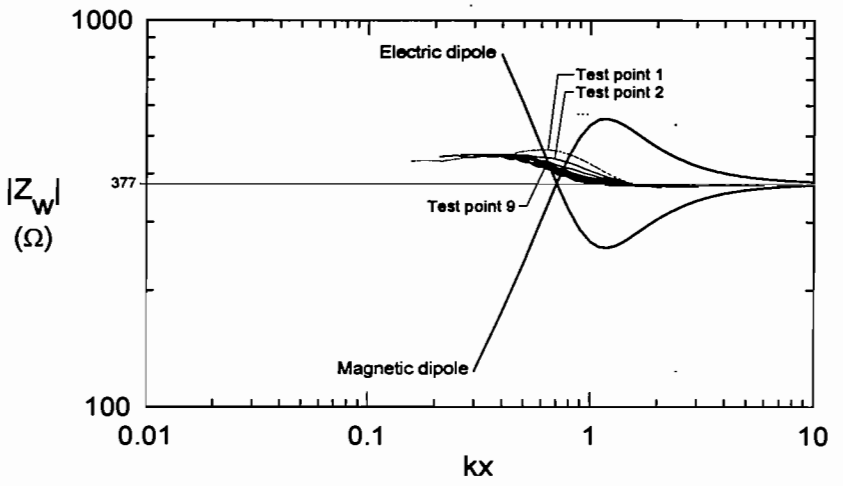


**Figure 76. Plot of the calculated wave impedance $Z_W$ magnitude for the scale-model p×m antenna on a perfect ground, as a function of normalized frequency *kx*.**

From these plots, we note that the p×m antenna behaves as expected. At high frequencies (or equivalently, in the far field) the E/H ratio of the primary field components is very close to the free-space value of 377 Ω. At $kx \approx 1$, the ratio between electric and magnetic field strength is slightly higher than 377 Ω, suggesting that there may be too much of an electric dipole moment contribution to the composite antenna. From the comparisons with dipoles at low frequencies, it appears that a lower load resistance, say $R_L \approx 220$ Ω, may be a better choice for the p×m operation of this antenna.

Notice that test point 8, which is the most distant point in this measurement sequence, seems to deviate from the rest of the data and from the calculated results as well. This is attributed to noise in the more distant measurements, and is one reason why the data for test point 9 was deemed unreliable.

*6.4.4.2 Impedance along the A-B-C-D contour*

Figure 77 shows the wave impedance variation in the rectangular area defined by the test point sequence 2, A, B, 3, C and D. The main reason for these rather large deviations in the impedance is again due to the large variations in the measured H-fields, as seen in Figure 73. A consequence of this variation in the magnetic field data is that in a real testing situation, one must be very careful to maintain a high quality in the field illumination and in the measurements. Figure 78 presents the corresponding calculated wave impedance for the scale model antenna over a perfect ground.

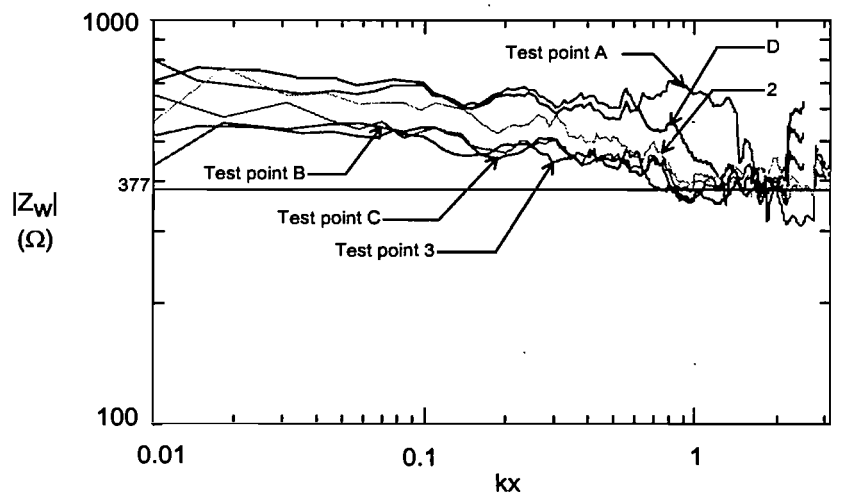


**Figure 77. Plot of the measured wave impedance $Z_w$ magnitude on the mesh groundplane along the rectangular contour bounded by test points A, B, C and D.**

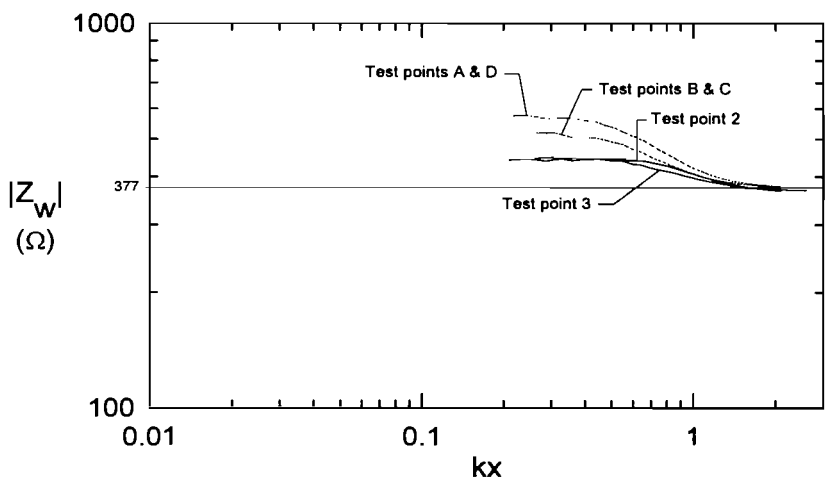


**Figure 78. Plot of the calculated wave impedance $Z_w$ magnitude on the mesh ground plane along the rectangular contour bounded by test points A, B, C and D.**

### 6.4.5 Measurement #4 - Input Impedance of the Large Antenna

With the large antenna of Figure 55, measurements of the input current were made as a function of frequency. This was done to insure that the antenna was being excited properly, and to observe the quality of the measuring system. As an example of the expected variation of the input impedance of this antenna, a series of NEC calculations was run for the antenna having load resistances of $R_L$ = 1, 100, 500, 1000, and 10000 Ω. For these calculations, the earth was assumed to have a conductivity $\sigma$ = 0.01 S/m and permittivity $\varepsilon_r$ = 10. Unless specified otherwise, all calculations for the large antenna in this section use these assumed values.

Figure 79 presents the results of these calculations for a range of frequencies up to 25 MHz. While this is well beyond the 5.6 MHz limit for p×m operation, these calculations serve to show that the input impedance corresponds to what one expects for a loaded loop antenna. At very low frequencies, the input impedance corresponds to the load resistance. For the nearly short-circuited case ($R_L$ = 1 Ω), we expect an antenna resonance (manifested by a *minimum* of the input impedance) to occur when the total antenna length is one wavelength. This corresponds to a frequency of about 18 to 19 MHz, and it is clearly evident in the figure.

There are several frequencies (≈ 4.5, 13.5 and 24 MHz) at which the input impedance of the antenna is independent of the load resistance. This occurs when the antenna current distribution has a null at the load position. No current at this point implies that the presence or absence of a load is unimportant in determining the load resistance. It is also interesting to note that the load resistance $R_L$ = 1000 Ω appears to give a relatively flat input impedance at low frequencies.

For the case of a nearly open-circuited antenna ($R_L$ = 10,000 Ω), the antenna should have its first resonance at roughly one-half of the full-loop resonance, or at about 9 MHz. This null in $Z_{in}$ is also evident.

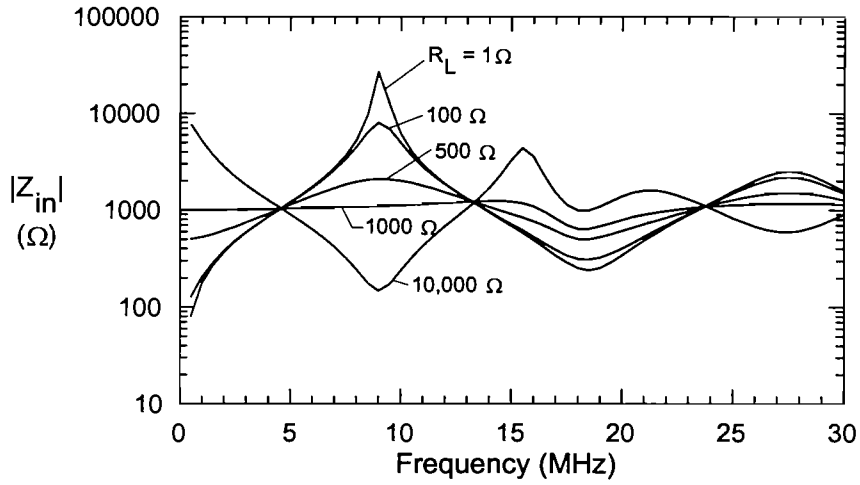


**Figure 79. Plot of the NEC-computed input resistance of the large p×m antenna for an assumed earth conductivity $\sigma$ = 0.01 S/m and permittivity $\varepsilon_r$ = 10.**

Measurements were conducted from 100 KHz to 10 MHz for the large antenna, and the results are shown in Figure 80 for three different load resistances. Part *a* of this figure presents the magnitude of the measured input impedance, and part *b* shows the measured phase in radians. Figure 81 shows the computed values of the magnitude of $Z_{in}$ for the specific load resistances over the same frequency range.

The agreement between the theoretical and measured results is not very good in this case. Unfortunately, we do not know how the asphalt layer influences the antenna impedance. The 5 meter long base wire of the antenna is very close to the asphalt, for

which the conductivity is unknown. Furthermore, the earth may be a stratified medium and its influence is uncertain.

However, certain important trends exist in the measured data. At very low frequencies, the impedances are approaching the proper DC values given by the load on the antenna. The coalescence of the impedances at a single point occurs at a frequency of about 3 MHz, which contrasts with 4.5 MHz for the calculated data. Finally, the anti-resonance at a frequency of about 8.8 MHz is noted in both the experimental and theoretical plots. Remaining to be explained, however, is the reason for the null in the measured impedances at 6 MHz.

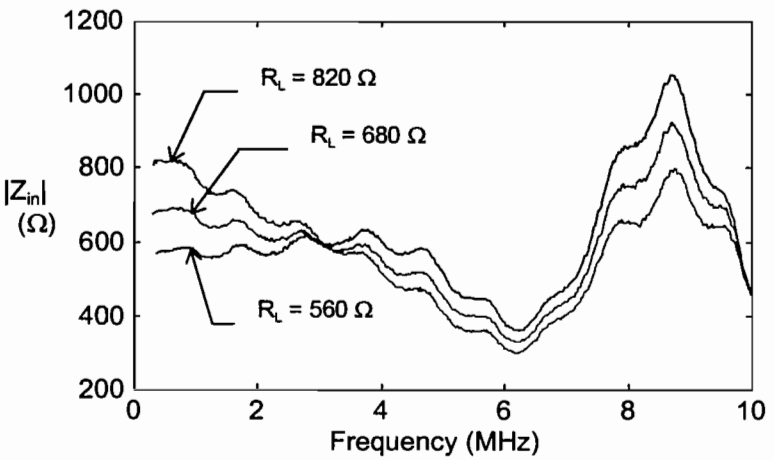


(a) Magnitude

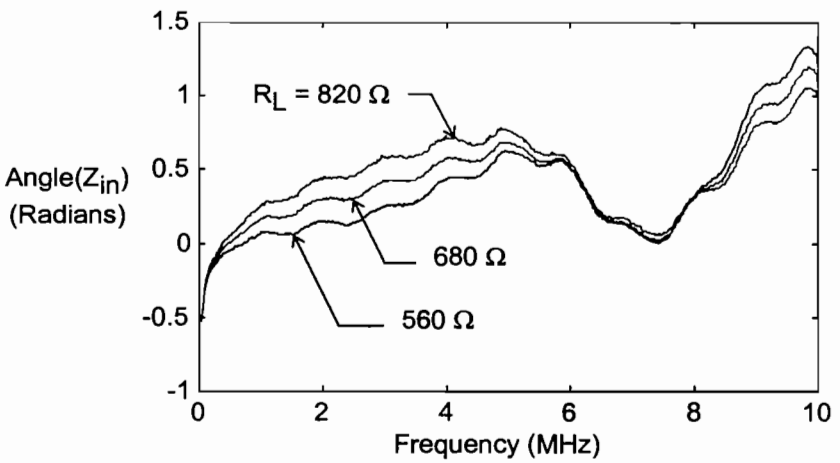


(b) Phase

**Figure 80. Plot of the measured input impedance magnitude and phase for the large antenna with different load resistances.**

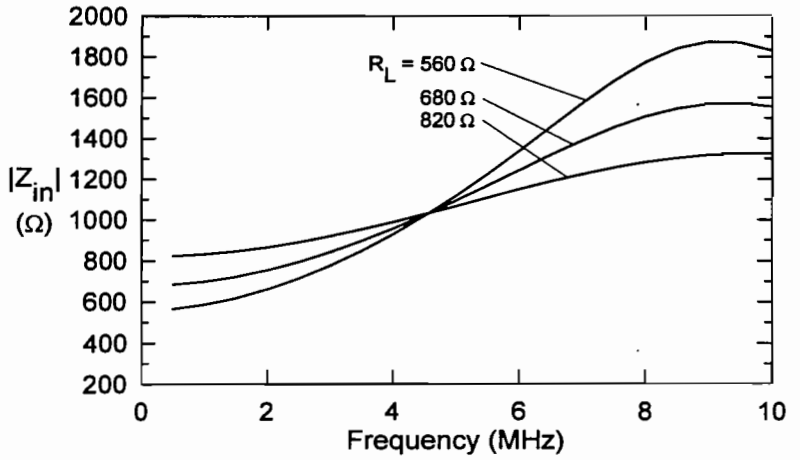


**Figure 81. Plot of the computed input impedance magnitude for the large antenna with different load resistances for an assumed earth conductivity $\sigma = 0.01$ S/m and permittivity $\varepsilon_r = 10$.**

### 6.4.6 Measurement #5 - Determination of the Antenna Load Resistance for Large Antenna

E- and H-field measurements were conducted on the large p×m antenna using the equipment configuration illustrated in Figure 56. These measurements were generally more difficult to perform and analyze, because the range of frequencies was a factor of 10 lower than for the scale model antenna. Noise and signal variability at low frequencies caused large variations in the measured fields. Furthermore, the situation is made more complicated by the presence of the lossy earth.

The first field measurements for the large antenna were performed to determine the best resistance for this antenna for p×m operation. For this antenna with a wire radius of $a = 0.4$ mm, the computed optimum resistance was $R_L = 306$ Ω. This value, however, is for the antenna over a perfect ground, and for the case of a lossy earth near the antenna, it is reasonable to expect that this value will change. Consequently, different resistor values of 220, 330, 470, 680, 1000, 1500, 2200, and 3300 Ω were chosen, and the $E_z$ and $H_y$ components at test point 2 in the forward direction were measured for a sensor height of $z = 1$ meter.

Figure 82 presents the measured results for the E-field, and the corresponding calculated values are shown in Figure 83. Both of these sets of curves show the same general trends in the data as the frequency is increased.

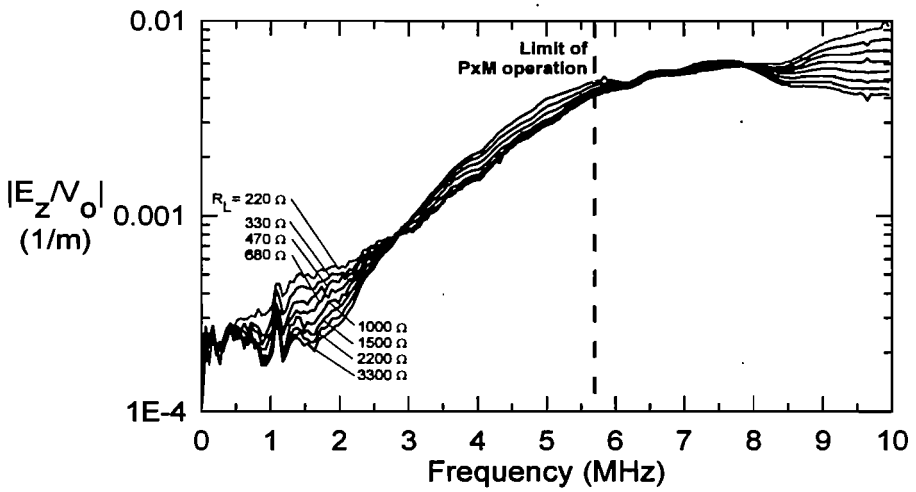


**Figure 82. Measured $E_z$ field at test point 2 for the large p×m antenna for different values of load resistance.**

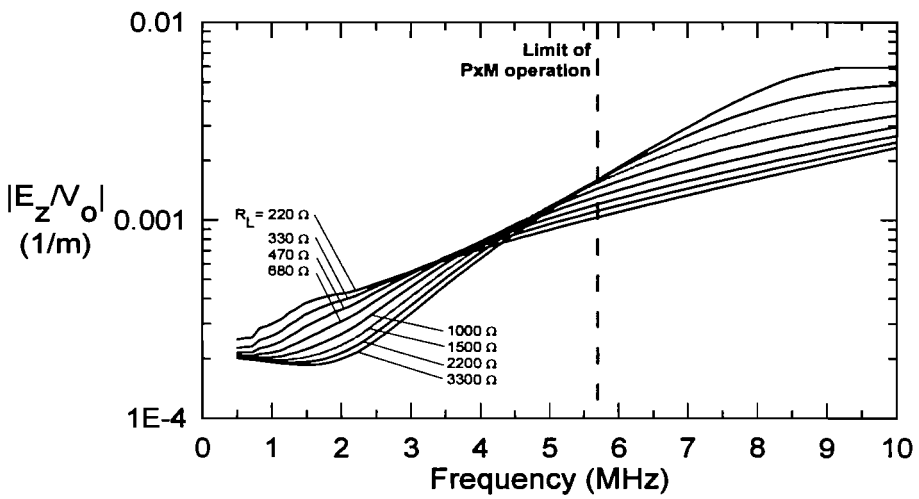


**Figure 83. Calculated $E_z$ field at test point 2 for the large p×m antenna for different values of load resistance.**

Similar plots for the magnetic field are shown in Figure 84 for the measurements and in Figure 85 for the computed responses. Notice the interesting anomaly in the low frequency responses that occur both in the measurements and in the calculations, and which evidently arises from the lossy ground interaction.

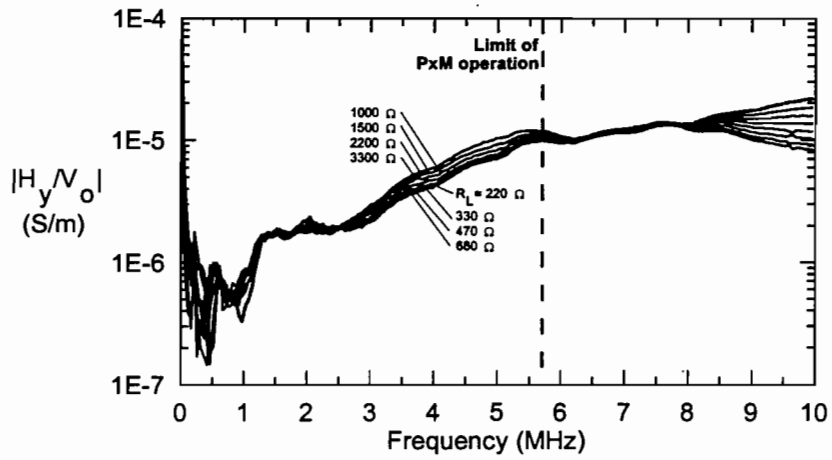


**Figure 84. Measured $H_y$ field at test point 2 for the large p×m antenna for different values of load resistance.**

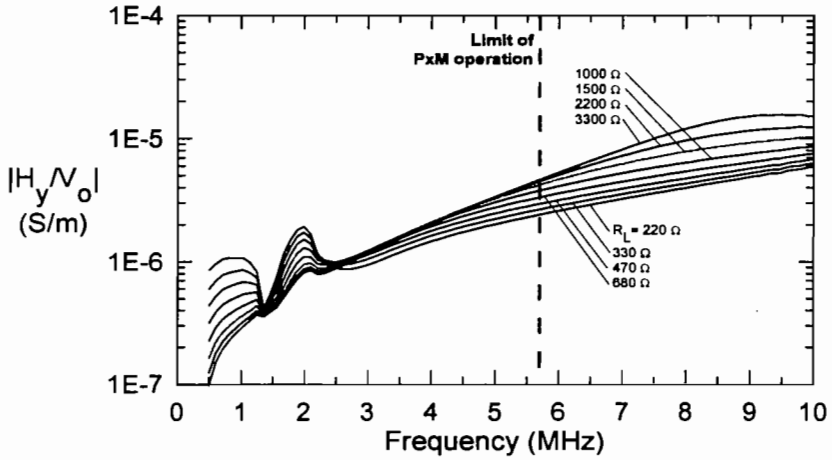


**Figure 85. Calculated $H_y$ field at test point 2 for the large p×m antenna for different values of load resistance.**

Using the measured E and H fields at test point 2, the wave impedance may be calculated. This is shown in Figure 86 as a function of frequency. Notice that at frequencies below about 1 MHz, these results are questionable, primarily due to the noise in the H-fields that cause the curves to increase near zero frequency (see Figure 84.)

In comparing these results with the forward wave impedance for the scale model antenna in Figure 75, we note that there is a significant dip in the impedance at low frequencies (around 1 to 2 MHz) that is not present in the perfect ground case. Again, this appears to be an influence of the lossy earth on the fields surrounding the antenna. Figure 87 plots the calculated wave impedance from the NEC model and the general trend in the measurements is corroborated.

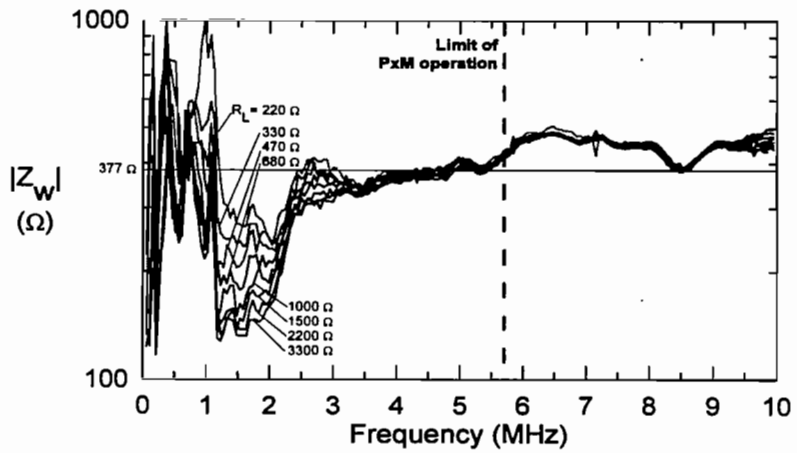


**Figure 86. The wave impedance $Z_W$ from the measured fields at test point 2 for the large p×m antenna for different values of load resistance.**

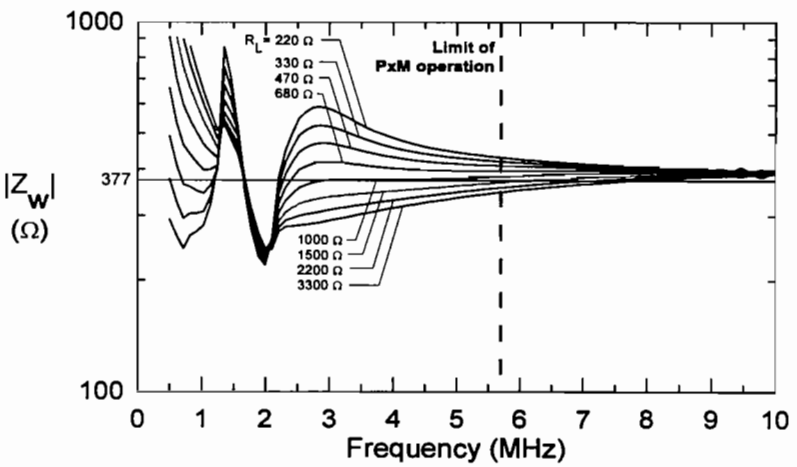


**Figure 87. The wave impedance $Z_W$ from the calculated fields at test point 2 for the large p×m antenna for different values of load resistance.**

From the data presented in Figure 86, it is not at all evident what the best choice of the antenna resistance should be. In an on-site assessment of the measurements, we estimated that an antenna load resistance of $R_L \approx 556\ \Omega$ would be reasonable. However, in retrospect, it appears from Figure 86 that something larger may be better. For example, the 1000 Ω value provides a good wave impedance match for frequencies greater than 2.5

MHz, according to the calculated model[4]. This value is difficult to determine from the measured data, however. For the remainder of the large antenna measurements, the 556 Ω value was used.

### 6.4.7 Measurement #6 - Variations of the $E_z$ Field Away from the Large Antenna

*6.4.7.1 E-fields along the antenna centerline*

The next sequence of measurements involved examining the behavior of the $E_z$ field at different test points for the large antenna. For a sensor height of $z$ = 1 m, Figure 88 presents the measured $E_z$ field magnitude for test points 2, 4 and 5 at $x$ = 20, 30 and 35 meters from the origin, respectively. Figure 89 presents the corresponding calculated fields, with good agreement in the shape of the curves, but with a difference in magnitudes of about 2 to 3. Generally, we find that the calculated responses are lower than the corresponding measured values.

The plots in Figure 90 and Figure 91 show the variation of the fields at a height of $z$ = 2.5 meters, but this time for test points 2, 3 and 5. An indication of how the E-fields vary with height is provided in Figure 92 for the measured quantities, and in Figure 93 for the calculated values.

[4] It is interesting to note that the value of $R_L \approx 1000\ \Omega$, which is obtained from the wave impedance plot in Figure 87, is also the same value for the input impedance magnitude $|Z_{in}|$ for the antenna when all of the curves in Figure 81 for difference antenna loads coalesce. In the corresponding plot for the measured values in Figure 80, the resistance value is about 600 Ω, which is consistent with the estimated value of 556 Ω. The differences between these experimental and calculated resistance levels suggest that the assumed earth parameters are not chosen correctly for the calculations.

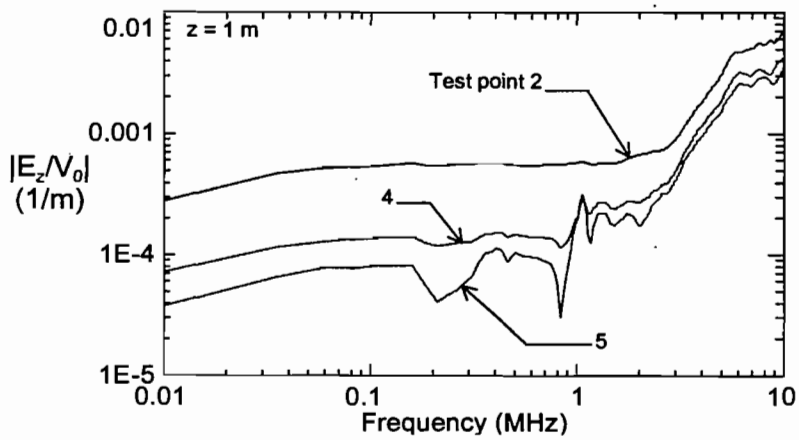


**Figure 88. The measured $E_z$ field for three test points along the $x$-axis as a function of frequency for the large antenna over an imperfectly conducting earth at a height of $z = 1$ m.**

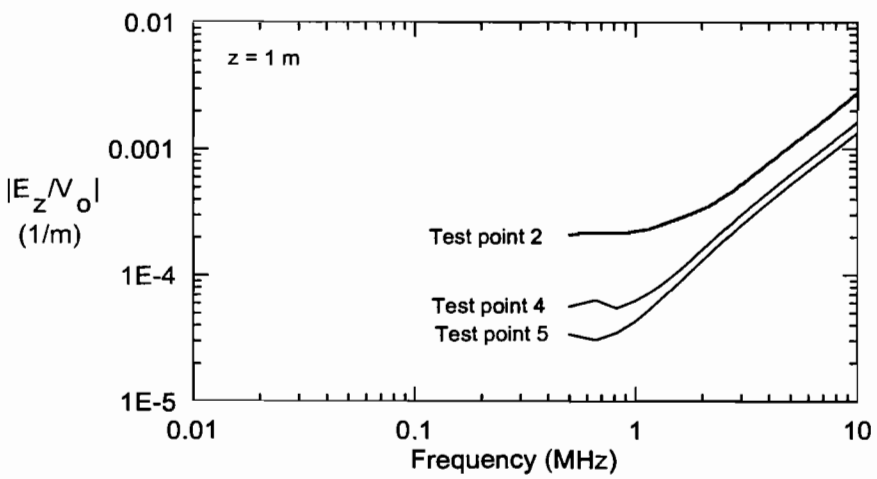


**Figure 89. The calculated $E_z$ field for three test points along the $x$-axis as a function of frequency for the large antenna over an imperfectly conducting earth at a height of $z = 1$ m.**

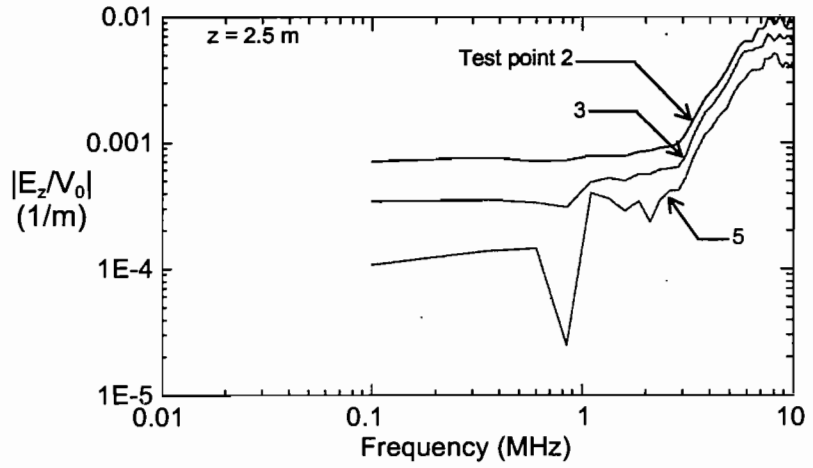


**Figure 90. The measured $E_z$ field for three test points along the $x$-axis as a function of frequency for the large antenna over an imperfectly conducting earth at a height of $z = 2.5$ m.**

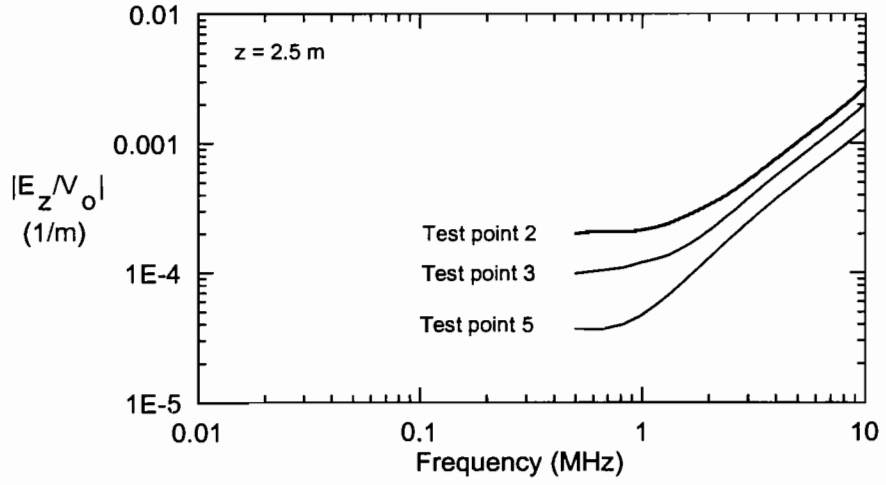


**Figure 91. The calculated $E_z$ field for three test points along the $x$-axis as a function of frequency for the large antenna over an imperfectly conducting earth at a height of $z = 2.5$ m.**

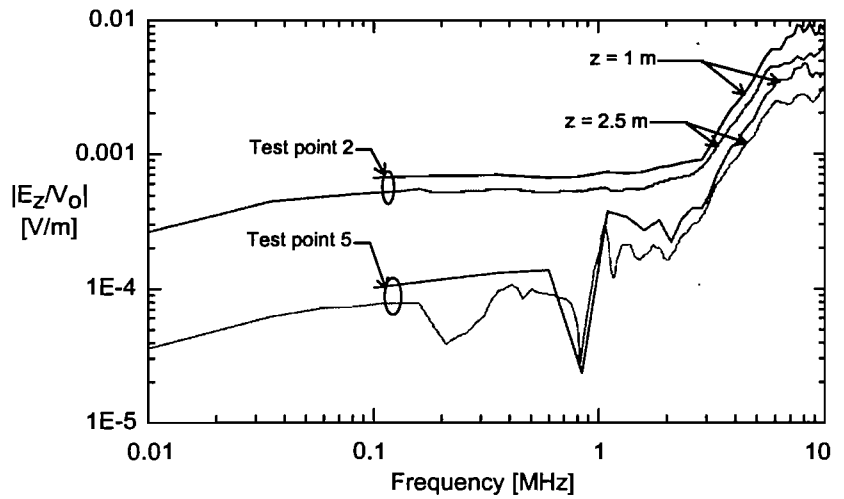


**Figure 92. Variation of the measured $E_z$ field at test points 2 and 5 for two different heights over the imperfectly conducting earth.**

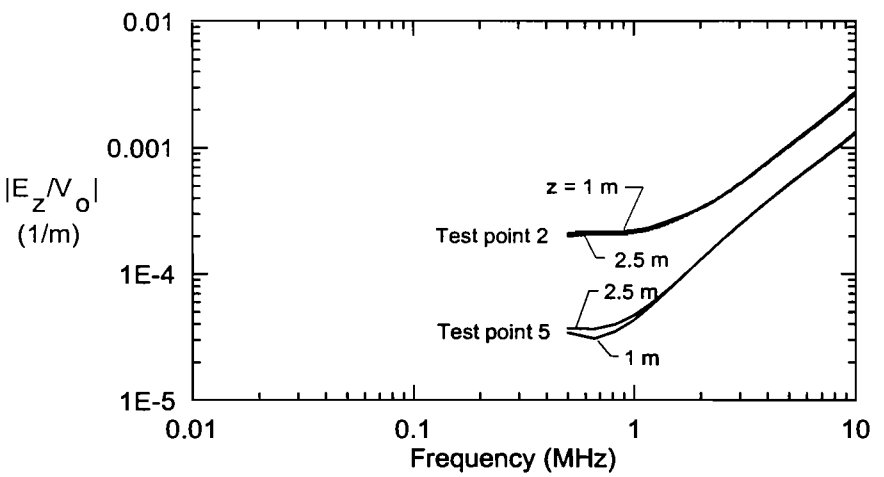


**Figure 93. Variation of the computed $E_z$ field at test points 2 and 5 for two different heights over the imperfectly conducting earth.**

*6.4.7.2 E-fields along the A-B-C-D contour*

$E_z$ fields were measured along the contour A-B-C-D to provide an indication of the transverse variation of the fields for the large antenna. Figure 94 presents the measured data for a sensor height of $z$ = 1 meter and the computed field strengths from the NEC model are shown in Figure 95. Similarly, for a height of 2.5 meters, Figure 96 illustrates the measured data, with Figure 97 presenting the calculated values.

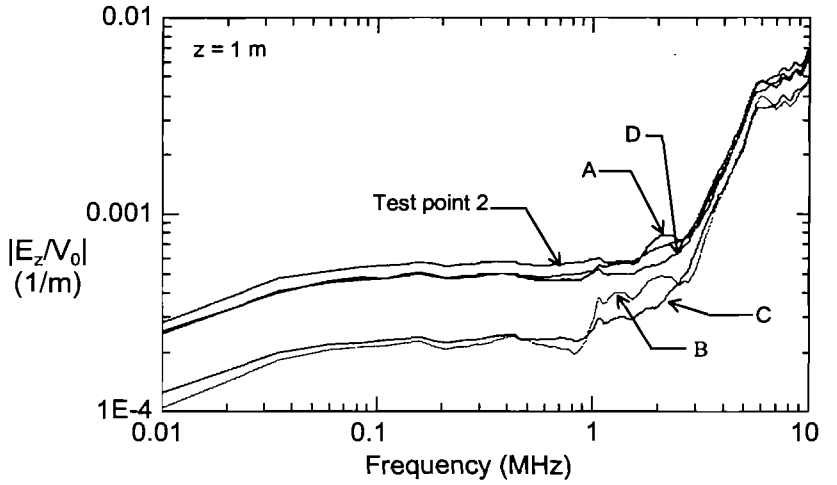


**Figure 94. Plots of the measured $E_z$ field at a height of 1 m along the rectangular contour bounded by test points A, B, C and D for the large antenna over the lossy earth.**

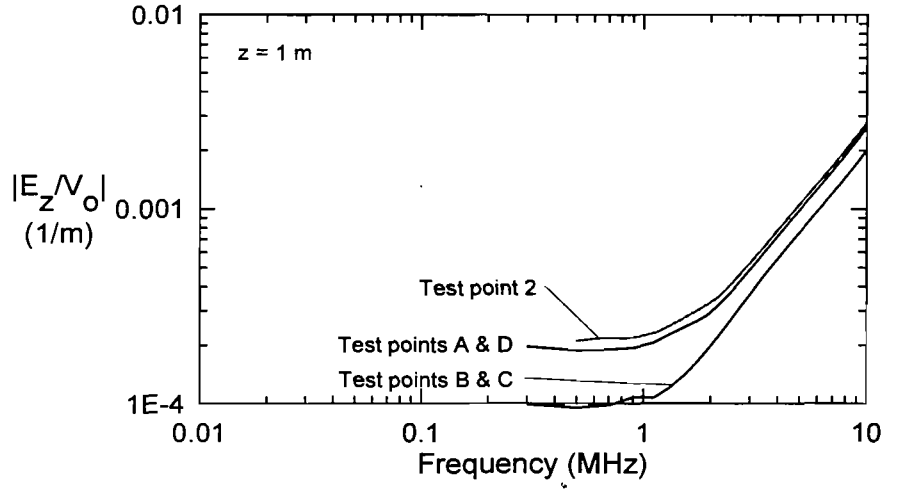


**Figure 95. Plots of the calculated $E_z$ field at a height of 1 m along the rectangular contour bounded by test points A, B, C and D for the large antenna over the lossy earth.**

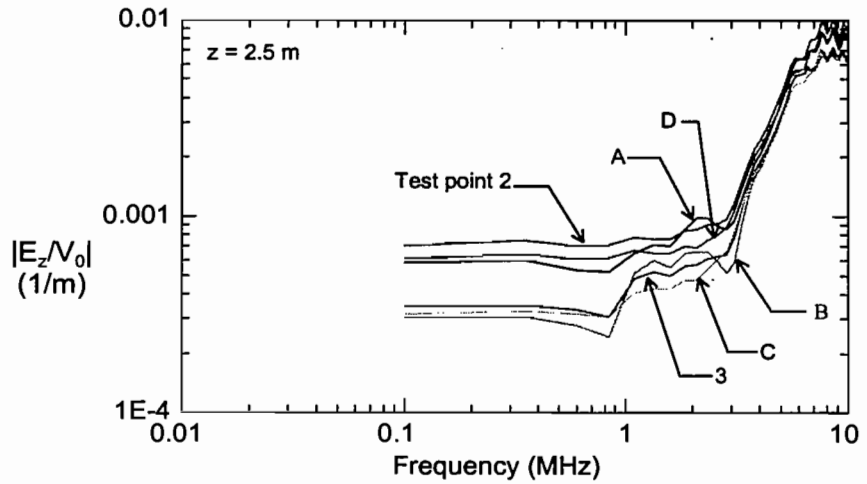


**Figure 96. Plots of the measured $E_z$ field at a height of 2.5 m along the rectangular contour bounded by test points A, B, C and D for the large antenna over the lossy earth.**

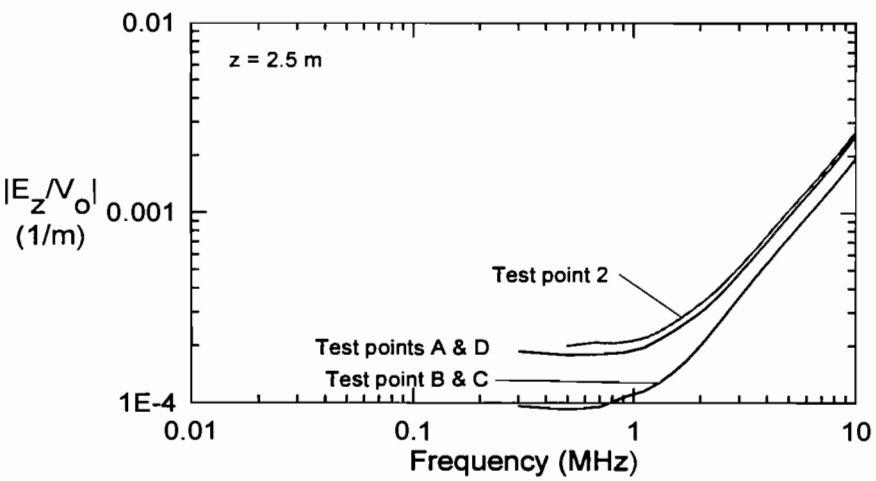


**Figure 97. Plots of the calculated $E_z$ field at a height of 2.5 m along the rectangular contour bounded by test points A, B, C and D for the large antenna over the lossy earth.**

### 6.4.8 Measurement #7 - $H_y$ Measurements for the Large Antenna

*6.4.8.1 H-fields along the antenna centerline*

H-field measurements were made for the larger antenna located over the lossy earth at a height of $z$ = 1 m. Figure 98 presents plots the magnitude of the $H_y$ field component at test points 2, 4 and 5 — the same locations as for the E-fields in Figure 88. In this figure, two different measurements were made at test point 2 on two different rainy days. These two curves demonstrate some of the changing conditions in the ground properties (at low frequencies), as well as the consistency in the field behavior (at high frequencies). Figure 99 plots the corresponding calculated values for these fields.

Figure 100 illustrates the measured $H_y$ field at test points 2 and 3 at a sensor height of $z$ = 2.5 m as a function of frequency, and the calculated responses are given in Figure 101.

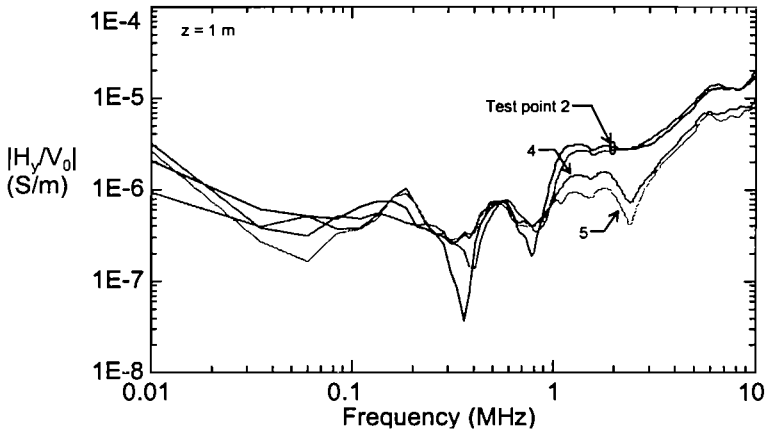


**Figure 98. Plot of the measured $H_y$ field for three test points along the $x$-axis as a function of frequency for the large antenna over an imperfectly conducting earth at a height of $z$ = 1 m. (Test point 2 measured twice.)**

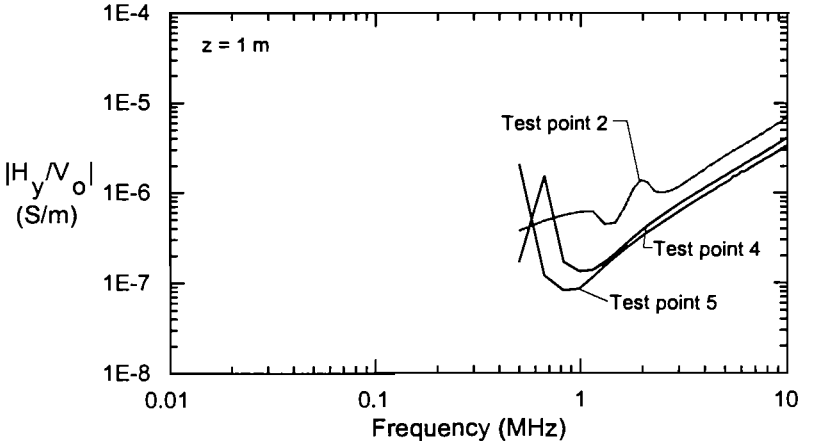


**Figure 99. Plot of the calculated $H_y$ field for three test points along the $x$-axis as a function of frequency for the large antenna over an imperfectly conducting earth at a height of $z$ = 1 m.**

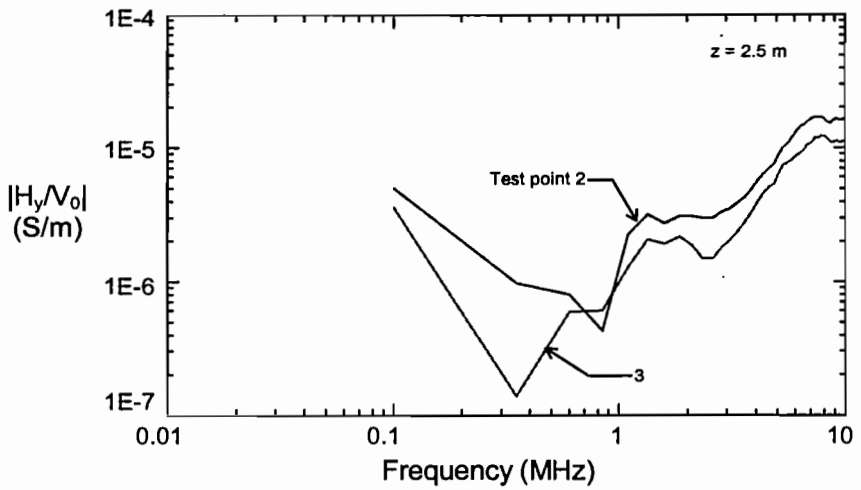


**Figure 100. Plot of the measured $H_y$ field for two test points along the $x$-axis as a function of frequency for the large antenna over an imperfectly conducting earth at a height of $h = 2.5$ m.**

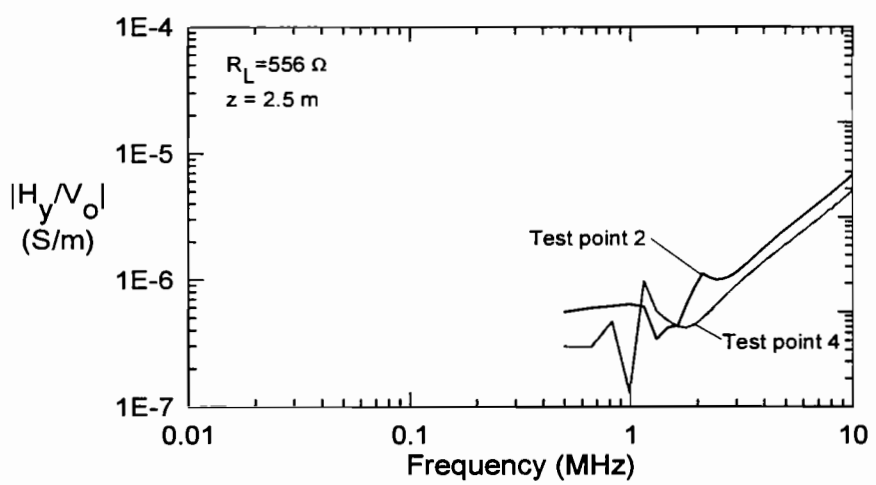


**Figure 101. Plot of the calculated $H_y$ field for two test points along the $x$-axis as a function of frequency for the large antenna over an imperfectly conducting earth at a height of $h = 2.5$ m.**

Unfortunately, in the H-field measurements involving different heights of the sensor, only one test point (2) was common in the measurement sets. Figure 102 illustrates the overlay of the two $H_y$ field component responses at this point for $z = 1$ and 2.5 m. Figure 103 presents the calculated responses.

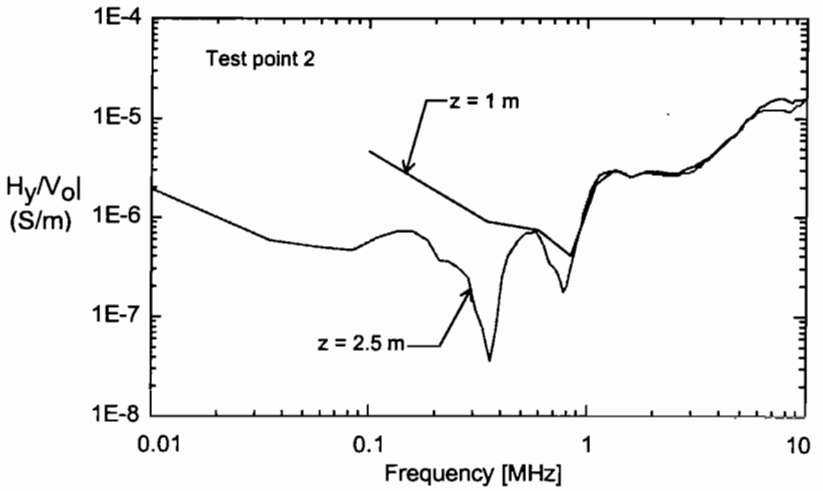


**Figure 102. Variation of the measured $H_y$ field at test point 2 for two different heights over the imperfectly conducting earth.**

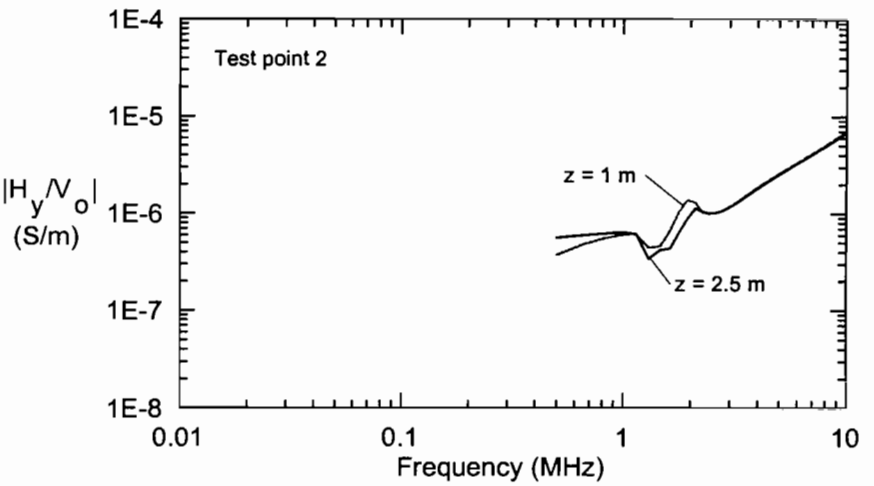


**Figure 103. Variation of the calculated $H_y$ field at test point 2 for two different heights over the imperfectly conducting earth.**

*6.4.8.2 H-fields along the A-B-C-D contour*

H-field variations in the A-B-C-D contour were made for the large antenna at the two sensor heights. Figure 104 presents the measured normalized $H_y$ field at $z$ = 1 meter, and Figure 105 illustrates the corresponding calculated values for comparison. For the $z$ = 2.5 meter case, Figure 106 presents the measured data, with the calculated results being shown in Figure 107.

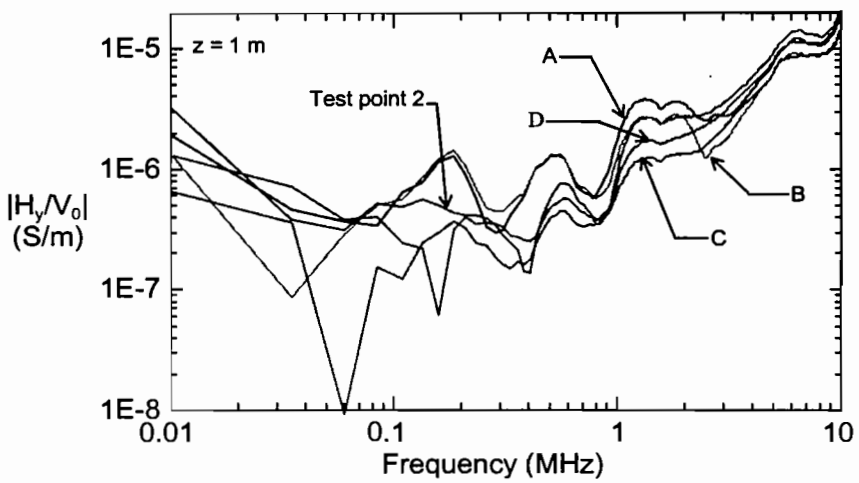


**Figure 104. Plots of the measured $H_y$ field at a height of 1 m along the rectangular contour bounded by test points A, B, C and D for the large antenna over the lossy earth.**

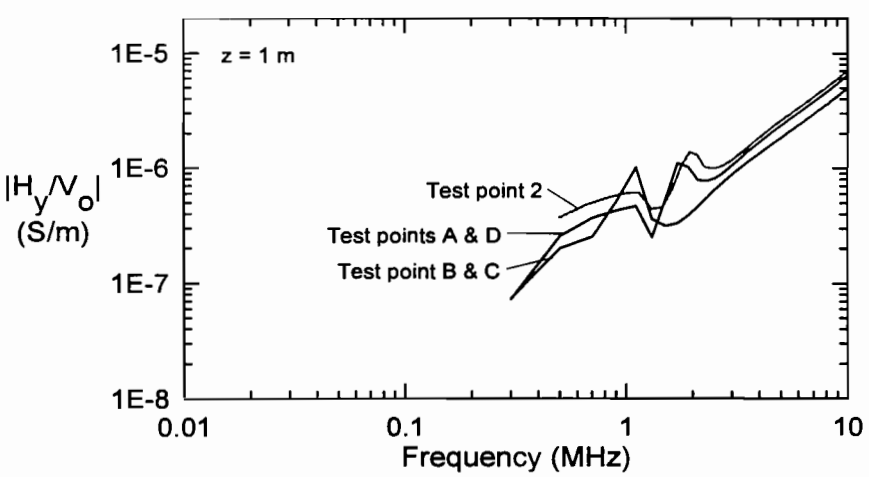


**Figure 105. Plots of the calculated $H_y$ field at a height of 1 m along the rectangular contour bounded by test points A, B, C and D for the large antenna over the lossy earth.**

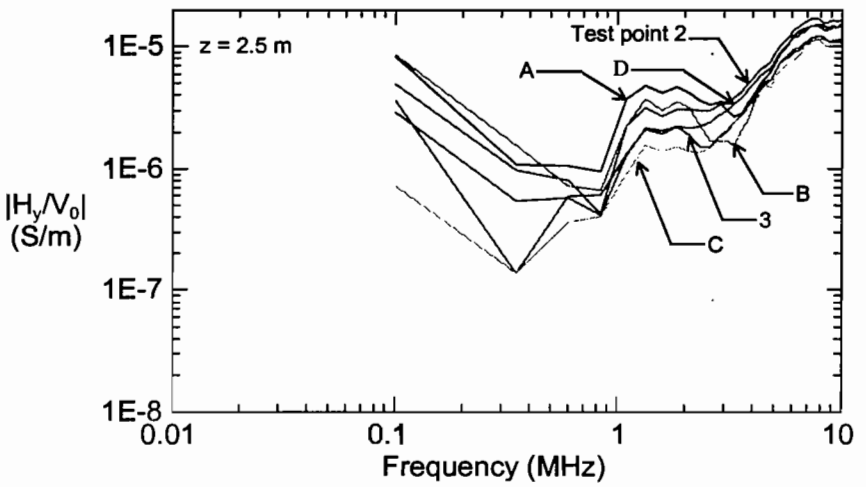


**Figure 106. Plots of the measured $H_y$ field at a height of 2.5 m along the rectangular contour bounded by test points A, B, C and D for the large antenna over the lossy earth.**

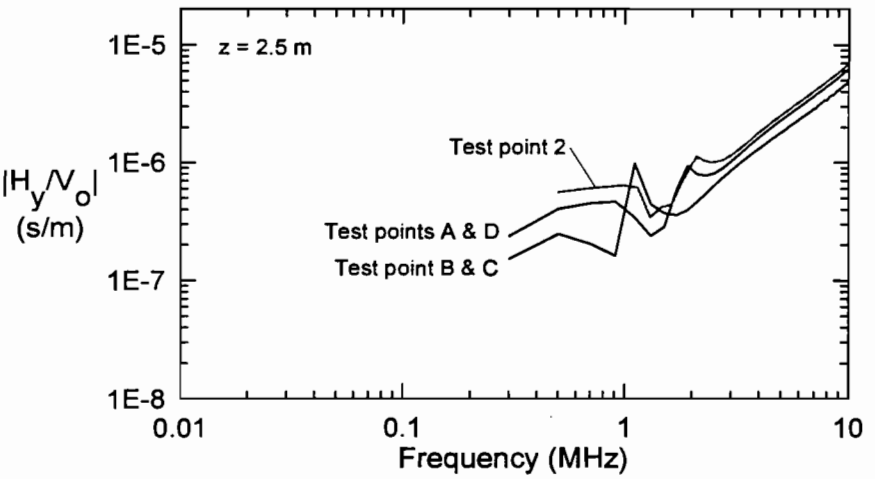


**Figure 107. Plots of the calculated $H_y$ field at a height of 2.5 m along the rectangular contour bounded by test points A, B, C and D for the large antenna over the lossy earth.**

### 6.4.9 Wave Impedance in the Forward Direction of the Large Antenna

*6.4.9.1 Impedance along the antenna centerline*

Using the E-fields of Figure 88 and the H-fields in Figure 98, the wave impedance at test points 2, 4 and 5 at a height of 1 meter have been calculated. These data are shown in Figure 108, as a function of normalized frequency $kx$, where $x$ denotes the test point coordinate along the $x$-axis. Notice that the rather large impedance values for low frequencies for test point 2 correspond to the nulls in the H-field Figure 98. For these low frequencies, the reliability of these wave impedances is suspect, due to the noise in the field measurements.

Figure 109 presents the computed impedances for test points 2, 4 and 5, to be compared with Figure 108. Here, the comparison is poor, suggesting that the lossy earth has a significant effect on the wave impedance. In comparing the wave impedance plot in Figure 76 for the perfect ground with the present responses, we note that there is a clear difference in the trends of the data. However, in the present case, it is not clear exactly how the "optimum" antenna resistance should be determined. Perhaps with another choice of the resistance loading, better behavior of the wave impedance in the forward direction would be observed.

The impedance plots for test points 2 and 4 at a height of 2.5 meters are shown in Figure 110, with the corresponding theoretical values plotted in Figure 111.

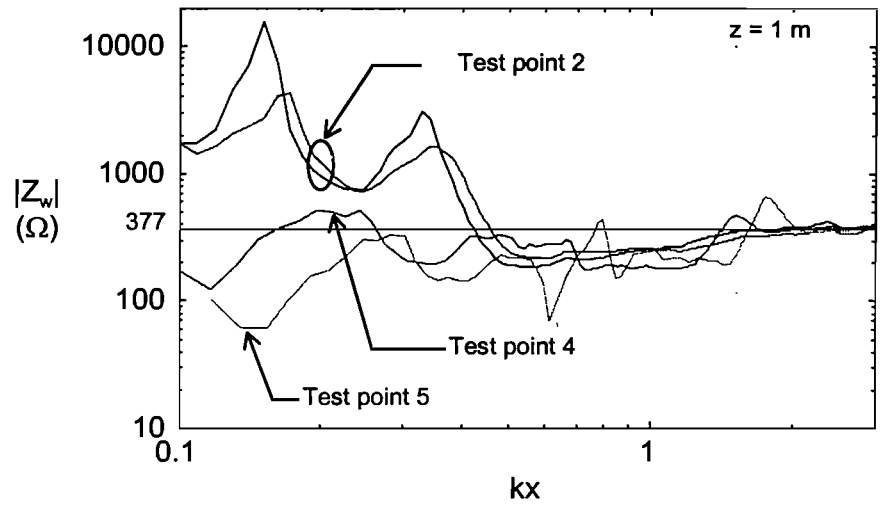


**Figure 108. Plot of the wave impedance $Z_w$ magnitude at a height of 1 meter for different test points for the large antenna over the imperfectly conducting earth.**

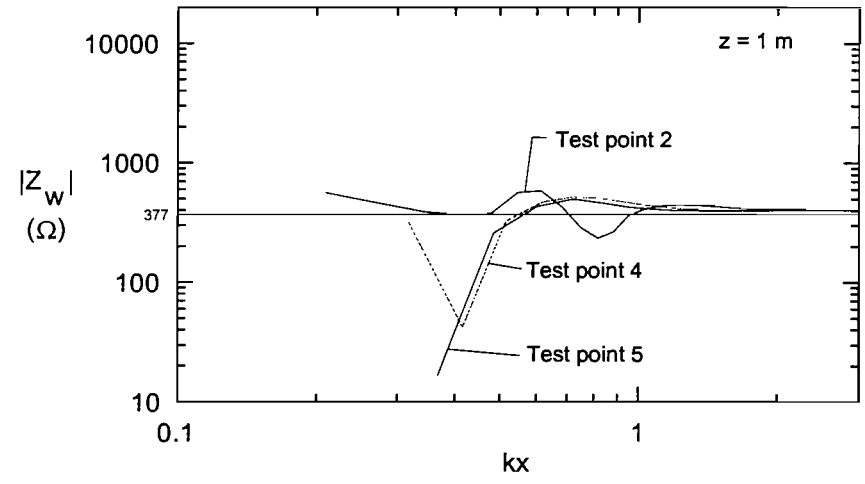


**Figure 109. Plot of the theoretical wave impedance $Z_w$ magnitude at a height of 1 meter for different test points for the large antenna over the imperfectly conducting earth having an assumed earth conductivity $\sigma = 0.01$ S/m and permittivity $\varepsilon_r = 10$.**

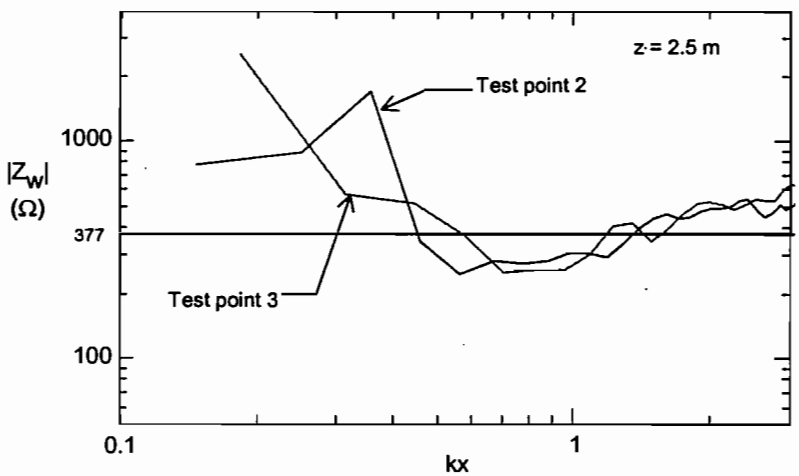


**Figure 110. Plot of the wave impedance $Z_w$ magnitude at a height of 2.5 meter at two test points for the large antenna over the imperfectly conducting earth.**

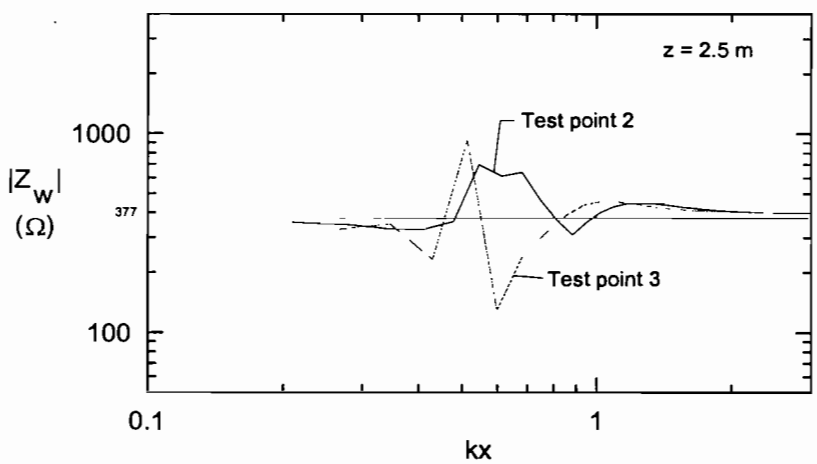


**Figure 111. Plot of the theoretical wave impedance $Z_w$ magnitude at a height of 2.5 meter for different test points for the large antenna over the imperfectly conducting earth having an assumed earth conductivity $\sigma = 0.01$ S/m and permittivity $\varepsilon_r = 10$.**

*6.4.9.2 Impedance along the A-B-C-D contour*

Variations of the wave impedance in the transverse direction for the large antenna as derived from the measured $E_z$ and $H_y$ field components are presented in Figure 112 for a sensor height of 1 meter. The corresponding theoretical values are shown in Figure 113. Similarly, Figure 114 presents the measured impedances for a height of 2.5 meters, with the theoretical values being plotted in Figure115.

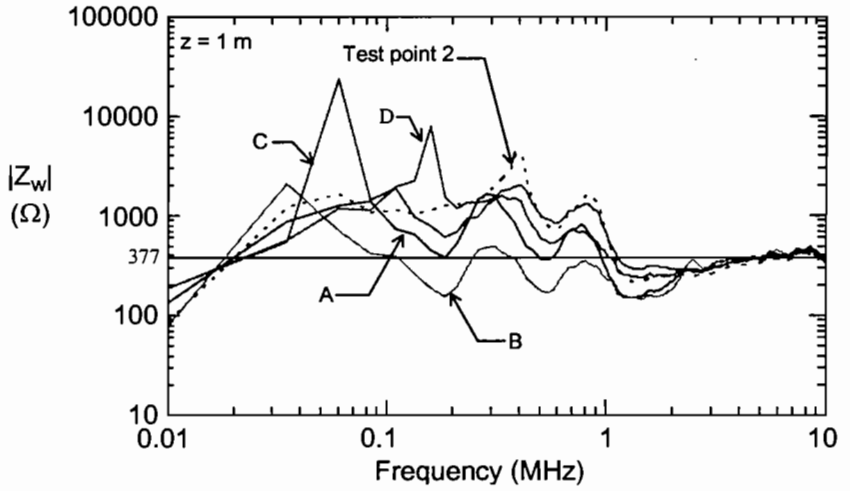


**Figure 112. Plots of the measured wave impedance along the rectangular contour bounded by test points A, B, C and D at a height of 1 m for the large antenna over the lossy earth.**

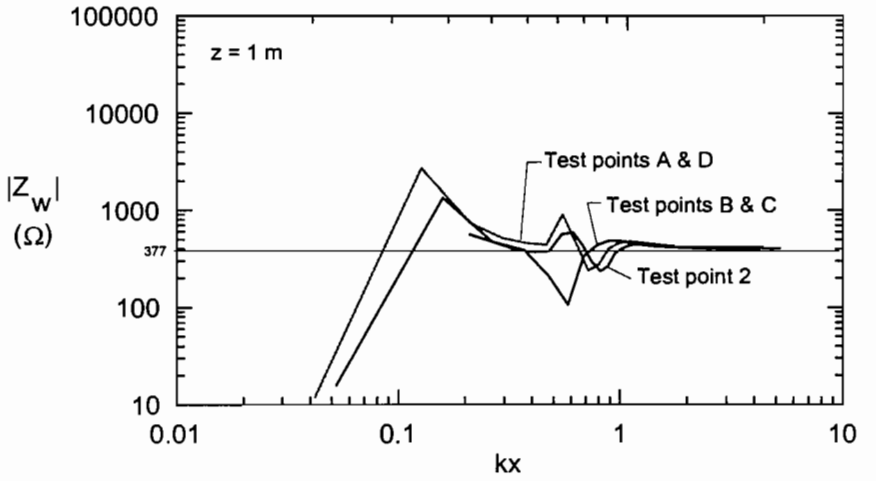


**Figure 113. Plots of the theoretical wave impedance along the rectangular contour bounded by test points A, B, C and D at a height of 1 m for the large antenna over the lossy earth.**

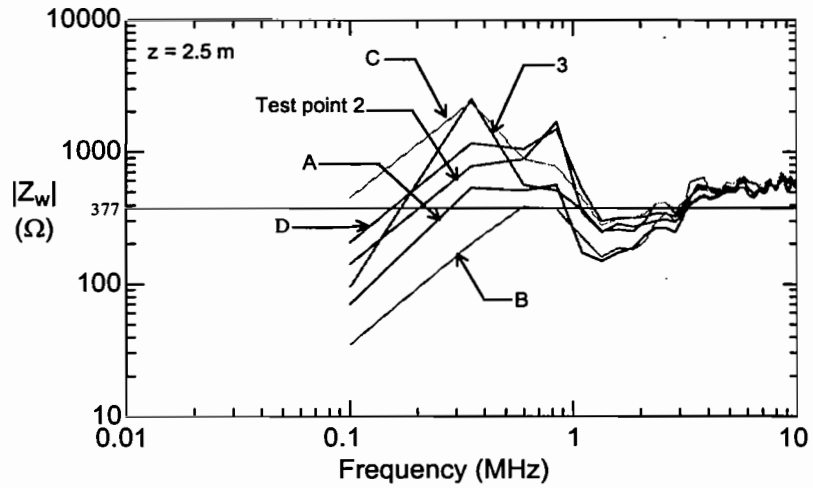


**Figure 114. Plots of the measured wave impedance along the rectangular contour bounded by test points A, B, C and D at a height of 2.5 m for the large antenna over the lossy earth.**

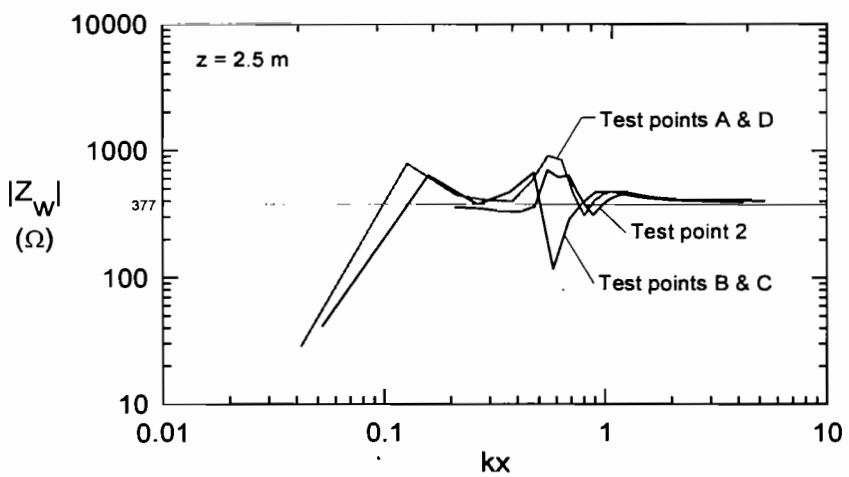


**Figure115. Plots of the theoretical wave impedance along the rectangular contour bounded by test points A, B, C and D at a height of 2.5 m for the large antenna over the lossy earth.**

## 7. Summary and Conclusions

This report has summarized a combined theoretical and experimental effort designed to better understand and characterize the p×m antenna. In this report, the fundamental behavior of idealized point electric and magnetic dipole moments has been examined, and this behavior is then related to the more complex radiation of physical antenna structures. Several different shapes of possible p×m antennas have been considered, and design curves for the optimum antenna loading resistance have been presented.

The analysis leading to the design curves for the p×m antennas is based on DC considerations, and assumes that the ground plane next to the antenna is a perfect conductor. At higher frequencies where other multipoles are excited, or when the antenna is located on a real earth, the antenna behavior departs from that of the ideal p×m antenna, and these issues have been examined.

Based on the computational model of one of the antennas — the inverted V antenna with a ground return wire— a measurement program was conducted, permitting a comparison of the theoretical and experimental results. Generally, we have seen that the comparison between the calculated and measured data is reasonable for the case of the p×m antenna over a highly conducting ground plane. However, when the antenna is operated over a real earth, the agreement is not as good. In this latter case, trends in the data still agree, allowing one to conclude that the analysis models remain useful tools for inferring p×m antenna behavior in real-earth environments.

From this study, a number of observations and conclusions may be drawn. They include:

- The real p×m antenna of finite extent behaves as expected, especially when operated over a highly conducting ground plane. It produces near fields in the forward direction that have an impedance ratio of 377 Ω, and a field null in the backward direction.

- A real (lossy) earth has a significant effect on the wave impedance of the principal field components at very low frequencies in the near zone. This may limit the effectiveness of the antenna in real situations if an artificial ground plane or mat is not used.

- The efficiency of the antenna is inherently low. Most of the transmitted power is absorbed in the load resistance and not put into the EM fields surrounding the antenna. This observation must be put into perspective, however, as the radiating efficiency of *any* antenna, including the loop or linear dipole commonly used for EMC measurements will be poor at low frequencies.

- The p×m bandwidth of this illuminator is small, and the antenna operates best low frequencies. If the antenna is "pushed" and operated at higher high

frequencies, it begins to behave more like a traveling wave, or Beverage, antenna with the direction of the main beam moving from the backward to forward direction. For CW measurements, however, this change of pattern may not be very important, as long as there is some field radiated in the forward direction.

The results of this work suggest several other interesting areas of future inquiry in to the understanding and use of the p×m antenna for system testing. These include:

- Performing of a near-field coupling study with canonical structures (a rod, a sphere, a cube, etc.) to compare the responses from a p×m antenna to those induced by a plane wave
- Investigation of techniques to increase the bandwidth of the p×m antenna by considering log-periodic arrays of antennas
- Evaluating the effects of reactive loading of the antenna in an attempt to "correct" for the unwanted effects of a lossy earth
- Study the possibility of creating localized, near fields from a p×m antenna that are not grazing to the local ground plane (i.e., attempt to simulate a plane wave incident on the ground plane with an arbitrary angle of incidence[5]).
- Evaluation of internal earth fields produced by a p×m antenna in an attempt to illuminate buried structures

Finally, an effort in the practical design and deployment of this type of antenna would include:

- Develop design criteria for an easy to use p×m antenna
- Construct the antenna thus designed and perform field calibration tests for its use in system testing.

---

[5] Note that other types of antenna systems, such at TORUS or ELLIPTICUS, provide this type of excitation. The suggestion here is to consider a radiating structure that is not connected to the earth, but supported above the earth by an airborne platform.

## 8. References


1. Tesche, F. M., "The PxM Antenna and Applications to Radiated Field Testing of Electrical Systems, Part 1 - Theory and Numerical Simulations", *Sensor and Simulation Notes*, Note 407, Phillips Laboratory, Kirtland AFB, NM, June 11, 1997.

2. Karlsson, T., et. al, "Low Level Simulation of the EMP Environment in a Telecommunications Tower", paper presented at the May 1990 Nuclear EMP Meeting (NEM), Albuquerque, NM.

3. Yu, J. S., C-L James Chen and C. E. Baum, "Multipole Radiations: Formulation and Evaluation for Small EMP Simulators", *Sensor and Simulation Notes*, Note 243, Phillips Laboratory, Kirtland AFB, NM, July 19, 1978.

4. Van Bladel, J., **Electromagnetic Fields**, McGraw Hill, New York, 1964.

5. Sylvester, P., **Modern Electromagnetic Fields**, Prentice-Hall, Englewood Cliffs, N.J, 1967.

6. Harrington, R. F., **Field Computation by Moment Methods**, Reprinted by the author, Syracuse University, Syracuse, NY, 1968.

7. Tesche, F. M., M. V. Ianoz and T. Karlsson, **EMC Analysis Methods and Computational Models**, John Wiley & Sons, New York, 1996.

8. Lee, K. S .H., ed., **EMP Interaction: Principles, Techniques and Reference Data**, Taylor & Francis, New York, 1989.

9. Burke, G. J., and A. J. Poggio, "Numerical Electromagnetics Code (NEC) - Method of Moments", NOSC TD 116, January 1981.

10. Baum, C. E., "EMP Simulators for Various Types of Nuclear EMP Environments: An Interim Categorization," *IEEE TRANS. EMC,* Vol. EMC-20, No.1, Feb. 1978.

11. Baum, C. E., and H. Chang, "Fields at the Center of a Full Circular TORUS and a Vertically Oriented TORUS on a Perfectly Conducting Earth", *Sensor and Simulation Notes*, Note 160, December 1972.

12. Zuffada, C., F. C. Yang, and I. Wong, "On the Thin Toroidal and Elliptical Antennas", *Sensor and Simulation Notes*, Note 315, January 1989.

13. King, R. W. P., and G. S. Smith, **Antennas in Matter**, The MIT Press, Cambridge, 1981.

14. Jordan, E. C. and K. G. Balmain, **Electromagnetic Waves and Radiating Systems**, Prentice Hall, Englewood Cliffs, 1968.

15. Burke, G. J. and E. K. Miller, "Modeling Antennas Near to and Penetrating a Lossy Interface", *IEEE Trans. AP*, Vol. AP-32, No. 10, pp.1040-1049, October 1984.

16. Baños, A., **Dipole Radiation in the Presence of a Conducting Half-Space**, Pergamon Press., New York, 1966.

17. Wait, J. R., **Electromagnetic Waves in Stratified Media**, MacMillan Co., New York, 1962

18. *IEEE Standard Calibration of Electromagnetic Field Sensors and Probes, Excluding Antennas, from 9 KHz to 40 GHz*, IEEE STD 1309-1966.

## Appendix A

## Analysis of the Uniformly Loaded Toroidal Antenna

### 1. Introduction

Details of the analysis of a resistively loaded loop antenna have been discussed by Baum and Chang [A1], with applications to a toroidal EMP simulator. Known as a transient omnidirectional radiating unidistant and static (TORUS) simulator, this antenna has been designed so that the quasistatic E/H ratio in the center of the loop is equal to the impedance of free space $Z_0 \approx 377\ \Omega$. This is accomplished by loading the loop conductor with a uniformly distributed per-unit-length resistance $R'$ having a value

$$R' = \frac{R}{2\pi b} = \frac{Z_o}{2\pi b}\left[\ln\left(\frac{8b}{a}\right) - 2\right] \ (\Omega / m) \qquad \text{(A1)}$$

where $R$ is the total resistance load along the loop, $b$ is the radius of the loop, and $a$ is the conductor radius. The geometry of this antenna is shown in Figure A 1.

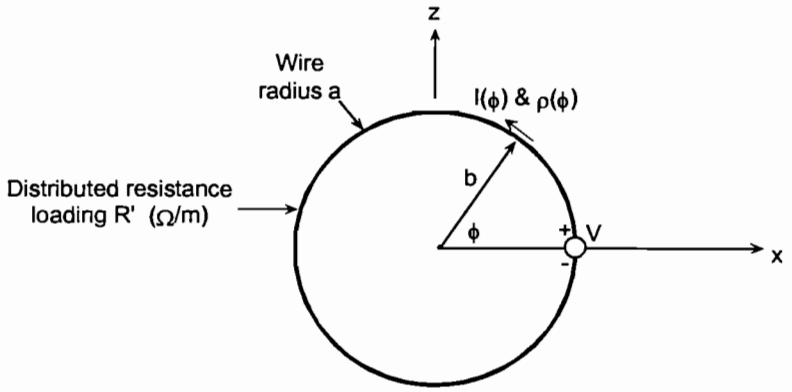


**Figure A 1. Geometry of the circular loop antenna.**

Although this type of antenna has already been considered in Section 3.4 using the quasi-static electric and dipole moments calculations, it is possible to use the same analysis as that of Baum and Chang to analytically determine the appropriate distributed loading $R'$ for optimum PxM operation. In doing so, it is found that the value of this resistance is exactly ½ of the value needed for achieving the quasistatic E/H ratio of 377 Ω at the loop center. That is to say, it can be shown that the necessary loading of the loop for the correct PxM condition is

---

A1. Baum, C. E., and H. Chang, "Fields at the Center of a Full Circular TORUS and a Vertically Oriented TORUS on a Perfectly Conducting Earth", *Sensor and Simulation Notes*, Note 160, December 1972.

$$R'_{PxM} = \frac{R'}{2} = \frac{Z_o}{4\pi b}\left[\ln\left(\frac{8b}{a}\right) - 2\right] (\Omega / m). \qquad \text{(A2)}$$

In this appendix, the analysis approach used by Baum and Chang for determining the current and charge on the loop structure is reviewed and the necessary PxM loading given in Eq.(A2) is derived.

## 2. The Integral Equation for the Loop Antenna

The analysis of the current flowing on the loop structure arising from the localized voltage generator $V$ is discussed in detail in ref. [A1]. For a fat toroidal structure, there will be surface currents flowing in the two orthogonal directions on the conductor surface, and these can be described by a relatively complicated set of coupled integral equations. For the present case, however, when the wire radius is much smaller than the loop radius ($a << b$), and for frequencies such that the wire is electrically thin ($a << \lambda$), the azimuthal current on the conductors is approximately zero and the only current on the antenna that must be determined is the total current $I(\phi)$ circumferentially on the loop.

This loop current is described by an integral equation of the form

$$V\delta(\phi) = \frac{jZ_o}{4\pi}\int_{-\pi}^{\pi} M(\phi - \phi')I(\phi')d\phi' - R'I(\phi) \qquad \text{(A3)}$$

where the kernel $M$ is defined as

$$M(\phi - \phi') = \frac{b}{2\pi}\left[kb\cos(\phi - \phi') + \frac{1}{kb}\frac{\partial^2}{\partial\phi^2}\right]\int_{-\pi}^{\pi}\frac{e^{-jkr}}{r}d\zeta, \qquad \text{(A4a)}$$

where $k = \omega/c$ and the distance $r$ is given as

$$r = \sqrt{\left(2b\sin(\frac{\phi - \phi'}{2})\right)^2 + \left(2a\sin\left(\frac{\zeta}{2}\right)\right)^2}. \qquad \text{(A4b)}$$

Details of the derivation of this equation are presented in [A1] and in Collin [A2].

---

A2. Collin, R. E., and F. J. Zucker, **Antenna Theory**, Part 1, Chapter 11, McGraw-Hill, New York, 1969.

## 3. Solutions to the Integral Equation

There are several different ways to solve this equation for the current $I(\phi)$. One way is to use asymptotic antenna theory to develop transmission line type currents flowing on the loop [A3]. This approach leads to rather simple forms for the loop current, but has inaccuracies in representing the effects of radiation on the solution. However, at low frequencies these inaccuracies are not very important.

Another solution approach is to solve Eq.(A3) numerically using the method of moments [A4]. Such approach involves representing the current by a set of pulse functions over the loop, and then casting the integral equation into a matrix equation which is solved numerically. Such a solution requires a direct numerical integration of the kernel $M$, and has been illustrated by Mei [A5]. Frequently, the thin-wire approximation [A6] is used to simplify the singular integral found in the kernel $M$, and this results in the following expression for the kernel:

$$M(\phi-\phi') \approx b\left[ kb\cos(\phi-\phi') + \frac{1}{kb}\frac{\partial^2}{\partial\phi^2} \right]\frac{e^{-jkr}}{r} \qquad \text{(A5a)}$$

where the distance $r$ is now expressed as

$$r = \sqrt{\left( 2b\sin(\frac{\phi-\phi'}{2}) \right)^2 + a^2}\ . \qquad \text{(A5b)}$$

A third approach for determining the loop current arises from work by Wu [A7] and King [A2], and later expanded upon by Baum [A1]. This is a more analytical approach in which the kernel, forcing function and current are all expanded in a Fourier series in the angle $\phi$ on the loop. From this expansion, the coefficients for each term can be determined analytically, and this results in a complicated, albeit closed-form, solution for the current.

---


A3. Zuffada, C., F. C. Yang, and I. Wong, "On the Thin Toroidal and Elliptical Antennas", *Sensor and Simulation Notes*, Note 315, January 1989.

A4. Harrington, R. F., **Field Computation by Moment Methods**, Reprinted by the author, Syracuse University, Syracuse, NY, 1968.

A5. Mei, K. K., "On the Integral Equations of Thin-Wire Antennas, *IEEE Trans. AP*, Vol. AP-13, No.3, May 1965, pp. 374-378.

A6. Tesche, F. M., "The Effect of the Thin-Wire Approximation and the Source Gap Model on the High Frequency Integral Equation Solution of Radiating Antennas," *IEEE Trans AP*, pp 210-211, March 1972.

A7. Wu, T. T., "Theory of the Thin Circular Antenna", *J. Math. Phys.*, Vol. 3. pp. 1301-1304, 1962.

Summarizing the final results of this development, the current on the loop may be expressed as an infinite sum of terms as

$$I(\phi) = I_o + 2\sum_{n=1}^{\infty} I_n \cos(n\phi). \tag{A6}$$

The associated linear charge density $\rho'$ on the loop is found from the continuity equation $\nabla \cdot \vec{J} = -j\omega\rho$ to be

$$\begin{aligned} \rho'(\phi) &= \frac{-1}{j\omega b}\frac{\partial I(\phi)}{\partial \phi} \\ &= \frac{2}{j\omega b}\sum_{n=1}^{\infty} n I_n \sin(n\phi) \end{aligned} \tag{A7a}$$

or

$$c\rho'(\phi) = \frac{2}{jkb}\sum_{n=1}^{\infty} n I_n \sin(n\phi) \tag{A7b}$$

where the normalizing constant $c$ is the speed of light. For a uniformly loaded antenna, the expansion coefficients $I_n$ can be expressed in terms of the antenna excitation voltage $V$ and total load resistance $R$ as

$$I_n = \frac{V}{R + i\pi Z_o \alpha_n}, \tag{A8}$$

where the coefficient $\alpha_n$ is

$$\alpha_n = b\left[\frac{-n^2 K_n}{kb} + \frac{kb}{2}\left(K_{n-1} + K_{n+1}\right)\right] \tag{A9}$$

and the terms $K_n$ are integrals of the kernel, weighted by the term $\exp(in\phi)$:

$$K_n = \frac{1}{2\pi}\int_{-\pi}^{\pi} \frac{e^{-jkr}}{r} e^{in\phi} d\phi. \tag{A10}$$

The distance $r$ is given in Eq.(A5b). Note that this last expression has been simplified somewhat from that presented by Baum [A1] by the use of the thin-wire approximation.

The integrals for the $K_n$ functions can be performed numerically, if desired. However, as the order n increases, the integrand becomes highly oscillatory, and the integrals are slow to converge. This has led to further analytical representations of the integrals. It is shown that the $K_n$ can be expressed as

$$K_n = \frac{1}{\pi b}\left[ \mathsf{K}_o\left(\frac{na}{b}\right)\mathsf{I}_o\left(\frac{na}{b}\right) + C_n - \pi S_{2n}(kb) \right] \qquad \text{(A11)}$$

where $\mathsf{K}_0$ and $\mathsf{I}_0$ are the modified Bessel functions, $S_{2n}$ is the Anger-Weber function [A8] and $C_n$ is defined as

$$C_n = \gamma + \ln(4n) - 2\sum_{m=0}^{n-1}(2m+1)^{-1} \qquad \text{(A12)}$$

with $\gamma \approx 0.5772157..$

As an example of the solution to the integral equation, the half-loop structure shown in Figure 17 of this report was considered with a diameter $d = 2b = 12$ m and wire radius $a = 0.1$ cm. Using image theory, this is equivalent to the total loop structure discussed in this appendix, with a voltage source $V = 2V_o$ and a total loop resistance of $R = 2R_L$. For this structure, the normalized charge density $c\rho'/V_o$ was computed as a function of position along the loop, for the source located at $\zeta = 18.85$ m, and assuming a low operating frequency so that $kb \ll 1$.

Figure A 2 presents these results for three different analysis methods. The static integral equation discussed in Section 2 provides a simple and accurate solution for the charge, and results from this analysis are illustrated by the solid line in the figure. The NEC code [A9] conducts a direct numerical solution of the integral equation, and the computed charge density is then found from the continuity equation. These results are also shown in the figure (the dotted line), as computed at a frequency where $kb \approx 0.095$, since NEC will not permit calculations at DC. Notice that there are some minor oscillations in the charge due to numerical instabilities in the code at very low frequencies, and that also NEC appears to have a difficulty in computing the charge density in the first cell at the source location. This may be due to a problem with the finite-difference representation for the charge.

Also shown in Figure A 2 are the results of the Fourier expansion solution for the charge, starting with 1 term in the series in Eq.(A7) and progressing up to a total of 5 terms. It is clear that the solution is converging to the correct static limit for the charge.

---

A8. Baum, C. E., H. Chang, and J. P. Martinez, "Analytical Approximations and Numerical Techniques for the Integral of the Anger-Weber Function", *Mathematics Notes*, Note 25, August 1972.

A9. Burke, G. J., and A. J. Poggio, "Numerical Electromagnetic Code (NEC) - Method of Moments," NOSC Tech. Doc. 116, Naval Ocean Systems Center, San Diego, CA, Revised January 2, 1980.

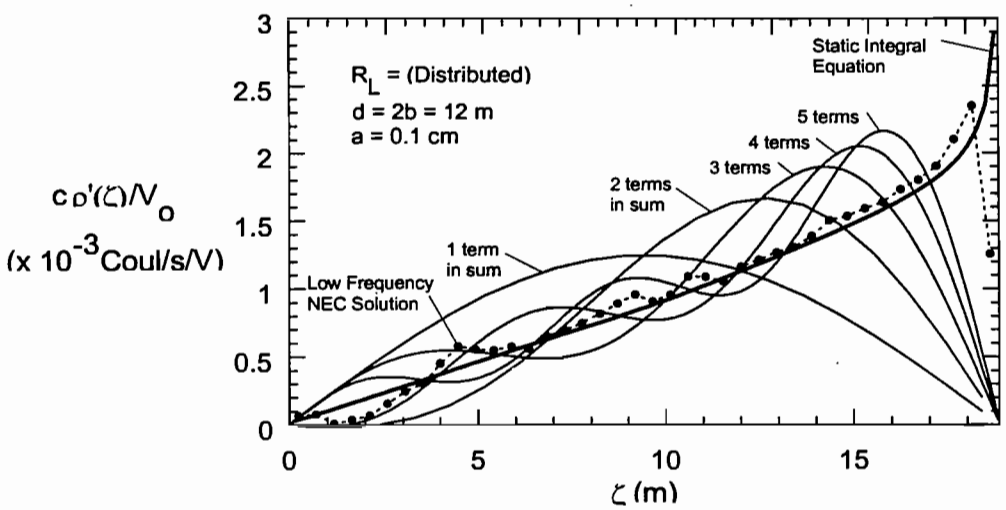


**Figure A 2. Plot of the normalized static linear charge density on the loop antenna.**

## 4. Quasistatic Fields at the Loop Center

The E and H fields at any point in space can be evaluated by integrating over the current distribution $I(\phi)$ with appropriate Green's functions. At low frequencies, these two calculations can be considered separately, with the H-field being computed by an integral over the quasistatic current distribution and the E-field computed by integrating over the charge distribution. At the center of the loop, it is easily seen that only the $n = 0$ term of the current expansion will contribute to the H-field, due to the spatial symmetry in the current modes. Similarly, only the $n = 1$ term of the charge expansion will contribute to the E-field.

The $a_0$ term of Eq.(A9) may be expressed as

$$\alpha_0 = kb\left[\frac{1}{\pi}\left(\ln\left(\frac{8b}{a}\right) - 2\right) - S_2(kb)\right] \tag{A13}$$

and as a result, the $n = 0$ term of the current becomes

$$I_0 = \frac{V}{R + jkb\,Z_o\left(\ln\left(\frac{8b}{a}\right) - 2 - \pi S_2(kb)\right)}. \tag{A14}$$

In the static limit as the frequency approaches zero, this current becomes simply

$$I_0 = \frac{V}{R}. \tag{A15}$$

Similarly, the $\alpha_1$ term in Eq.(A9) is

$$\begin{aligned}\alpha_1 = &\frac{kb}{2}\left[\frac{1}{\pi}\left(\ln\left(\frac{8b}{a}\right)-\frac{8}{3}\right)-S_0(kb)-S_4(kb)\right] \\ &-\frac{1}{kb}\left[\frac{1}{\pi}\left(\ln\left(\frac{8b}{a}\right)-2\right)-S_2(kb)\right]\end{aligned} \tag{A16}$$

and the $n = 1$ quasistatic normalized charge distribution mode is approximately

$$\rho_1'(\phi) \approx \frac{2V\sin(\phi)}{j\omega bR + cZ_o\left(\ln\left(\frac{8b}{a}\right)-2\right)}. \tag{A17}$$

At zero frequency, this charge density reduces to

$$\rho_1'(\phi) \approx \frac{2V\sin(\phi)}{cZ_o\left(\ln\left(\frac{8b}{a}\right)-2\right)} \tag{A18}$$

From the $n = 0$ and $n = 1$ modes of the current and charge on the loop, the static H and E fields at the center can be computed. The magnetic field is computed by the integral

$$\begin{aligned}H_y &= \frac{-1}{4\pi}\int\frac{I(\zeta)}{r^2}d\zeta = \frac{I_o}{4\pi}\int_{-\pi}^{\pi}\frac{bd\phi}{b^2} \\ &= -\frac{V}{2bR}\end{aligned} \tag{A19}$$

The static E-field may be calculated by a similar integral:

$$\begin{aligned}E_z &= \frac{1}{4\pi\varepsilon_o}\int\frac{\rho'(\zeta)}{b^2}\sin(\phi)d\zeta = \frac{V}{2\pi\varepsilon_o cZ_o\left(\ln\left(\frac{8b}{a}\right)-2\right)}\int_{-\pi}^{\pi}\frac{\sin^2(\phi)d\phi}{b} \\ &= \frac{V}{2b\left(\ln\left(\frac{8b}{a}\right)-2\right)}\end{aligned} \tag{A20}$$

The value of load resistance $R$ can be set by requiring that

$$\frac{|E_z|}{|H_y|} = Z_0 . \tag{A21}$$

Inserting Eqs(A19) and (A20) into this last expression immediately provides the necessary total load resistance value:

$$R = Z_0\left(\ln\left(\frac{2b}{a}\right) - 2\right). \tag{A22a}$$

Distributing this resistance uniformly over the circumference of the loop then yields the required distributed resistance

$$R' = \frac{Z_0}{2\pi b}\left(\ln\left(\frac{2b}{a}\right) - 2\right), \tag{A22b}$$

which is the expression stated in Eq.(A1)

## 5. Dipole Moments and the PxM Condition

The dipole moments, $m_y$ and $cp_z$, for the loop antenna can be also calculated from the $n = 0$ and $n = 1$ modal distributions. The magnetic dipole moment is immediately evaluated as

$$m_y = -I_o A = \pi b^2 \frac{V}{R}. \tag{A23}$$

The electric dipole moment is calculated as

$$\begin{aligned} cp_z = c\int \rho'(\zeta)\, z\, d\zeta &= \frac{2V}{Z_0\left(\ln\left(\frac{8b}{a}\right) - 2\right)} \int_{-\pi}^{\pi} b^2 \sin^2(\phi) d\phi \\ &= \frac{2\pi b^2 V}{Z_0\left(\ln\left(\frac{8b}{a}\right) - 2\right)} \end{aligned} \tag{A24}$$

Requiring that $m_y = cp_z$ for proper PxM operation of the antenna gives the relation

$$R_{PxM} = \tfrac{1}{2} Z_0\left(\ln\left(\frac{8b}{a}\right) - 2\right) \tag{A25}$$

which is ½ the total resistance needed for maintaining the proper E/H ratio in the center of the loop. It should be remembered that Eq.(A25) provides the *total* resistance on the

loop structure. If the half-loop over the ground, as illustrated in Figure 22 is to be considered, the physical loading on the half loop amounts to ½ of the value of the total loop. Thus,

$$R_{PxM}\Big|_{1/2\,Loop} = \tfrac{1}{4} Z_0 \left( \ln\left(\frac{8b}{a}\right) - 2 \right). \qquad \text{(A25)}$$

## Appendix B

### Considerations for the Network Analyzer Reference Voltage

In making measurements with the network analyzer, a measured response (say from an EM field probe) is always compared with a convenient reference signal. As shown in Figure B 1, this reference signal can be split off from the output of the network analyzer to provide a phase-stable reference. As a result, a measurement $M$ made of some quantity called $E$ will actually be normalized by the reference voltage $V_{ref}$, so that $M = E/V_{ref}$.

Frequently, it is desired to refer the measured data to a different voltage reference, as in the case of the PxM antenna analysis, where all responses are to be related to a unit voltage source at the antenna input. For example, in the report, all measured data have been processed in this manner. This appendix discusses some background information as to how this is accomplished.

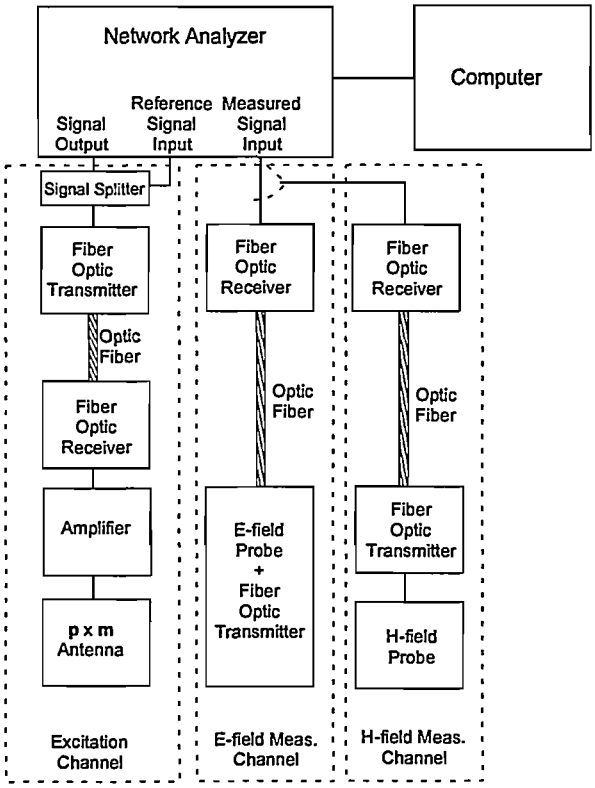


**Figure B 1. Example of the network analyzer connection to the excitation and measurement channels.**

In looking at the simplification of the measurement system output section shown in Figure B 2, one can view the splitter as an ideal transformer that takes the original voltage output of the network analyzer, $V_o$ and splits it up into two different channels -

each with a voltage $V_2$ and an impedance level of 50 Ω. If the splitter is designed properly, its impedance as seen by the output section of the analyzer is 50 Ω and as a result, the voltage at the input of the splitter is $V_1 = V_o/2$.

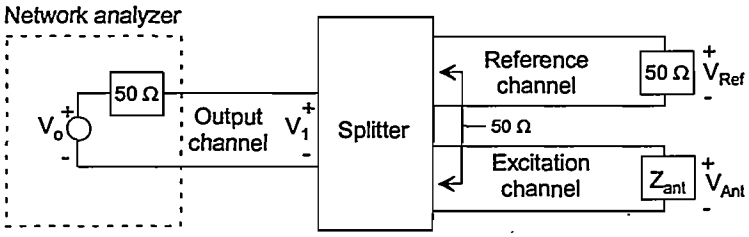


(a) Physical configuration


(b) Equivalent circuits

**Figure B 2. Simplification of the network analyzer feeding section (without the amplifier).**

The measurement reference channel is assumed to be loaded by 50 Ω and the voltage across this load, $V_{ref}$, is used as the reference quantity by the network analyzer. The other channel from the splitter feeds the antenna (neglecting, for the moment, the amplifier), and there is a voltage $V_{ant}$ developed across the effective load of the antenna, which is denoted as $Z_{ant}$.

From these two circuits, we see that

$$V_{ant} = \frac{Z_{ant}}{Z_{ant} + 50} V_2 \quad \text{and} \quad V_{ref} = \frac{50}{50 + 50} V_2 = \frac{1}{2} V_2$$

and consequently, the ratio $V_{ant}/V_{ref}$ is given by

$$\frac{V_{ant}}{V_{ref}} = \frac{2 Z_{ant}}{Z_{ant} + 50}.$$

Now, suppose that a particular measurement $M$ is made, which is some response relative to the reference voltage:

$$M = \frac{E_z}{V_{ref}}.$$

This measurement can now be referenced to the *antenna* source as

$$\frac{E_z}{V_{ant}} = \frac{E_z}{V_{ref}} \frac{V_{ref}}{V_{ant}} = M \frac{Z_{ant} + 50}{2 Z_{ant}}.$$

Thus, we note that the referencing of any measurement to the voltage source providing excitation to the antenna depends on the input impedance of the antenna — a quantity that may be frequency dependent in the most general case. This can pose problems in some cases.

At this point, it is necessary to include the effect of the amplifier. The amplifier increases the effective signal level fed into the antenna by a certain amplification factor, say $A$ dB, or equivalently, by a factor of $F = 10^{(A/20)}$. This implies that the expression given above is *too large* by this amplification factor. Thus, the corrected measurement result is obtained by *dividing* the measured data by $F$, giving

$$\left( \frac{E_z}{V_{ant}} \right)_{corr} = \frac{M}{F} \left( \frac{Z_{ant} + 50}{2 Z_{ant}} \right).$$